Charge and heat transport in non-metallic crystals using first-principles Boltzmann transport theory

Thesis by
Peishi Cheng

In Partial Fulfillment of the Requirements for the
Degree of
Doctor of Philosophy

CALIFORNIA INSTITUTE OF TECHNOLOGY
Pasadena, California

2022
Defended April 1, 2022

Peishi Cheng
ORCID: 0000-0002-3513-9972

ACKNOWLEDGEMENTS

I don't remember when acknowledgements became my favorite part of reading theses and attending defenses, but it was probably around the same time that I began looking forward to writing mine. This section has been my favorite because in contrast to academic writing whose precision is a defense against critique and revision, these confessions of thankfulness are imprecise, incomplete, and insufficient, and they are unimpeachably mine.

And now that it's my turn, I feel like I don't have the right words, and I don't even know who's going to read it, but I hope what is conveyed in a lasting way is this feeling of relief and gratitude for those who have carried me here to this moment.

I saw some acknowledgements started with a quote, so I guess I'll give that a try: In *Braiding Sweetgrass*, Robin Wall Kimmerer says "Ceremony focuses attention so that attention becomes intention." I want to focus my attention on how much of graduate research is a product of social interactions, and crystallize my intention of recognizing first and foremost that it is people and the communities that hold them that make work of any kind possible.

My first scientific mentor was Dr. Jacob Jones whose attentiveness and willingness to personally train me reflects his dedication to mentorship and made me feel like part of a scientific community. My second undergraduate adviser was Dr. Henry Sodano who made me feel like I was capable of research and whose support got me to graduate school.

At Caltech, of course Austin has had the largest influence on my development as a graduate student. I think it's fair to say that if it weren't for Austin, I would not have completed my degree. His patience is matched only by his stubbornness, and both happened to make it possible for me to graduate. His patience and understanding in giving me time to recover and not push myself too hard when I got 2-3 concussions in my second year gave me reassurance and support for continuing with research. His stubbornness has transformed my presentations to be more narratively cohesive than they otherwise would have been, and his stubborn belief that I am capable of doing this work has finally pushed me within reach of the finish line. I also really appreciate his

openness and willingness to meet, and his equanimity in meetings. Thank you Austin.

Nina was also one of the first people I worked with on research at Caltech. Thank you for introducing me to computational physics and sharing your appreciation of all the great food in LA. Andrew was the officemate in my first few years who I talked with the most. Your advice, sarcasm, and experience as an older graduate student were indispensable in getting me situated at Caltech. Alex: I guess the saying is "two is company and three is a crowd," but for grad school I feel like the saying should be "one is misery, and two makes it bearable." Thanks so much for letting me join the noise project and being a great collaborator. The star next to our names for equal contribution on our paper is one of the things I have enjoyed most in grad school. Adrian: together, the power of our complaining combined is a fearsome force. Navaneetha and Chengyun, thanks for being friendly scientific role models who are always willing to help. To others in the group who I've overlaped with: Nate, Nick, Taeyong, Junlong, Xiangwen, Yang, Jaeyun, Bo, Zoila, and Nachiket: Thank you for shaping my time here. To the younger students Benjamin, Tomi, Shi-Ning, David, and Azmain: Thank you for your energy and excitement, and I wish you a swift journey along a path you feel intentionally in control of.

To Christy Jenstad and Jennifer Blankenship. Christy, I remember running into you while walking around and absorbing the SoCal sun during my visit days, and your friendly chats then and since have made the department feel welcoming. Jennifer, your friendliness over email has almost a physical presence that helped me feel more connected during this pandemic, and all of your pun based advertising for department events always made me smile. Sonya: Thanks for always being a friendly face in Gates Thomas and always having a lab notebook for me.

Thank you to my thesis and candidacy committee members. Brent Fultz: Your presence feels like an inimitable part of the Materials Science department, and gave a friendly gravitas to this journey. Keith Schwab: Taking intro to solid state physics with you left me with important analogies, and your interest in my work after my candidacy was an appreciated reassurance. Marco Bernardi: MS 131 might have been the hardest class I've ever taken in my life, but it was also one of the classes whose concepts and methods I can see in all aspects of this thesis. Thanks for your rigor and for your commitment to computational

physics. Joe Falson: Thank you for taking the time to think about my work and agreeing to review the work of a stranger.

To all the friends I've met from ultimate – Daryl, Bryce, Paul, Erika, Sundar, and Radka: I might have left with a couple MTBIs but I won't forgot the memories we made and places we went. Daryl, I remember chatting until very late at Lucky Baldwin's during my visit days about the journey through academia, and to this day your drive to be a good scientist and friend remains a source of inspiration. Radka, thank you for your compassion and support in stumbling through the fog of concussions. Bryce, thanks for helping make it feel like part of Florida and home came to California too. Erika, thanks all the delicious meals we shared together and the shenanigans at the dinky Roosevelt house.

To my friends and co-organizers at Socialists of Caltech: thank you for helping me grow and transform my nebulous core of beliefs and values into concrete voice and action. Your dedication to and vision of justice helps me hold fast to the knowledge that any human power can be resisted and changed by human beings. Organizing together has illuminated a horizon that I may sometimes lose sight of, but one that I know I will be pulled and guided towards in the long run. Thank you Jane, B, Ashay, Dawna, Sean, Zoya, Kriti, Charles, Sam, Aaron, and Cai for sharing a path towards that horizon and walking together with me. Thanks in particular to Jane for always finding the energy to grasp and articulate the root of specific and general problems and then acting in the nicest and most serious way to deal with them, while being a caring and serious friend. Thanks to B for your intense and selfless thoughfulness and your complete pride in who you are. Sean: for being the funniest and most tender annoyed person I know. Charles: for reading enough and being correct enough for the rest of us and for bringing me to dingy and dank Jacobin reading groups on rainy LA nights all those years ago.

It was a bit silly of me to try to separate the communities I've been a part of since I've made friends through all of them, but now I'll give thanks to the people and relationships that don't fit neatly into groups but have shaped me just the same. I appreciate all of the new friends, old friends: everyone who's been a part of the community that not just kept the bottom from falling out, but the community that has been the undeniable high points of my time here.

Thank you Joe, Kaushik, Emily, Xuan, Thom, Frea, Konrad, Kate, Domenico, many others.

Thanks to Alon for keeping the friendships streak going since middle school. To Frances and Grace for your constant laughter and love, almost to the point of live laugh loving. To Siobhán for your kooky, kind, and resilient excitement for life. To Jash for your calm, grounded, and observant friendship. To Thom for your chaotic cackling and good heart. To Frea for your ability to turn anxious energy into sparkling curiosity and generosity towards people that I hope to one day learn. To my Florida and Yellowstoned crew Chris, Masud, Govind, and Weier for nearly 15 years of antics and great times. To Ollie for your relentless overthinking of how to do good. To Zeynep for setting an impossible example as GSC Advocacy chair getting everything done, and for being a friend whose thoughtfulness I aspire to. To Francesca and Román for bringing out the best in me and being a voice I can always count on to get to the root of things. To Wilbur for amazing me with your simultaneous ability to be relaxed and fun while being hungry for tennis and physics greatness. To Vasilije for always passing the vibe check and so easily slipping into thoughtful conversations. To Stax for counting los borregos with me and finding nonsense noises funny. To Katherine for being a role model of how to take care of people around you with delicious meals and so much more. To the fam, your friendships have been one of the greatest gifts I have received, and my thankfulness for your gifts motivates a reciprocity toward you all that I hope endures for as long as we can muster, and then more. To Erica for being a constant presence and for ridiculous and serious conversations that held me together when it mattered. And to Joeson: without our late night dinners and life chats, I really don't think I would have made it out of grad school. I hope we continue to challenge and shape each others' views of muddling through life.

Finally to my family which has only grown more dear as I got further away. To my mom for enduring all my sour photo faces in front of beautiful scenery and for your love, support, grace, maturity, and fierce loyalty. To my dad for emphasizing the importance of academics which no doubt shaped my decision to come to grad school, and for your love and support. To my baby half sister Aurora for being a new light. And to my brother xiao kuei who taught me the only life lesson I'll ever need to know, but one that I didn't learn soon enough. I hope to keep trying to earn and deserve your admiration.

ABSTRACT

Phonon-phonon and electron-phonon interactions underlie many fundamental transport properties like thermal conductivity and electrical mobility, and models of these properties provide information about the underlying microscopic interactions present in the materials. Many of these models use the Boltzmann transport equation where the choice of the expression for the collision integral is the most important and challenging aspect since it should capture all of the relevant interactions. In the past the expressions were semi-empirical, but in recent decades first principles models with no fitting parameters have become more commonplace, leading to discovery of new materials or providing deeper insights into the relevant mechanisms governing transport. This thesis presents first-principles calculations of thermal conductivity in polymer crystals, and charge transport at high electric fields in semiconductors in the Boltzmann transport framework.

Polymers are thermally insulating in their typical amorphous form, but it is known that their thermal conductivity can be enhanced through drawing and aligning of their polymer chains. With perfect chain alignment, the structures can be described as polymer crystals, which tend to contain many atoms per unit cell. However, the conventional understanding of thermal transport in crystals predicts low thermal conductivity for complex, many atom unit cells. It is known from simple models that phonon focusing redirects the heat flow into the polymer chain direction, but the extent to which phonon focusing plays a role in setting the intrinsic upper limits of polymer thermal conductivity has not been assessed from a first principles standpoint. We calculate the ab initio lattice conductivity of polythiophene, a complex molecular crystal with 28 atoms per unit cell, using the temperature dependent effective potential (TDEP) method to obtain finite temperature phonon properties taking into account the large quantum nuclear motion of hydrogen atoms present in polymers. We find a high thermal conductivity due to phonon focusing and stiff branches that overcome the expected low phonon lifetimes. The phonon focusing aligns group velocities along the chain axis throughout the Brillouin zone, even for states with wave vector almost orthogonal to the chain axis.

For charge transport, ab initio calculations focus almost exclusively on low field mobility, but technologically relevant phenomena like negative differen-

tial resistance manifest only at high fields far from equilibrium. Further, there are no ab initio calculations of non-equilibrium electronic noise, which differs qualitatively from transport observables at high fields. We report a methodological advance that obtains both the high-field transport properties and the non-equilibrium noise using an ab initio Boltzmann transport approach. Our method extends the collision integral to high fields by making physically motivated approximations to account for the non-linearities at high fields.

Using our method, we calculate the high-field noise and transport properties in GaAs and find that the 1ph level of theory is inadequate. Thus, we implement an approximate form of higher order interactions where electrons are scattered consecutively by two phonons (2ph) and find that these 2ph processes qualitatively alter the energy relaxation of the electron system compared to 1ph scattering, resolving a long-standing discrepancy in the strength of intervalley scattering inferred from different experiments. We also calculate non-equilibrium electronic noise from first principles for the first time. However, we are not able to reproduce experimental trends, and we suggest that 2ph processes beyond our approximation may be necessary to obtain experimental agreement. Our calculation shows how noise provides a new observable against which the accuracy of first-principles methods can be measured.

PUBLISHED CONTENT AND CONTRIBUTIONS

Peishi Cheng, Shi-Ning Sun, Alexander Y. Choi, and Austin J. Minnich (Jan 2022). High-field transport and hot electron noise in GaAs from first principles: role of two-phonon scattering. In: arXiv:2201.11912

P.C. co-designed the research, conducted the calculations, analyzed the data, and wrote the manuscript.

Alexander Y. Choi*, Peishi Cheng*, Benjamin Hatanpää, and Austin J. Minnich (Apr 2021). Electronic noise of warm electrons in semiconductors from first principles. In: *Phys. Rev. Materials* 5, pp. 044603. DOI: 10.1103/PhysRevMaterials.5.044603

P.C. co-designed the research, generated the scattering matrices used in the transport calculation, analyzed the data, participated in the discussion and drafting of the figures, and wrote the Methods section of the manuscript.

Peishi Cheng, Nina Shulumba, and Austin J. Minnich (Sep 2019). Thermal transport and phonon focusing in complex molecular crystals: Ab initio study of polythiophene. In: *Phys. Rev. B* 100, pp. 094306. DOI: 10.1103/PhysRevB.100.094306.

P.C. co-designed the research, conducted the calculations, analyzed the data, and wrote the manuscript.

*These authors contributed equally to the work

TABLE OF CONTENTS

LIST OF ILLUSTRATIONS

Chapter 1

INTRODUCTION

This chapter has been adapted, in part, from:

> Peishi Cheng, Nina Shulumba, and Austin J. Minnich (Sep 2019). "Thermal transport and phonon focusing in complex molecular crystals: Ab initio study of polythiophene". In: *Phys. Rev. B* 100, pp. 094306. DOI: 10.1103/PhysRevB.100.094306.
>
> Alexander Y. Choi, Peishi Cheng, Benjamin Hatanpää, and Austin J. Minnich (Apr 2021). "Electronic noise of warm electrons in semiconductors from first principles". In: *Phys. Rev. Materials* 5, pp. 044603. DOI: 10.1103/PhysRevMaterials.5.044603
>
> Peishi Cheng, Shi-Ning Sun, Alexander Y. Choi, and Austin J. Minnich (Jan 2022). "High-field transport and hot electron noise in GaAs from first principles: role of two-phonon scattering". In: arXiv:2201.11912

In solids, resistance to the transport of heat and charge comes from the scattering experienced by heat and charge carriers like the electron and the phonon. Calculating macroscopic material properties like thermal or electrical conductivity can reveal the physics underlying the transport phenomena and help build better microscopic models of the resistive interactions that scatter electrons and phonons. This thesis concerns calculations of heat and charge transport with a first-principles description of the microscopic interactions to provide physical insight into the transport behavior of phonons and electrons in materials.

1.1 From phenomenological models to first-principles simulation using density functional theory

Some of earliest transport models that acknowledged the microscopic nature of the charge and heat carriers were the Drude model and the kinetic model of thermal conductivity. Below is the expression for electrical mobility obtained from the Drude model which treats the quantum mechanical electron entirely classically, but accounts for the resistance experienced by the electron through

a phenomenological relaxation time τ [1].

$$\mu = \frac{e\tau}{m^*} \tag{1.1}$$

Here, e is the elementary charge and m^* is the effective mass of the electron. Similarly, one can derive an expression for the thermal conductivity in an isotropic material due to phonons from the kinetic theory of gases [2], where the phenomenological quantity is the mean free path l.

$$\kappa = \frac{1}{3}Cvl = \frac{1}{3}Cv^2\tau \tag{1.2}$$

Here, C is the heat capacity, v is the phonon velocity, and the mean free path can also be expressed in terms of a relaxation time as $l = v\tau$. These relaxation times reflect the finite lifetime of electrons or phonons during transport due to all scattering processes occurring in the material, expressed through a single average number. This averaging obscures a more detailed picture of the transport physics.

Progress in solid state physics has been marked by better transport models and less approximate ways to obtain the relaxation time. Calculation of phonon thermal conductivity from the Boltzmann equation was first performed by Peierls [3] who obtained finite phonon lifetimes due to intrinsic anharmonicity from perturbation theory. The models that followed derived frequency and temperature dependent relaxation times but only for acoustic phonons whose dispersions were assumed to be linear [4, 5]. Building on these models, and in the absence of more accurate methods to determine phonon properties, studies instead developed intuitions for high thermal conductivity based on empirical observation [6]. For charge transport, theoretical advancements focused on expressions for the electron-phonon (e-ph) matrix element, with the very first attempt being made for free electrons in metals interacting with linear dispersion acoustic phonons [7]. In semiconductors, the matrix element was found by considering phonons as continuum elastic waves which deform the crystal and using macroscopic measured material properties like elastic constants for semi-empirical expressions, forming the basis of "deformation potential" theory [8], with later extensions to materials with multiple, anisotropic valley structures [9]. Moving beyond the free electron model with the pseudopotential method [10, 11] made the study of the e-ph interaction possible across a wider range of materials, but still requiring experimental measurements of phonon dispersions. Due to these limitations, a first-principles theory, also called ab initio

theory meaning a theory "from the beginning," was desired. An ab initio theory should be applicable to many materials, requiring the specification only of the atom positions and identities, and with scattering rates calculated for each unique state in the Brillouin zone.

The beginnings of such an ab initio treatment for both electrons and phonons on the same footing was made possible by Kohn-Sham density functional theory (DFT) [12] which solves for the electronic ground state based on functionals on the electron density. While the eigenstates of the Kohn-Sham Hamiltonian are fictitious orbitals that do not, in general, correspond to the quasiparticles of the actual system, they are still used as an approximate representation of the electronic states and provide a way to calculate interactions for each state individually. Phonon calculations from microscopic theories were possible before DFT but largely restricted to metals with a nearly free electron model [13]. DFT permitted a more general approach to lattice dynamics since atomic vibrations are defined by the interatomic forces which can be calculated in the DFT framework by the Hellman-Feynmann theorem [14, 15], with the initial methods directly displacing atoms [16, 17], and later methods using linear response theory [18]. DFT is not entirely free of shortcomings since all practical calculations use an approximate form of the exchange-correlation functional, and DFT cannot describe strongly correlated materials due to its nature as a mean-field method, but it is a desirable framework because it does not require any empirical inputs and is computationally efficient compared to more advanced theories.

Enabled by DFT, ab initio calculations of transport coefficients are now possible, revealing the most important factors governing transport phenomena and enabling predictive calculations for never-synthesized materials. A salient example was the prediction of remarkably high thermal conductivity of boron arsenide which, at the time, had never been synthesized [19]. The calculations attributed the high thermal conductivity to low phonon scattering rates due to unique features in the phonon dispersion, an analysis which was only possible due to calculation of phonon properties throughout the entire Brillouin zone. The subsequent synthesis and measurement of BAs [20, 21] stimulated further development of theory, revealing the importance of higher order scattering processes [20, 22]. We take this as an example of the dialectical process of theory guiding experiment, which then guides theory, and so on, and motivates our

first-principles calculations which aim to provide insight into the physics of microscopic interactions in materials.

1.2 Transport under the validity of perturbation theory: The Boltzmann transport equation

Next, let us narrow our scope to a particular framework of first-principles transport calculation. There are many ways to compute the heat and charge transport properties, with the appropriate method depending on the structure and spatial order of the material of interest, as well as the type and strength of the interactions in the material. In this thesis, we are interested in crystalline materials where the interactions can be treated using perturbation theory. Perturbation theory is valid when carriers can be described as weakly interacting quasiparticles whose lifetime is much longer than the frequency or energy of the quasiparticle itself. Under these conditions, transport can be calculated using the Boltzmann transport equation (BTE)

The history of the BTE extends back 150 years and a detailed derivation is beyond the scope of this thesis, so we aim to give a conceptual background based on the more rigorous account found in Ref. [23]. The BTE was originally formulated by Boltzmann to obtain macroscopic properties of gases from a microscopic picture of gas particle collisions through the use of probability distribution functions of particles having a given momentum and position. The BTE comes from the Liouville equation which is a conservation equation on the "flow" of the distribution function $f^{(N)}(t, \mathbf{r}, \mathbf{p})$ through some control volume in the momentum and position phase space for N particles, in analogy to fluids [24]. However, this phase space has $6N$ independent coordinates (3 momentum and 3 position coordinates for each particle) which renders the problem practically intractable. The BTE instead seeks to describe the distribution function of a single representative particle averaged over the coordinates of all other $N-1$ particles. The result of this averaging leads to a collision term which describes the redistribution of flow in the phase space of the representative particle due to its interactions and scattering with other particles.

Later, the BTE was extended to solid state physics to describe the distributions of heat and charge carriers. The BTE formalism for electrons and phonons is semi-classical in that the carriers are treated by neglecting any wave-like interactions but including particle-like collisions derived from quantum mechanical

perturbation theory using Fermi's Golden Rule. A first principles Boltzmann framework involves calculating the transition rates of Fermi's Golden Rule without reference to ad hoc constants, which has been made possible by DFT.

The Boltzmann equation is given below:

$$\frac{\partial f}{\partial t} + \frac{\mathbf{p}}{m} \cdot \nabla_{\mathbf{r}} f + \mathbf{F} \cdot \nabla_{\mathbf{p}} f = \left(\frac{\partial f}{\partial t} \right)_{\text{coll}} . \tag{1.3}$$

Here f is the distribution function $f(t, \mathbf{r}, \mathbf{p})$ which describes the probability of finding a particle at position $\mathbf{r}$ with momentum $\mathbf{p}$ at time t. The distribution function is the solution to the BTE we seek, which, in our case, is for phonons or electrons described as particles. $\mathbf{F}$ is any force field that acts on the particles, $\mathbf{p}$ is the momentum vector, $\mathbf{r}$ is the position vector. The various terms have physical meanings which we depict schematically in Fig. 1.1: the second term on the left hand side describes diffusion, the third term on the left hand side describes advection due to body forces on the particles, and the right hand side is the collision term which has no general form and depends on the system of interest. The principal difficulty with the Boltzmann equation is specifying the expression for the collision term which must include the relevant physics of the materials. In the ab initio framework, the collision integral calculates the scattering interactions from first principles. For transport, the electrons and phonons can interact with one another and with defects or impurities, or scatter due to disorder in the material. Let us now discuss the materials of

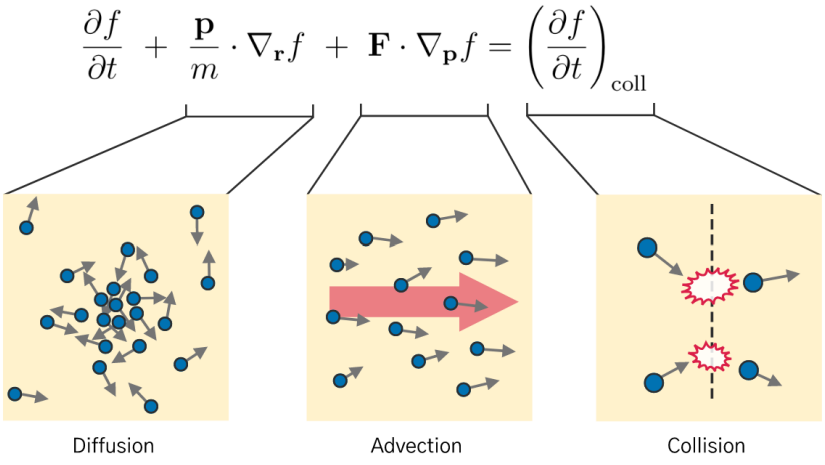

Figure 1.1: The BTE with schematic representation of particles undergoing processes represented by various terms in the equation.

interest in this thesis and the motivation for their study which will decide the relevant interactions to be included in the Boltzmann framework.

1.3 Heat transport: The intrinsic upper limit in crystalline polymers due to phonon-phonon interactions

While amorphous polymers are known to have poor thermal conductivities on the order of $\sim$ 0.1 $\mathrm{Wm^{-1}K^{-1}}$, it has been known since the late 1970s that orienting the polymer chains through drawing can increase the thermal conductivities along the draw direction by nearly 2 orders of magnitude [25, 26]. This enhancement was well understood in terms of the alignment and crystallization of the polymer chains that facilitates heat flow along the strong intrachain bonds instead of through the weak interchain van der Waals bonds [27]. However, a new wave of interest in the thermal properties of aligned polymers was generated beginning in 2010 due to a measured thermal conductivity of over 100 $\mathrm{Wm^{-1}K^{-1}}$ in a polyethylene nanofiber [28], suggesting that the upper limit of thermal conductivity in polymers is higher than previously thought. This upper limit exists at the theoretical ideal of drawing and chain alignment which is a fully crystalline polymer. For electrically insulating crystals, the thermal conductivity is due to phonons and can thus be described from first principles using the Boltzmann transport equation. Such a study would be of interest since the high thermal conductivity of polymer crystals which tend to have complex, many atom unit cells seem to buck the trend of other complex crystals which are typically poor thermal conductors [29].

The high uniaxial thermal conductivity in crystalline polymers can be partially attributed to the typically stiff, covalently bonded backbones of carbon, and partially to phonon focusing. Phonon focusing describes the situation where the phonon group velocity is not aligned with the wave vector, leading to preferential propagation of phonons along certain crystallographic directions and has been studied in polymers [30]. The theory of phonon focusing was first formulated to describe the propagation of elastic waves in single crystals [31] and first measured at low temperatures in cubic crystals as differing amplitudes and patterns of ballistic phonons based on the elastic anisotropy [32, 33]. In polymer crystals, the focusing phenomena is more exaggerated due to the extremely anisotropic bonding. Stronger covalent bonds in one crystal axis compared to the others lead to higher group velocities in that axis, leading to ellipsoidal isofrequency surfaces in the Brillouin zone. Since the group ve-

locity is the gradient of frequency with respect to wave vector, an ellipsoidal surface will have group velocity vectors preferentially oriented along the short axis of the ellipse. While early studies of phonon focusing were interested in imaging the patterns that result from low temperature ballistic transport to understand elastic anisotropy, at room temperatures these patterns vanish since the transport is diffusive, but the focusing still affects the thermal conductivity. Analyses of how focusing affects thermal conductivity were almost always restricted to acoustic phonons of small wave vector [34, 35]. So the combined effect of phonon focusing across the entire Brillouin zone with the many phonon branches of complex polymer crystals, in conjunction with the stiff polymer backbones giving large group velocities, is unclear.

Most modern simulations of heat transport in polymers have focused on other factors besides phonon focusing that affect thermal conductivity. A large fraction of studies have been molecular dynamics simulations establishing the microscopic basis for the relationship between morphology and thermal conductivity [36–38]. MD studies are useful because they can manipulate the force fields to show which interactions have the largest effect on morphology and thus thermal conductivity [39]. However, these force fields are also the primary shortcoming due to their semi-empirical nature, where studies of intrinsic thermal conductivity in PE using MD have produced significant discrepancies [40, 41].

Instead, first principles approaches based on the Boltzmann equation [42] are more suitable for studying intrinsic upper limits. The ab initio study of polymer crystals was made possible by the inclusion of the van der Waals (vdW) interaction in DFT, which is a non-trivial task due to the dynamical and non-local nature of vdW interactions compared to the most commonly employed DFT functionals that rely on approximations of locality [43]. With these advancements, first principles Boltzmann approaches have been applied to study the thermal conductivity of non-polymer quasi-1D crystals, reporting size effects [44], or symmetry selection rules [45]. Studies of polymer thermal transport focus on polyethylene, describing the change in thermal conductivity between a single PE chain and the bulk crystal [46]. Other studies of polymers are limited to assumptions of ballistic transport [47] or relaxation time approximations to the BTE [48]. Importantly, though, almost all studies neglect the effect of zero point nuclear motion which is large in polymers due to the pres-

ence of light hydrogen atoms with zero point energies corresponding to 1000 K [49]. This obstacle was overcome by application of the temperature-dependent effective potential (TDEP) method [50], adapted to include zero point motion by sampling the Born-Oppenheimer energy surface at the temperature of interest using thermal amplitudes that include the additional displacement from quantum nuclear motion [49, 51]. This sampling thus also includes the effect of finite temperature anharmonicity [52–54]. Without the correct quantum statistics for nuclear motion, the thermal conductivity in PE is overestimated by around 50% [49].

The work of this thesis is a first-principles calculation in a complex polymer crystal that informs the intrinsic upper limits of thermal conductivity in polymers, includes quantum nuclear motion, and analyzes the effect of phonon focusing throughout the entire Brillouin zone. Studying these theoretical limits provides guidance for how close experiments are to the ideal, and studying polymers beyond polyethylene allows us to make more general claims about the features are important in setting the high thermal conductivity. Our calculations focus on the intrinsic resistances in an electrically insulating complex crystal, and thus requires the phonon-phonon interactions coming from the anharmonicity in the material. The scattering of phonons by isotopes are also included due to natural isotopic distributions. These are the interactions which we must include in our first principles Boltzmann framework.

We will focus on crystalline polythiophene which is an example of a complex polymer crystal. It has 28 atoms per unit cell compared to the 12 atoms per unit cell of polyethylene. It has attracted interested in its substituted form, poly(3-hexylthiophene) (P3HT), for both its thermal [55, 56] and electrical properties [57]. Experimentally, a relatively high thermal conductivity of $\sim$4 $\mathrm{Wm^{-1}K^{-1}}$ was reported for amorphous aligned chains of unsubstituted polythiophene [58].

1.4 Charge transport: Non-linear effects and electron-phonon scattering in semiconductors at high electric fields

The current-field relationship of semiconductors is known to be non-linear at high electric fields, and the study of high-field charge transport is of fundamental and practical interest for semiconductor devices [59–62]. For example, nonlinear variation of drift velocity with electric field was observed in elemental

semiconductors [63–65], and current instabilities observed in III-V semiconductors [66, 67]. The current instabilities are known as the Gunn effect and form the basis of solid state microwave sources [59]. Modeling of high-field transport became widespread beginning in the 1970s through the application of the Monte Carlo method, enabling the simulation of various phenomena across a range of electric fields, temperatures, and geometries [68].

A qualitative understanding of the relevant physics at both low and high fields can be indirectly inferred from Monte Carlo simulation by fitting scattering rates to data, but the various free parameters and empirical constants suggest the need for a more precise and microscopic description of the scattering. Such a description is possible, especially given the advances in the ab initio theory of electron-phonon interactions [69, 70]. There are other interactions experienced by electrons in solids like electron-impurity or electron-electron interactions, but the dominant source of scattering at room temperature and low carrier concentrations is that of electrons scattered by phonons [70]. As a result, the low-field mobility has been computed from first principles within the quasiparticle picture using the Boltzmann transport equation for diverse materials [71] including Si [72–75], GaN [76], GaAs [77, 78], hybrid perovskites [79, 80], two-dimensional materials [81–84], and other compound semiconductors [85, 86]. For other materials with strong e-ph interactions where the quasiparticle picture breaks down, the charge carrier is the polaron and the Kubo formula has been applied to calculate the mobility [87–89]. Advances to ab initio e-ph theory continue to be reported, with examples such as the GW corrections to the e-ph interaction [75, 90] and inclusion of the quadrupole interaction [91, 92]. Within the Boltzmann transport framework, works have studied phonon drag [93] and magnetotransport [94].

The calculated observable in all of the above ab initio reports, though, is the low field mobility. This thesis is concerned with extending the ab initio calculation to high electric fields to model the non-linear transport characteristics of semiconductors. However, non-linearities arise in the collision integral at high fields since the quadratic terms present from linearizing the distribution about the equilibrium distribution can no longer be neglected as they were at low fields. There are recent works reporting high field transport from first principles where the non-linearities are included in the collision integral and the distribution is obtained by time stepping the BTE to steady state [95], or

by the Monte Carlo method [96]. In our work, we describe a method which solves for the steady state distribution directly through a series of physically motivated approximations. While such a method provides no information about the real time dynamics of reaching steady state, it avoids the numerical instabilities associated with time stepping [95].

We choose to study GaAs which is a prototypical semiconductor containing a region of negative differential mobility and exhibiting the Gunn effect. For GaAs, achieving quantitative accuracy in the first-principles calculation of even the low-field mobility remains a subject of ongoing work, with discrepancies between initial ab initio calculations [77, 78] largely ascribed to differences in the band structure with different effective masses and valley separations [97]. A recent calculation of electron mobility including higher-order terms in which electrons are sequentially scattered by two phonons has indicated that these processes are non-negligible [98]. Calculations at high fields including two-phonon processes may reveal additional effects of this scattering.

1.5 Hot electron noise: A new ab initio observable

While the majority of first principles simulation has focused on low field mobility with only two prior works reporting high field transport, there were no works prior to this thesis reporting an ab initio treatment of electronic noise at high fields, despite its experimental accessibility [99, 100] and its importance in applications like radio astronomy [101]. Electronic noise arises from stochastic nature of scattering processes which leads to fluctuations in the occupation of electronic states. A nonrandom measure of electronic noise is the power spectral density (PSD), often measured as the PSD of current fluctuations. Owing to the fluctuation-dissipation relation, the PSD close to equilibrium is proportional to the mobility and thus does not provide additional information about charge transport [102–104]; this is known as the Nyquist relation. However, away from equilibrium, the PSD contains qualitatively new information because it characterizes the fluctuations about a non-equilibrium steady-state distribution, in contrast to transport observables that characterize the mean of the steady-state distribution like drift velocity [99, 105].

The development of theory for treating fluctuations began in 1935 with the application of kinetic theory to velocity fluctuations in a non-equilibrium gas [106]. For charge carriers, an important link was established between the

diffusion coefficient under non-equilibrium steady state conditions and the spectral density of current fluctuations [107] which is why the current PSD at frequencies small compared to scattering rates is also known as diffusion noise. Most relevantly for our work, the noise calculation was later formulated in terms of solutions to the BTE [108], providing the foundation for our ab initio Boltzmann transport treatment. Numerical investigations of noise phenomena began in earnest around the same time that Monte Carlo simulations were used to study high-field transport. However, as with the study of high-field transport, a first-principles framework with no adjustable parameters for the calculation of noise is desirable.

The study of intervalley scattering is an example of both the ambiguity that arises from fitting parameters in semi-empirical models as well as the unique transport behavior exhibited by noise PSD. Intervalley scattering in GaAs in particular has been the subject of substantial experimental and theoretical study due to its role in producing negative differential resistance [61] and non-monotonic features of the PSD versus electric field [107, 109–111]. Early theoretical works derived symmetry selection rules for intervalley scattering, concluding that only LA and LO phonons could mediate intervalley coupling between states at the Γ and L points [112]. Diverse experimental and numerical methods have reached conflicting conclusions regarding the strength of intervalley scattering in GaAs as quantified by the intervalley deformation potential (IDP), denoted by $D_{\Gamma\mathrm{L}}$ [113]. Transport studies involving measurements of PSD [114, 115], I-V curves in sub-micron structures [116], and threshold field versus stress [117] interpreted using Monte Carlo simulations with semi-empirical scattering rates [118] concluded that the intervalley scattering strength must be weak ($D_{\Gamma\mathrm{L}} \sim 2 \times 10^8$ eV cm^{-1}) to match trends of experimental data. On the other hand, experiments based on photoluminescence of optically excited carriers inferred a markedly larger value ($D_{\Gamma\mathrm{L}} \sim 8 \times 10^8$ eV cm^{-1}) [119–123]. Recent first-principles calculations [124] support the larger value of the deformation potential due to contributions from non-longitudinal phonons, as selection rules are relaxed away from high symmetry points [125]. Advances in experimental methods have enabled the relaxation of photoexcited electrons to be monitored with momentum and energy resolution, providing insights into the effect of intervalley scattering on the differing timescales of momentum and energy relaxation [126–128]. Despite these experimental ad-

vances, the discrepancy in the intervalley scattering strength inferred from various experiments remains unresolved.

In the ab initio framework, all electronic states are treated on the same footing and definition of intervalley scattering simply comes from which states are selected to belong to a particular valley [126]. However, in practice, calculations are limited to an energy range of interest which creates a separation between electronic states in the Brillouin zones and provides a convenient way to define different valleys. In this manner, the first principles calculation provides a far less ambiguous method of investigating the effect of intervalley processes on the high-field transport by showing the aggregate effect of all such processes calculated without parameterizing based on valley label. Furthermore, the effect of 2ph scattering has only been studied for low field mobility. The 2ph processes may produce additional effects on high field transport if they have a non-trivial contribution at higher energies where intervalley scattering occurs in GaAs.

1.6 Outline of thesis

In this thesis, we show how our first principles calculations test the limits of conventional ab initio theory and revealing the mechanisms that determine transport phenomena.

In Chapter 2, we give an overview of the Temperature Dependent Effective Potential (TDEP) method to obtain interatomic force constants that accounts for zero point nuclear motion, as well as an overview of the thermal conductivity calculation using the Boltzmann equation. We then calculate the lattice thermal conductivity of polythiophene, a complex polymer crystal. We find a high thermal conductivity nearing 200 $\mathrm{Wm^{-1}K^{-1}}$ despite a complex unit cell containing 28 atoms due to extremely anisotropic bonding which leads to strong phonon focusing and high group velocities in both acoustic and optical branches throughout the Brillouin zone that overcomes the expected short phonon lifetimes. Without the phonon focusing that aligns group velocities along the chain axis, the thermal conductivity would be reduced to a value of 34 $\mathrm{Wm^{-1}K^{-1}}$. As additional evidence of the generality of the phonon focusing mechanism, we calculate the thermal conductivity of a high-pressure phase of polytetrafluoroethylene and also find a high thermal conductivity that would be only half as large without focusing.

In Chapter 3, we give an overview of the theory required to calculate hot electron noise and high field transport, and describe our numerical methods for obtaining these high field observables from first principles. Specifically, we combine an ab initio e-ph collision integral with the Boltzmann description of the behavior of electronic fluctuations. We obtain e-ph matrix elements using Wannier interpolation. Further, we modify the collision integral of the typical low-field BTE to account for the non-linearities that arise at high fields. We also include higher order e-ph scattering where an electron is scattered by two phonons in succession (2ph). We restrict our calculation to 2ph events where the intermediate state is close to the band energy to achieve computational tractability.

In Chapter 4, we calculate the drift velocity and hot electron noise in GaAs for electric fields up to 5 kV cm^{-1} including on-shell 2ph scattering. We start by discussing the deviation of noise and transport from low-field values, and explain the frequency dependence of the current PSD as coming from the quasi-elastic nature of scattering at moderate electric fields. At higher electric fields, we report that the on-shell 2ph processes we include produce significantly improved agreement with drift velocity measurements compared to the 1ph level of theory, and that the 2ph scattering noticeably increases the energy relaxation of the electron system which explains a long-standing discrepancy in the strength of intervalley scattering inferred from different experiments. The trends of hot electron noise in GaAs are not reproduced and we suggest that intervalley 2ph processes beyond our approximation may be necessary to obtain experimental agreement. Our work tests the limits of conventional ab initio theory and shows the utility of first principles calculations in revealing the mechanisms that determine transport phenomena.

Finally, in Chapter 5 we summarize our work and suggest directions for further investigation.

Chapter 2

THERMAL TRANSPORT AND PHONON FOCUSING IN COMPLEX POLYMER CRYSTALS

This chapter has been adapted, in part, from:

> Peishi Cheng, Nina Shulumba, and Austin J. Minnich (Sep 2019). Thermal transport and phonon focusing in complex molecular crystals: Ab initio study of polythiophene. In: *Phys. Rev. B* 100, pp. 094306. DOI: 10.1103/PhysRevB.100.094306.

As discussed in Ch. 1, one of the most notable successes in the ab initio thermal transport field was the prediction of high thermal conductivity in boron arsenide [19], which revised and expanded longstanding intuitions [6] about what materials constitute good thermal conductors. However, one of the criteria that was not controverted by the BAs calculation was association of simple unit cells with high thermal conductivity, which appears to be contradicted by the complex unit cells of polymer crystals.

The first studies of enhanced polymer thermal conductivity due to stretching were in polystyrene and polymethylmethacrylate [129]. Because of the ease at which polyethylene (PE) crystallizes, it became the primary focus for the following decades [26, 27, 130–133], with a few studies of other polymers like polyacetylene [134] or polypropylene [27]. While PE nanofibers had the highest reported thermal conductivities for polymers [28, 135], more sophisticated fabrication techniques were applied to produce macroscopic film samples with thermal conductivities greater than 60 $\mathrm{Wm^{-1}K^{-1}}$ [136, 137]. Experimental methods that can measure phonon mean free paths suggest that these films are still limited by finite crystal domain size and that the thermal conductivity can be increased further [138, 139]. Even for more complex molecular crystals with up to 48 atoms per unit cell, compared to the 12 atoms per unit cell in PE, thermal conductivities are still reported on the order of tens of $\mathrm{Wm^{-1}K^{-1}}$ [140].

To understand where polymer crystals fit into the picture of crystal thermal transport and what role phonon focusing plays in enhancing thermal con-

ductivity, we are interested in expanding the study beyond polyethylene. In molecular dynamics studies of polymers, calculations of many different materials allowed for the most important factors that determined morphology to be extracted and established with more certainty [39]. Thus, we seek to calculate the crystal thermal conductivity of various polymers beyond polyethylene to investigate the phonon behavior throughout the Brillouin zone that leads to the high uniaxial thermal conductivity of polymer crystals. In this chapter, we will calculate and discuss the thermal conductivity of polythiophene and the high-pressure thermal conductivity of polytetrafluoroethylene.

2.1 Interatomic force constants including quantum nuclear motion and finite temperature anharmonicity

The ab initio approach to thermal conductivity is based on computing the interatomic force constants (IFCs) using density functional theory (DFT) which we have noted must include the effects of quantum nuclear motion. To do so, we use the TDEP method for which we give an overview here. Once the IFCs have been computed, all the relevant phonon properties can be calculated using lattice dynamics and the Boltzmann transport equation. Lattice dynamics broadly refers to the study of phonons and the properties that can be derived from phonons. Phonons are the normal modes of a crystal and derived as plane wave solutions to the equations of motion. For thermal conductivity, one begins from the lattice Hamiltonian given below

$$\hat{H} = U_0 + \sum_i \frac{\mathbf{p}_i^2}{2m_i} + \frac{1}{2!}\sum_{ij}\sum_{\alpha\beta}\Phi_{ij}^{\alpha\beta}u_i^\alpha u_j^\beta + \frac{1}{3!}\sum_{ijk}\sum_{\alpha\beta\gamma}\Phi_{ijk}^{\alpha\beta\gamma}u_i^\alpha u_j^\beta u_k^\gamma \dots \tag{2.1}$$

where $\Phi_{ij}^{\alpha\beta}$ and $\Phi_{ijk}^{\alpha\beta\gamma}$ are the interatomic force constants which describe how the energy of the lattice changes with respect to displacements along all of the atomic degrees of freedom indexed by i, j, k for atoms in the unit cell and α, β, γ for the Cartesian directions. The $\Phi_{ij}^{\alpha\beta}$ are the harmonic IFCs which give the phonon frequencies, and the first three terms constitute the harmonic Hamiltonian for which phonons are the eigenstates. The $\Phi_{ijk}^{\alpha\beta\gamma}$ are the third order, anharmonic IFCs which are considered the perturbations to the harmonic Hamiltonian leading to phonon-phonon scattering. There are of course higher order terms which contribute to scattering through higher order perturbation theory and have been the focus of much recent study [22, 141, 142]. Various methods of first principles computation of phonons differ principally in their methods for obtaining the IFCs.

First principles approaches to IFCs since their development in the 1980s are essentially zero temperature approaches since DFT is a zero temperature method. Until recently, phonon methods could be grouped into two classes: the direct approach and the linear response approach. The direct approach, also called the "frozen phonon" approach, displaces atoms and calculates the change in energy to obtain force constants [143, 144], with a popular implementation given in Ref. [145]. The linear response approach based on linear response theory requires, in principle, expensive computation of the dielectric matrix, but in practice requires the solution of a more straightforward self consistent equation in a formulation known as density functional perturbation theory (DFPT) [18], with implementations across many electronic structure codes. Both of the methods described above calculate the interatomic force constants for displacements about the equilibrium positions in the zero temperature crystal structure obtained from DFT. However, this can be an issue when crystal structures of interest are dynamically unstable at 0 K such as $SrTiO_3$ [146]. These structures are stabilized at room temperature because the atoms have much larger thermal displacements that experience a potential which appears harmonic and stabilizes the vibrational excitation. The main concept of TDEP is to obtain the force constants that better reflect the vibration of nuclei in this finite temperature potential. We note that there are other methods to obtain finite temperature phonons with similar ideas to TDEP [147–149].

In contrast to the zero temperature phonon approach which is a Taylor expansion of the potential energy surface about the zero temperature equilibrium atomic positions, the TDEP method seeks a different set of interatomic force constants corresponding to a model Hamiltonian of the same form as Eq. 2.1 that best fit the potential effectively felt by the atoms at a given temperature. To do this, one obtains a set first-principles forces associated with atomic displacements that correspond to the temperature of interest and compares them to the forces that should result from the model Hamiltonian, which are given by the equation below:

$$f_{i\alpha}^{\mathrm{M}} = -\sum_{j\beta} \Phi_{ij}^{\alpha\beta} u_j^{\beta} - \frac{1}{2} \sum_{jk\beta\gamma} \Phi_{ijk}^{\alpha\beta\gamma} u_j^{\beta} u_k^{\gamma} + \dots \tag{2.2}$$

Here $f_{i\alpha}^{\mathrm{M}}$ are the forces on atoms given the model Hamiltonian of Eq. 2.1 with only third order anharmonic terms, and here the IFCs are the model IFCs. The TDEP method minimizes the difference between the model forces of Eq. 2.2 and the actual forces calculated with thermal displacements. This is done through a least squares solution for the IFCs, with the symmetry constraints of the crystal. The result is the set of force constants which best represent the Born-Oppenheimer energy surface sampled at the temperature of interest.

The original TDEP method sampled the energy surface using ab initio molecular dynamics (AIMD) simulation, obtaining the force-displacement data from various time steps in the simulation. A schematic of this process is given in Fig. 2.1 where the atoms have some displacement at a given time step, with the blue color around the mean position of the atoms representing the potential felt by the atoms as calculated from DFT. However, the force-displacement data at each time step is not independent of the previous time steps by definition, since the purpose of the molecular dynamics simulation is to track the evolution of the system through time. Since the fitting of TDEP benefits from time steps that are uncorrelated to provide more constraints on the linear system, computational inefficiencies arise due to correlated AIMD time steps which are redundant constraints in the solution of the IFCs. Most importantly, this method suffers from the classical nature of molecular dynamics which does not account for the zero point motion of atoms which are important in polymers.

Quantum nuclear motion with thermal snapshots

An approach which addresses both drawbacks involves the use of "thermal snapshots," where the force-displacement data are not obtained from AIMD, but instead by providing random displacements to the atoms based on expressions for the phonon mode amplitude that corresponds to a given temperature [51], and calculating the resulting forces using DFT in the particular snapshot. The snapshots idea has a long history [150], with applications to lattice dynamics given in Refs. [147, 148, 151]. The expression for the thermal average amplitude is given in Eq. 2.3 below.

$$\langle A_{i\lambda} \rangle = \sqrt{\frac{\hbar(2n_\lambda + 1)}{2m_i\omega_\lambda}} \tag{2.3}$$

Here, i indexes the atom, and λ is single index of phonon modes for unique combinations of wave vector and branch index. We also have n_λ for the Bose-

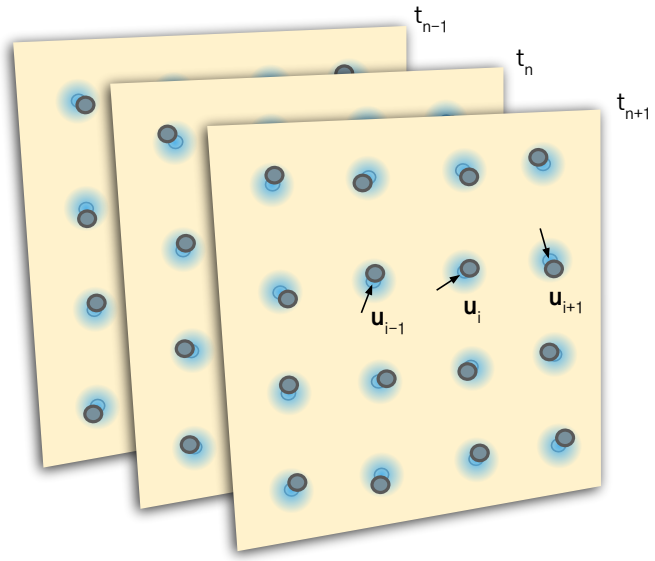

Figure 2.1: Schematic of the TDEP method which finds the best fit of force constants to a model Hamiltonian using the forces and displacements calculated from first principles. Each atom has some displacement $\mathbf{u}_i$. Each plane represents either a time step in an ab initio molecular dynamics simulation, or a thermal snapshot where the displacements obey quantum statistics. The blue represents the potential experienced by the atoms which leads to forces on the atoms.

Einstein occupation of a phonon with frequency ω_λ. The atoms have mass m_i. The real space atom displacements and velocities come from sums over the thermal amplitudes and eigenvectors for all phonons in the Brillouin zone. These thermal snapshots will be independent of one another due to the displacements coming from a random distribution, and will incorporate the quantum statistics directly, accounting for zero point motion, with the IFCs subsequently obtained in the same way as before. In the schematic of Fig. 2.1, we can imagine that instead of atomic positions coming from the classical equations of motion integrated from prior time steps in the simulation, each time step is now an uncorrelated force-displacement data set with displacements larger than in AIMD due to the quantum nuclear motion.

One additional complication arises from this method though. The expression for the quantum thermal amplitude depends itself on the phonon frequencies which we are trying to obtain, so the scheme requires iteration to self consistency. In TDEP, the initial iteration uses a simple pair potential for which

the phonon frequencies can be analytically obtained and are known to be stable [51]. Once iterated to self consistency, we have obtained the IFCs which correctly represent the potential energy surface experienced by the atoms including their zero point motion.

The fitting of TDEP can be thought of as a renormalization scheme where the TDEP phonons at a given temperature come from the harmonic part of an approximate representation of the true interatomic potential fitted up to a third order expansion. Thus, the TDEP phonons include anharmonicity to all orders felt by the thermal sampling of the atoms [152]. While this fitting may seem ad hoc, we note that a recent work provides a more rigorous theoretical derivation for phonon renormalization due to anharmonicity with explicit expressions based on the fourth order IFCs [142]. The approaches differ, but provide a justification for renormalization.

2.2 Thermal conductivity from the Boltzmann transport equation

Let us know discuss how thermal conductivity is calculated from the BTE to see how the IFCs determine the transport properties.

The thermal conductivity by Fourier's law is given by $\mathbf{J} = -\kappa \nabla T$ where J_α is the heat current in direction α which, for phonons, is given by the following expression:

$$J_\alpha = \frac{1}{V} \sum_\lambda \hbar \omega_\lambda v_{\lambda\alpha} n_\lambda \tag{2.4}$$

where n_λ is the non-equilibrium phonon occupation that arises due to a thermal gradient, and $v_{\lambda\alpha}$ is the phonon group velocity given by $\partial\omega_\lambda/\partial k_\alpha$, and the sum runs over all phonons indexed by λ for unique combinations of wave vector and branch index, as before. Since the phonon frequencies depend on the harmonic force constants, the group velocities are also affected. This is one way in which the TDEP phonons may give qualitatively different results from phonons calculated using a different method. The anharmonic force constants are involved in the scattering processes which determine the n at steady state. Obtaining the thermal conductivity requires solution of the BTE for the non-equilibruim phonon occupations.

Since thermal conductivity is a material property with no time dependence, we seek the solution to the Boltzmann equation at steady state meaning there

is no time dependence. Further, there is no force that can act directly on phonons, so the advection term also vanishes. The phonon BTE is thus given by the following form:

$$\frac{\mathbf{p}}{m} \cdot \nabla_{\mathbf{r}} n_\lambda = \left(\frac{\partial n_\lambda}{\partial t} \right)_{\text{coll}}. \tag{2.5}$$

We can manipulate this further by expressing the spatial gradient of the left hand side in terms of the thermal gradient, and using $\mathbf{p} = m\mathbf{v}$:

$$\frac{\partial n_\lambda}{\partial T} \mathbf{v}_\lambda \cdot \nabla_{\mathbf{r}} T = \left(\frac{\partial n_\lambda}{\partial t} \right)_{\text{coll}} \tag{2.6}$$

where on the left hand side, we have the diffusion of phonons due to a temperature gradient. We can assume that the temperature gradient is small so that the non-equilibrium phonon distribution is only a small deviation from the equilibrium distribution function: $n_\lambda = n_\lambda^0 + n_\lambda^1$ where n_λ^0 is the equilibrium Bose-Einstein occupation and n_λ^1 is the deviation. One consequence of this assumption is that the diffusion term of the left hand side can be approximated by simply the diffusion term corresponding to the equilibrium occupation:

$$\frac{\partial n_\lambda}{\partial T} \approx \frac{\partial n_\lambda^0}{\partial T} = \frac{\hbar \omega_\lambda}{k_{\text{B}} T^2} n_\lambda^0 (n_\lambda^0 + 1) \tag{2.7}$$

using the mathematical identity $n_\lambda^0 + 1 = n_\lambda^0 e^{\hbar\omega / k_{\text{B}} T}$. Now we discuss the form of the collision integral for phonons to see how the anharmonic IFCs enter into the expressions. We restrict our discussion to phonon-phonon scattering even though we include isotope scattering in our calculation, because the equations and derivations are somewhat analogous. The collision integral describes the increase or decrease of the phonon occupation due to scattering with other phonons. Let us consider a phonon-phonon scattering process where a phonon of index λ coalesces with another phonon λ' to form a phonon λ'', which has a probability expressed using Fermi's Golden Rule:

$$P_{\lambda\lambda' \to \lambda''} = \frac{2\pi}{\hbar} \left| \langle f | \hat{H}_3 | i \rangle \right|^2 \delta(E_f - E_i) \tag{2.8}$$

where the delta function ensures the conservation of energy, and $\langle f | \hat{H}_3 | i \rangle$ is the phonon scattering matrix element due to the anharmonic part of the Hamiltonian:

$$\hat{H}_3 = \frac{1}{3!}\sum_{ijk}\sum_{\alpha\beta\gamma}\Phi_{ijk}^{\alpha\beta\gamma}u_i^\alpha u_j^\beta u_k^\gamma. \tag{2.9}$$

A common coordinate transformation of the Hamiltonian into creation and annihilation operators allows us to calculate the matrix element algebraically, where the displacements are now expressed as a sum over all the normal modes of the system:

$$u_i^\alpha = \sqrt{\frac{\hbar}{2Nm_i}}\sum_\lambda \frac{\epsilon_\lambda^{i\alpha}}{\sqrt{\omega_\lambda}}e^{i\mathbf{q}\cdot\mathbf{r}_i}\left(\hat{a}_\lambda + \hat{a}_\lambda^\dagger\right) \tag{2.10}$$

where N is the number of unit cells, $\hat{a}_\lambda^\dagger$ is the creation operator, $\hat{a}_\lambda$ is the annihilation operator, and $\epsilon_\lambda^{i\alpha}$ is the α component of the eigenvector for phonon λ and atom i. Using the normal mode coordinates, we can write the product of the 3 displacements in Eq. 2.9 as:

$$\begin{aligned} u_i^\alpha u_j^\beta u_k^\gamma = \left(\frac{\hbar}{2N}\right)^{3/2}\frac{1}{\sqrt{m_i m_j m_k}}\sum_{\lambda\lambda'\lambda''}\frac{\epsilon_\lambda^{i\alpha}\epsilon_{\lambda'}^{j\beta}\epsilon_{\lambda''}^{k\gamma}}{\sqrt{\omega_\lambda\omega_{\lambda'}\omega_{\lambda''}}}e^{i\mathbf{q}\cdot\mathbf{r}_i + i\mathbf{q}'\cdot\mathbf{r}_j + i\mathbf{q}''\cdot\mathbf{r}_k} \\ \times\left(a_\lambda + a_\lambda^\dagger\right)\left(a_{\lambda'} + a_{\lambda'}^\dagger\right)\left(a_{\lambda''} + a_{\lambda''}^\dagger\right). \end{aligned} \tag{2.11}$$

Each matrix element will have terms like:

$$\begin{aligned} &\sum_{\lambda\lambda'\lambda''}\left\langle f\left|\left(a_\lambda + a_\lambda^\dagger\right)\left(a_{\lambda'} + a_{\lambda'}^\dagger\right)\left(a_{\lambda''} + a_{\lambda''}^\dagger\right)\right|i\right\rangle \\ &= \sum_{\lambda\lambda'\lambda''}\left\langle f\left|a_\lambda a_{\lambda'} a_{\lambda''}^\dagger\right|i\right\rangle = 3\sqrt{n_\lambda n_{\lambda'}(n_{\lambda''}+1)} \end{aligned} \tag{2.12}$$

where the factor of 3 comes from the multiplicity of the $a_\lambda a_{\lambda'} a_{\lambda''}^\dagger$ terms in the sum over all phonon indices, and we have used the following properties of the creation and annihilation operators [153]:

$$\begin{aligned} \hat{a}^\dagger|n\rangle &= \sqrt{n+1}\,|n+1\rangle \\ \hat{a}\,|n\rangle &= \sqrt{n}\,|n-1\rangle \\ \langle i|j\rangle &= \delta_{ij}. \end{aligned}$$

The interpretation of Eq. 2.12 is that the matrix element for a phonon coalescence process $\lambda + \lambda' \rightarrow \lambda''$ will only have nonzero components that are due to the components of the anharmonic term where phonons λ and λ' are annihilated and a phonon λ'' is created.

The expression for the matrix element now becomes:

$$\langle f|\hat{H}_3|i\rangle_{\lambda\lambda'\rightarrow\lambda''} = \frac{1}{2}\sum_{ijk}\sum_{\alpha\beta\gamma}\Phi_{ijk}^{\alpha\beta\gamma}\sqrt{n_\lambda n_{\lambda'}(n_{\lambda''}+1)}\left(\frac{\hbar}{2N}\right)^{3/2} \times \frac{\epsilon_\lambda^{i\alpha}\epsilon_{\lambda'}^{j\beta}\epsilon_{\lambda''}^{k\gamma}}{\sqrt{m_i m_j m_j}\sqrt{\omega_\lambda\omega_{\lambda'}\omega_{\lambda''}}}e^{i\mathbf{q}\cdot\mathbf{r}_i+i\mathbf{q}'\cdot\mathbf{r}_j+i\mathbf{q}''\cdot\mathbf{r}_k}. \tag{2.13}$$

We observe that the third order IFCs are involved in the matrix element, which is how the anharmonicity produces phonon-phonon scattering. The matrix element for the phonon coalescence process we have taken as an example involves sums over all possible combinations of the $3N_a$ atomic degrees of freedom (where N_a is the number of atoms per unit cell) where each term in the sum uses the eigenvectors of the 3 phonons involved in the process, taking only components corresponding to the unique combination of atomic degrees of freedom $(i\alpha, j\beta, k\gamma)$.

The resulting expression for the scattering rate using Eq. 2.8 for this particular phonon coalescence process is:

$$P_{\lambda\lambda'\rightarrow\lambda''} = \frac{\hbar^2\pi}{16N}n_\lambda n_{\lambda'}(n_{\lambda''}+1)\left|\Phi_{\lambda\lambda'\lambda''}\right|^2\delta(E_f - E_i) \tag{2.14}$$

where we have lumped the sums over the atomic degrees of freedom into $|\Phi_{\lambda\lambda'\lambda''}|^2$. The full expression for the collision integral for phonon-phonon scattering requires deriving expressions similar to Eq. 2.14 for phonon decay where $\lambda \rightarrow \lambda' + \lambda''$, and summing over all possible coalescence and decay processes for each phonon state λ.

To obtain the form of the BTE that is numerically solved, a substantial amount of algebra is involved which is detailed in Refs. [42, 154, 155]. It relies on a clever choice of the deviational occupation given by the following definitions:

$$n_\lambda^1 = \frac{\partial n_\lambda^0}{\partial \omega_\lambda} \frac{k_\mathrm{B} T}{\hbar} \Psi_\lambda$$
$$\Psi_\lambda = \mathbf{F}_\lambda \cdot \nabla_\mathbf{r} T \tag{2.15}$$

which are substituted into expressions like Eq. 2.14 The resulting collision integral is given by:

$$\left(\frac{\partial n_\lambda}{\partial t}\right)_\mathrm{coll} = \sum_{\lambda' \lambda''} W^+_{\lambda\lambda'\lambda''} \left(\Psi_\lambda + \Psi_{\lambda'} - \Psi_{\lambda''}\right) + \frac{1}{2} W^-_{\lambda\lambda'\lambda''} \left(\Psi_\lambda - \Psi_{\lambda'} - \Psi_{\lambda''}\right) \tag{2.16}$$

where the plus and minus superscripts of $W^+_{\lambda\lambda'\lambda''}$ and $W^-_{\lambda\lambda'\lambda''}$ correspond to phonon coalescence and decay, respectively. Their expressions resemble the rates of Eq. 2.14 but with slightly different normalization factors and using equilibrium phonon occupations:

$$W^+_{\lambda\lambda'\lambda''} = \frac{\hbar\pi}{4N} n^0_\lambda n^0_{\lambda'} (n^0_{\lambda''} + 1) \left|\Phi_{\lambda\lambda'\lambda''}\right|^2 \delta(\omega_\lambda + \omega_{\lambda'} - \omega_{\lambda''}) \tag{2.17}$$
$$W^-_{\lambda\lambda'\lambda''} = \frac{\hbar\pi}{4N} n^0_\lambda (n^0_{\lambda'} + 1)(n^0_{\lambda''} + 1) \left|\Phi_{\lambda\lambda'\lambda''}\right|^2 \delta(\omega_\lambda - \omega_{\lambda'} - \omega_{\lambda''}) \tag{2.18}$$

We see that the BTE is a set of linear equations on the Ψ_λ. The thermal conductivity can then be expressed in terms of the vector $\mathbf{F}_\lambda$ since the definition of Eq. 2.15 implies a deviational occupation that is linear with respect to a small temperature gradient, and the thermal conductivity is defined as the linear response coefficient of the material to a temperature gradient.

2.3 Thermal conductivity in crystalline polythiophene

Let us begin our study with crystalline polythiophene through an ab initio Boltzmann approach.

Computational parameters

We briefly discuss the parameters used in calculating the IFCs from TDEP and the thermal conductivity. We use a 5.0 Å cutoff for the second order interatomic force constants which yields convergence of the vibrational free energy within 0.1 meV per atom. We use a 3.0 Å cutoff for the third order

interatomic force constants. For a grid of comparable density, using an increased third order cutoff of 3.3 Å yields only a reduction of 4% in the thermal conductivity.

We use the VASP implementation of DFT [156–159] to calculate the forces. The plane wave energy cutoff was 800 eV with a reciprocal space mesh of 3 × 3 × 3 to sample the Brillouin zone. We incorporate van der Waals interactions with a non-local density functional [160–162] (commonly denoted vdw-DF) that captures long range correlation and has been tested for the polyethylene crystal [163]. Others have studied the performance of various non-local functionals for polymer crystals [164] and found that this functional, and an updated version, performed best in estimating the a and b lattice parameters. We note that the choice of functional can affect the computed value of the thermal conductivity [165]. Our choice of functional was motivated by the desire to include van der Waals interaction in a parameter free way. Eight iterations were required to obtain self-consistent force constants. A single iteration comprises the extraction of the force constants from the thermalized supercell and generation of the thermal displacements for the supercells used in the successive iteration. The supercell was composed of a 2 × 2 × 2 repetition of the orthorhombic unit cell for a total of 224 atoms.

The Boltzmann transport equation was solved iteratively on a 18 × 18 × 18 grid in the Brillouin zone with a tetrahedron integration method for energy conservation. The included scattering mechanisms are intrinsic anharmonic phonon-phonon scattering and isotopic scattering [166] from the natural isotope distribution. Convergence of the thermal conductivity was verified by calculating thermal conductivity for various q-grid densities and plotting the inverse of the grid density with thermal conductivity to extrapolate to infinite grid density. Using an anisotropic q-grid where the chain axis has a higher grid density, extrapolation yields a value of 201 $\mathrm{Wm^{-1}K^{-1}}$. Using an isotropic grid, extrapolation yields a value of 195 $\mathrm{Wm^{-1}K^{-1}}$. We report the value using the 18 × 18 × 18 grid since it is obtained using the densest grid calculated, and the value lies within the two extrapolated values.

Harmonic phonon properties of crystalline polythiophene

The structure of the PT unit cell is given in Figures 2.2(a-c). Figure 2.2(a) shows the chains extending along the z axis. The atoms in each chain are co-

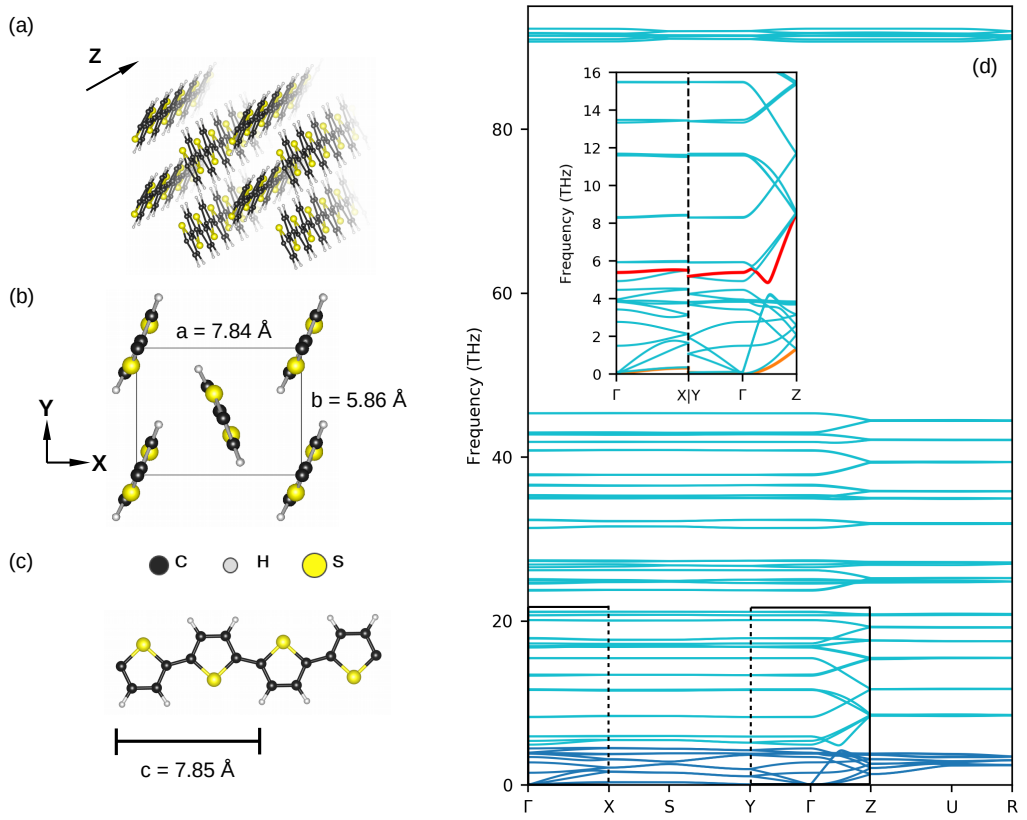

Figure 2.2: The structure and dispersion of polythiophene (PT). (a) Structure of a PT crystal with chains extending in the z axis. (b) View of the xy plane of the unit cell. There are two chains in each unit cell. Chains from the adjacent cell are shown. (c) Single polymer chain of PT showing that the length of unit cell in the chain axis is two thiophene chemical repeat units. (d) Calculated phonon dispersion of PT, showing numerous branches. The dark blue and light blue branches correspond to the spectral thermal conductivity of the acoustic-like and optic modes, respectively, as seen in Figure 2.3. Inset: The phonon dispersion along symmetry directions from Γ. The branches for which isoenergy contours are plotted later are highlighted in red (Figure 2.5a) and orange (Figure 2.5b).

valently bonded, while van der Waals bonding occurs between chains. Figure 2.2(b) shows the orthorhombic primitive cell which contains two such chains. The chains from adjacent cells are shown for reference. Figure 2.2(c) shows a single PT chain composed of the thiophene repeat units; a primitive cell contains two thiophene repeat units per chain. Our calculated lattice parameters from the relaxed structure are $a = 7.84$ Å, $b = 5.86$ Å, $c = 7.85$ Å for an orthorhombic unit cell. The lattice parameters from experiment are $a = 7.80$ Å, $b = 5.55$ Å, $c = 8.03$ Å also for an orthorhombic unit cell [167], corresponding to a mean absolute relative error of 2.78%.

The computed phonon dispersion for PT is given in Figure 2.2(d). The dispersion contains 84 branches corresponding to the degrees of freedom of the 28 atom primitive cell. The branches are highly dispersive in the $\Gamma - Z$ direction up to nearly 50 THz, whereas the branches are far less dispersive in the $\Gamma - X$ and $\Gamma - Y$ directions, becoming nearly dispersionless above 5 THz.

Temperature dependence and spectral thermal conductivity in polythiophene

Such a complex crystal would be expected to have a low thermal conductivity if considering only the phonon scattering phase space, which would be large given the numerous branches. For instance, the primitive cell of tetrahedrite contains 29 atoms per cell and has a thermal conductivity of around 1 $\mathrm{Wm^{-1}K^{-1}}$[168]. We calculate the chain-axis thermal conductivity of PT to be 198 $\mathrm{Wm^{-1}K^{-1}}$ at room temperature. This value is higher than both the room temperature thermal conductivity of silicon and the ab initio thermal conductivity of the simpler polyethylene crystal, which has only 12 atoms per unit cell [49]. The cross-chain thermal conductivity along the x and y axes are calculated as 8.3 and 7.3 $\mathrm{Wm^{-1}K^{-1}}$ at room temperature, respectively, a substantial thermal anisotropy which is expected for these elastically anisotropic polymer crystals.

The thermal conductivity versus temperature, as shown in Figure 2.3(a), was calculated by solving the Boltzmann transport equation at each temperature using the force constants generated at 300 K. While other works have independently calculated force constants for a grid of temperature and volume, such a calculation is computationally expensive for our system due to the size and complexity of the PT crystal. We calculated force constants on a grid of volumes at a single temperature (300 K) and determine the equilibrium volume

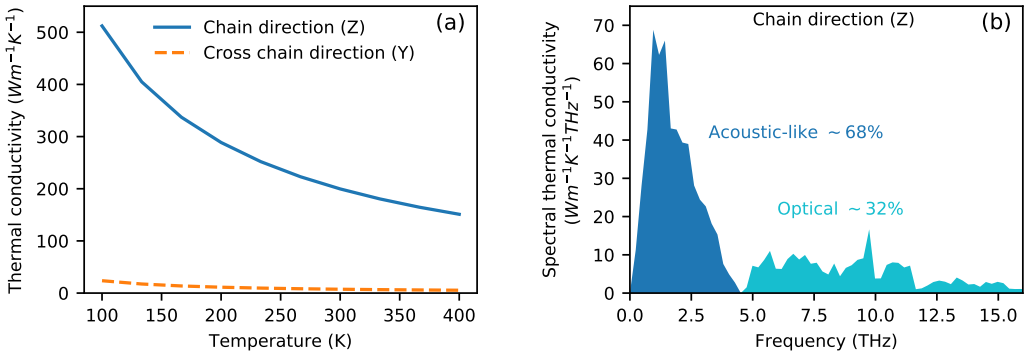

Figure 2.3: Thermal conductivity versus temperature and spectral thermal conductivity. (a) Thermal conductivity along the chain (blue solid line) and along the x axis perpendicular to the chains (orange dashed line) versus temperature using force constants obtained at 300 K. The polymer chains are oriented along the z axis (blue line). The chain-axis thermal conductivity is 198 $\mathrm{Wm^{-1}K^{-1}}$ at room temperature. (b) Spectral thermal conductivity versus phonon frequency along the chain axis. The contributions from acoustic-like modes and optic modes are highlighted in dark blue and light blue, respectively.

at this temperature by minimizing the Gibbs free energy. We then used the force constants at the equilibrium volume to calculate thermal conductivity at other temperatures. Given that the force constants are fixed, the trend shows the expected decrease of thermal conductivity with increasing temperature as our calculation includes only isotope and intrinsic anharmonic scattering.

Figure 2.3(b) shows the spectral thermal conductivity versus phonon frequency. Isolating purely acoustic modes below 5 THz is difficult because there is significant overlap in frequencies with some optical modes, as was also observed for polyethylene [49]. Thus, we denote the modes below 5 THz as acoustic-like modes, and all modes above 5 THz as optical modes. Greater than 96% of the thermal conductivity is due to phonon modes with frequencies below 16 THz, even though modes exist up to 92 THz. Around two thirds of the heat is conducted from the acoustic-like modes, with the remainder carried by the optical modes.

Comparison of PT thermal conductivity to an isotropic crystal

We next examine how the lifetimes and group velocities compare between PT and Si. The comparison with Si, an isotropic crystal with a lower but same

order of magnitude thermal conductivity, will reveal the importance of phonon focusing. We calculated the thermal conductivity of Si using the phonon properties generated by TDEP in Ref [169]. The phonon lifetimes versus frequency for PT and Si are shown in Figure 2.4(a). The results show that the lifetimes in PT are an order of magnitude lower than in Si over nearly the entire frequency range of 0-16 THz despite PT having the higher thermal conductivity. We can quantitatively assess how much heat is carried by individual modes over the entire spectrum of phonon lifetimes by examining thermal conductivity accumulation plots with respect to lifetime, shown in Figure 2.4(b). We observe that long lifetime modes in Si contribute significantly to the thermal conductivity, with over half of the thermal conductivity coming from modes with lifetimes greater than 50 ps. In contrast, in PT there are almost no modes contributing to thermal conductivity that have lifetimes greater than 50 ps. This comparison suggests that the lifetimes for these complex crystals are of the order expected of a crystal with a complex unit cell and thus high scattering rates.

Next, we present the group velocity magnitude versus frequency in Figure 2.4(c). We observe that PT possesses modes with higher group velocity modes than Si. To determine whether a higher group velocity magnitude by itself can be responsible for the high thermal conductivity of PT, we compute the RMS group velocity ($\sqrt{(\sum_\lambda v_\lambda^2)/N_\lambda}$). For PT, the value is 4.33 km s^{-1} below 18 THz, which is the frequency range containing 99% of the thermal conductivity. The value for Si is 3.46 km·s^{-1} below 13 THz, which is the corresponding frequency range containing 99% of the heat carrying modes. From these results alone, and without taking phonon focusing into account, how PT can have a higher thermal conductivity than Si despite having an order of magnitude lower lifetimes and only a slight increase in the RMS group velocity is not obvious.

PT is highly anisotropic and thus phonon focusing is expected to occur. A way to assess the strength of phonon focusing is to compare the RMS group velocity in the chain direction to the RMS group velocity magnitude. In PT, this RMS group velocity in the chain direction (0-18 THz) is 4.29 km s^{-1}, which is indeed very close to the RMS group velocity magnitude of 4.33 km s^{-1}. For Si, the RMS group velocity in the chain direction (0-13 THz) is 2.00 km s^{-1} which is far from the RMS group velocity magnitude of 3.46 km s^{-1}.

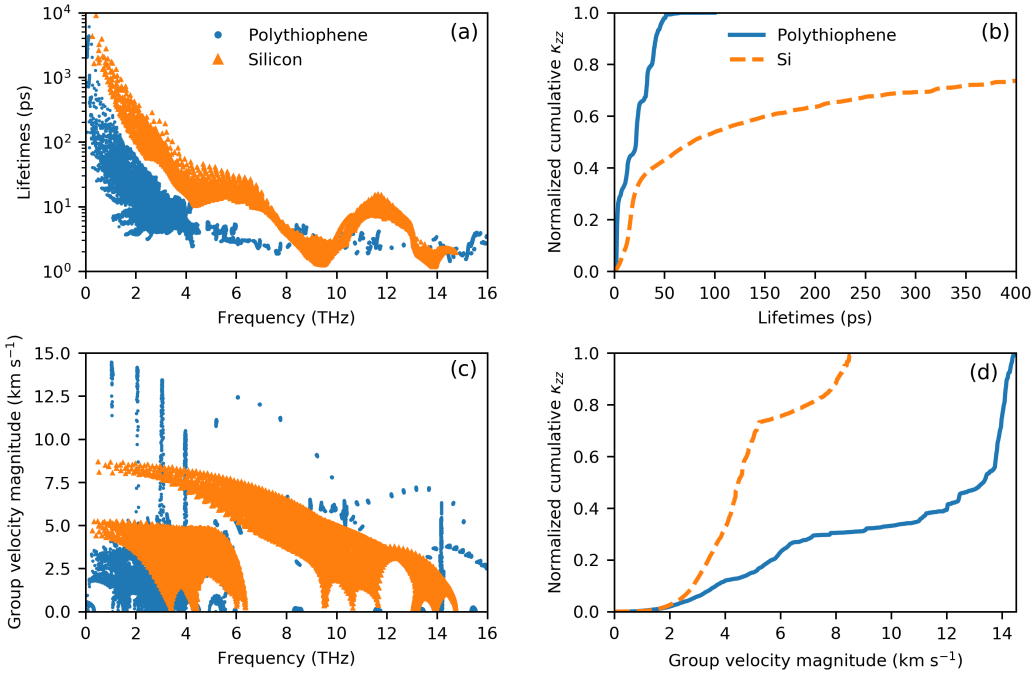

Figure 2.4: Phonon lifetimes and group velocities of PT and Si. (a) Phonon lifetimes versus frequency for PT (blue dots) and Si (orange triangles). (b) Thermal conductivity accumulation function versus lifetime. The thermal conductivity of PT is due almost entirely to modes with lifetimes less than 50 ps, in contrast to Si which has more than half of its thermal conductivity from modes with lifetimes longer than 100 ps. (c) Phonon group velocities along the chain axis (z) versus frequency of PT (blue dots) and Si (orange triangles). (d) Thermal conductivity accumulation function versus group velocity along the chain axis. Nearly two-thirds of the heat in PT is carried by modes with group velocity larger than the maximum group velocity in Si.

The effect of phonon focusing is also evident in Figure 2.4(d). Over half of the heat in PT is carried by modes with group velocity greater than 12 km s^{-1} because the highest group velocity modes correspond to the acoustic-like modes below 5 THz, which possess group velocity vectors oriented along the chain as well as the longest lifetimes in PT. However, optical modes also contribute substantially due to phonon focusing. While these modes possess the shortest lifetimes, as seen in the frequency range above 5 THz in Figure 2.4(a), phonon focusing allows these modes to overcome their low lifetimes to still contribute 32% of the total thermal conductivity. As a comparison, for Si we find that once the lifetimes become comparable to those in PT in the frequency range of 8-10 THz there is negligible contribution to thermal conductivity, despite

the group velocities in that range being near the maximum for Si, because of the lack of phonon focusing.

Isoenergy contours show dramatic phonon focusing

To further analyze the influence of phonon focusing, we plot isoenergy contours. We note that in contrast to previous work, our isoenergy contours are generated by calculating the dynamical matrix for a dense grid in the Brillouin zone using the ab initio force constants and subsequently plotting lines of equal frequency for a given plane in the Brillouin zone. Thus, they are valid beyond the typical frequency and wave vector ranges of isoenergy contours derived from continuum elasticity. The group velocity is the gradient of the frequency with respect to wave vector, so the group velocity vector is always normal to an isoenergy contour.

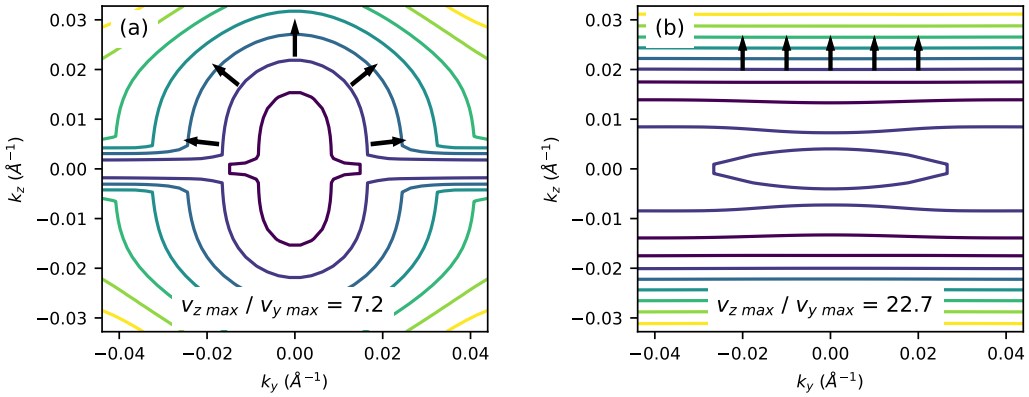

Figure 2.5: Isoenergy contours in PT. (a) The isoenergy contours of an acoustic branch with an anisotropy in the maximum group velocity ratio of 7.2 in PT for the $k_x = 0$ plane. The lines are contours of equal frequency. The arrows show the direction of the group velocity vector. The contours are similar to those Ref. [34] corresponding to the quasi-transverse acoustic branch. (b) The isoenergy contours of an optical branch with a much larger anisotropy ratio of 22.7. The group velocity of nearly all the modes are pointed along the chain axis. We observe a similar effect in other planes in the Brillouin zone for this branch, and for other optical branches with a large anisotropy ratio.

Figure 2.5(a) plots the isoenergy contours of a branch with a ratio of the largest group velocity along the chain axis to the largest group velocity along the cross-chain axis of 7.2, corresponding to the orange branch in the inset of Figure 2.2(d). The contours are similar to those in Ref. [34] corresponding to

the quasi-transverse acoustic branch. On the other hand, Figure 2.5(b) shows the isoenergy contours of an optical branch with an anisotropy ratio of 22.7, corresponding to the red branch in the inset of Figure 2.2(d). The contours reveal an exceptional degree of phonon focusing such that even for vibrations with wave vectors pointing almost completely orthogonal to the direction of the chain, the vibrational energy is still transported in the direction of the chain. We observe this effect throughout the Brillouin zone, irrespective of the plane for which the isoenergy contours are plotted. This phenomenon resembles the degree of focusing calculated for quasi-longitudinal acoustic branches [34, 35], but in PT the optical branches are also focused.

Thermal conductivity in hypothetical polymers with no phonon focusing

We quantitatively assess the importance of phonon focusing for the chain axis thermal conductivity by calculating the thermal conductivity of an isotropic version of PT in which the group velocity and wave vector are parallel. Note that only the direction of the group velocity is changed, but not the magnitudes of the group velocities and lifetimes. We find that the thermal conductivity of this isotropic crystal would be only 34 $Wm^{-1}K^{-1}$, confirming that the anisotropy is the key factor which underlies the high thermal conductivity. In fact, if we calculate the other extreme where the group velocity vectors of every mode is pointing along the chain direction, the thermal conductivity increases by only 7.5%. We performed this computation for the polyethylene crystal as well, finding an "isotropic" thermal conductivity for polyethylene of 67 $Wm^{-1}K^{-1}$, less than half of the actual calculated value. The extreme case of perfect focusing in the chain direction would yield only a 3.2% increase.

To further emphasize this conclusion, we plot the spectral thermal conductivity for the hypothetical isotropic PT as seen in Figure 2.6. In the frequency range where the acoustic-like modes previously contributed over 100 $Wm^{-1}K^{-1}$ (68% of the original thermal conductivity), there is now very little contribution, even though this frequency range contains modes with the largest group velocities and longest lifetimes in PT. In contrast, if we calculate this isotropic thermal conductivity for silicon, it is unchanged from the actual value.

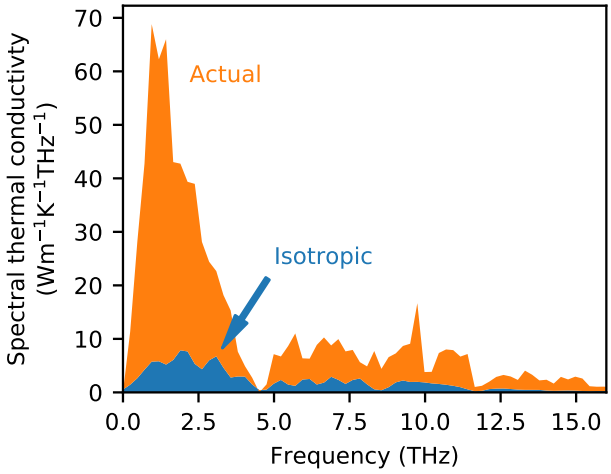

Figure 2.6: The spectral thermal conductivity versus frequency in the case where the group velocities are parallel to their wave vector (blue) compared to the actual (orange). Phonon focusing underlies the high thermal conductivity of PT, particularly for modes below 5 THz.

2.4 Discussion of prior work and heuristic understanding of high thermal conductivity in PT

We now discuss our results in the context of prior work on polymer crystals. First, many works use an average lifetimes or average mean free paths to analyze thermal transport in polymer crystals due to computational or experimental limitations [34, 140]. Using our ab initio calculations, we are able to assess the accuracy of these approximations. First, as in Figure 2.4(b), we find that the distribution of lifetimes for phonons that conduct heat is narrow, between 0-50 ps, so that assuming an average lifetimes is in fact a reasonable estimate. However, the estimate of an average mean free path is less accurate because the shortest lifetime modes can contribute significantly to thermal transport due to phonon focusing, while modes with group velocity approaching the maximum value possess the longest lifetimes. Thus the range of mean free paths relevant for heat transport spans 1 nm to 1 μm.

Second, we examine previous treatments of phonon focusing in anisotropic solids. Many previous works employed the Debye approximation because of the assumption of that acoustic phonons dominate the thermal transport [34, 35]. Our work demonstrates that phonon focusing has a dramatic effect on both acoustic and optical phonons for nearly all phonons regardless of wave

vector because dispersive optical modes persist throughout the thermal phonon frequencies. Consequently, future studies on thermal transport in polymers will have to be more cautious when interpreting results using simple models neglecting optical modes, since focusing allows optical phonons to contribute substantially to heat transport.

We note that the phonon focusing effect is expected to be more effective in quasi-1D materials compared to quasi-2D materials like graphite where the group velocities in the *ab* plane are similar because of covalent bonding between atoms in the plane, and thus the focusing largely exists only from anisotropy with the cross plane direction. In the quasi-1D case, both cross-chain directions have weak van der Waals bonding while the chain direction has strong covalent bonds, resulting in the focusing of an additional dimension of phonon modes and an enhanced chain-axis thermal conductivity. Indeed, we find that for the polarization shown in Figure 2.5(b), 87% of the modes have a group velocity vector that points less than 10 degrees away from the chain axis.

Let us also discuss the high value of thermal conductivity in PT from a more general, heuristic perspective to see where it stands with other crystals. If we consider the simple equation for thermal conductivity from the kinetic model presented in Ch. 1: Eq. 1.2, then we see that thermal conductivity is proportional to the phonon lifetime and to the square of the phonon group velocity. The roughly equivalent expression for the diagonal element of the thermal conductivity tensor, with knowledge of individual phonon properties in the crystal, is given below:

$$\kappa_{\alpha\alpha} = \frac{1}{V} \sum_{\lambda} c_{\lambda} v_{\alpha\lambda}^2 \tau_{\alpha\lambda}, \tag{2.19}$$

Where we have the same proportionalities, but the sum is over all phonon modes in the super cell of volume V, meaning that the atom density of the material is also a factor for thermal conductivity. Comparing the values of thermal conductivity of Si and PT, where our calculated value of thermal conductivity in Si is around 130 $\mathrm{Wm^{-1}K^{-1}}$, it may seem implausible that the thermal conductivity of PT is higher than in Si. If we consider phonon focusing only in a spherical Brillouin zone, we would only get a factor of 3 enhancement in thermal conductivity, while the lifetimes are 10 times lower in PT. Further, the RMS group velocities in PT are only about 25% larger

than in Si (4.33 km s^{-1} versus 3.46 km s^{-1}). Altogether, based on this rough estimate, the thermal conductivity of PT should be only 47% of the value of Si ($\frac{1}{10} \times 1.25^2 \times 3 = 0.47$).

However, here the use of average quantities for assessing thermal conductivity leads to misinterpretation. Although the RMS group velocity of PT is only 4.33 km s^{-1}, the highest group velocities are on the order of 15 km s^{-1}, which is to be expected given the covalent bonding of the carbon atoms along the polymer chain, leading to velocities comparable to that of diamond around 18 km s^{-1} [170]. These high group velocities also correspond to the highest lifetimes at low frequencies (c.f. Fig. 2.4a and 2.4c), which lead to substantial contributions to heat conduction. Furthermore, the phonon focusing factor can be greater than 3 since the PT Brillouin zone is orthorhombic and not spherical. The shape of the Brillouin zone also may explain the difference in the degree to which phonon focusing enhances thermal conductivity in PT versus PE, since PE has a shorter unit cell along the chain axis. The atom density in PT is also higher than in Si. The volume of the PT unit cell is 360.6 $Å^3$ with 28 atoms per unit cell which gives an atom density of 0.078 atoms/$Å^3$. In Si, there are 2 atoms per primitive cell with a volume of 41.0 $Å^3$ (our calculations used a lattice parameter of 5.474 Å from minimizing the free energy), which gives an atom density of 0.049 atoms/$Å^3$. This difference makes sense given the low packing factor of a diamond cubic structure. Therefore, PT has nearly a 60% higher atom density. Taken together, we can see how the thermal conductivity in an anisotropic crystal is more difficult to assess from a heuristic standpoint, but that the high value of thermal conductivity in PT compared to other crystals arises from many factors, where we have analyzed phonon focusing in particular.

Finally, we consider our prediction for PT in comparison to the predicted and experimentally realized thermal conductivities of other crystalline polymers. Prior computational works reported a range of 8 to 100 $Wm^{-1}K^{-1}$in polymer crystals lacking significant disorder [39] while the highest reported experimental values in macroscopic samples have ranged from 20 to around 65 $Wm^{-1}K^{-1}$[136, 137, 140]. Our work, along with other recent ab initio studies [49] indicate that the upper bound for polymer crystals is at least 160 $Wm^{-1}K^{-1}$. The steady progress in synthesis and associated increase in measured thermal conductivity in various material systems suggest that the pre-

dicted values from ab initio calculations can serve as useful guiding references, highlighting the utility of parameter free thermal conductivity calculations for the materials synthesis community. While defects and the difficulties of crystallizing polymers are substantial barriers to achieving high thermal conductivity, the generality of the phonon focusing mechanism in suggests that there are some crystalline polymers that, if synthesized at high enough quality, could have thermal conductivities exceeding 100 $Wm^{-1}K^{-1}$.

2.5 Thermal conductivity in the high pressure phase of polytetrafluoroethylene (PTFE)

The study of thermal conductivity under hydrostatic pressure has a history extending back nearly 100 years [171] due to its importance in geophysics and mineral physics, although the experimental setups necessary to conduct high quality measurements were not available until much later [172]. Pressure is often taken as the complementary thermodynamic state variable to temperature, so tuning pressure as well as temperature probes another axis of phase diagrams and allows us to see the effect of different crystal structures [172].

With the maturation of first-principles calculations, initial studies of the pressure dependence of thermal conductivity focused on materials relevant to geophysics like MgO [173]. The thermal conductivity versus pressure many materials like diamond [174], cubic BN [175], and Te compounds [176] were analyzed with respect to how the phonon dispersion and scattering rates changed with pressure. Other studies showed examples of the failure of conventional Leibfried–Schlomann (LS) theory predictions of the trend of thermal conductivity versus pressure due the use of phonon mode averaged quantities in the LS expressions that do not account for the change in scattering phase space with pressure [177]. Later calculations in BAs and BSb showed non-monotonic dependence of thermal conductivity versus pressure due to competing responses of three-phonon and four-phonon scattering [178]. In 2D materials, the thermal conductivity is often studied with respect to mechanical strain [179–182].

However, there are comparatively fewer studies of polymers under pressure. A polymer of interest is polytetrafluoroethylene (PTFE) which has a high pressure, high symmetry phase at modest pressures below 1 GPa [183, 184]. This phase is orthorhombic with the polymer chains forming a planar zigzag arrangement with identical symmetry to the ambient pressure phase of polyethy-

lene. However, at ambient pressure, the crystal structure of PTFE is helical with many chemical repeat units along the chain per unit cell. In this phase, even at high degrees of crystallinity, the absolute value of thermal conductivity is quite low, around 0.3 $Wm^{-1}K^{-1}$[185]. Given that PE has such a high thermal conductivity, it is worth considering whether PTFE will also have a higher thermal conductivity at high pressures in the high symmetry phase.

In a prior computational study of PTFE using MD, the thermal conductivity was calculated at ambient temperature and pressure but the PTFE crystal structure was initialized in the high pressure phase [39]. In that work, the low thermal conductivity of PTFE was attributed to segmental disorder due to dihedal axis rotations which prevented the formation of long range phonons. However disorder may also have been introduced as the material attempted to reach the helical crystal structure favored in ambient thermodynamic conditions. Thus, our interest in studying PTFE under pressure is less concerned with the particular pressure dependence, but rather its potential for high thermal conductivity given the similarity of the high pressure phase to the PE crystal structure, and the potential to further generalize the phonon focusing mechanism in quasi-1D materials.

To study materials under pressure, let us first define pressure which can be obtained by one of the Maxwell relations:

$$P = -\left(\frac{\partial F}{\partial V}\right)_T \tag{2.20}$$

where F is the Helmholtz free energy which includes the phonon free energy calculated using the canonical partition function.

Since the total free energy requires the phonons, sampling a large number of volumes involves significant computational expense. We take the typical approach of calculating phonons for a small number of volumes and then fitting an equation of state to the free energy which allows us to obtain pressure through an analytical derivative of this equation of state. We select 5 volumes and relax atom positions and unit cell parameters while keeping the cell volume fixed. We then calculate the phonons at 300 K. We fit a Birch-Murnaghan equation of state (EOS) [186]. From this fit, we can select a volume, and thus pressure, of interest for the thermal conductivity calculations. The free

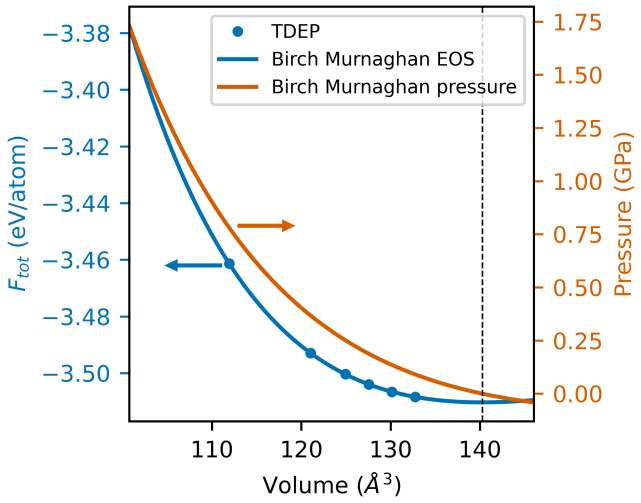

Figure 2.7: Helmholtz free energy and pressure versus volume in PTFE. The circles correspond to the free energies from the actual TDEP calculation. The blue curve corresponds to the best fit of a Birch Murnaghan equation of state (EOS). The red curve is the pressure corresponding to the volume, given by Eq. 2.20. The vertical dashed line corresponds to the volume of zero pressure

energy calculated from TDEP, the Birch-Murnaghan EOS fit to these TDEP free energies, and the corresponding pressure are shown in Fig. 2.7.

We note that when we attempt to calculate IFCs for the unit cells of lower pressure, some branches show unstable phonons meaning the structure is not dynamically stable, consistent with the phase diagram which indicates a helical phase for pressures below 0.6 GPa [184].

For the thermal conductivity calculations, we select a volume of 111.9 $Å^3$ corresponding to a pressure of 0.781 GPa. The phonon dispersion and unit cell parameters corresponding this volume are shown in Fig. 2.8. We note that in this structure, we have aligned the chains along the X axis. The crystal structure is almost identical to the PE crystal structure at ambient pressure, except with fluorine atoms in the place of the hydrogen atoms of PE. The a lattice parameter is much shorter in this structure than in PT due to short and simple chemical repeat units of PTFE. As a result, the $\Gamma - X$ path in the BZ is much longer in this structure. The phonon dispersion shows that there are many highly dispersive branches along the $\Gamma - X$ path and other paths along that direction ($S - Y$ and $Z - U$). As in PT, the optical branches along the X direction are highly dispersive all the way up to the highest frequency phonons

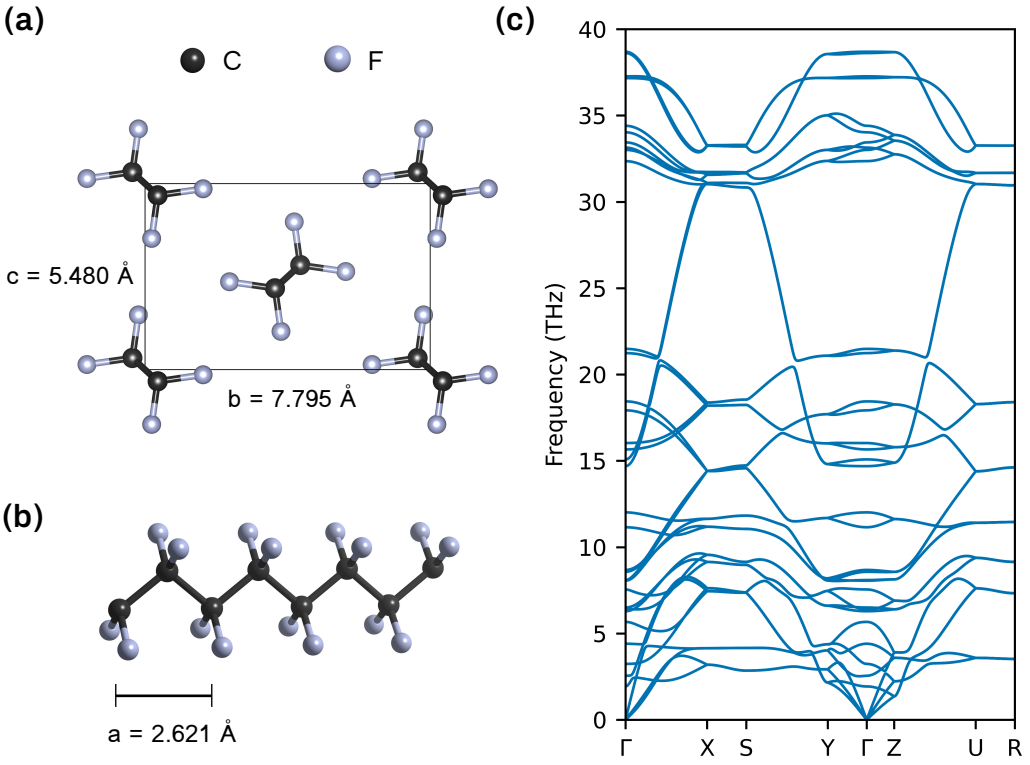

Figure 2.8: The crystal structure and dispersion of PTFE. Note that the PTFE chains are extended along the X axis, in contrast to PT where the chains are extended along the Z axis. Since the monomer units of PTFE are much shorter than in PT, the a axis of the unit cell is much shorter in PTFE despite both polymers having 2 chemical repeat units per unit cell. In the dispersion, we can see highly dispersive modes along the Γ-X direction. Note the absence of modes around 90 THz due to the lack of hydrogen atoms in PTFE.

around 40 THz. In contrast, along the non-chain directions, the branches are flat after 5 THz.

This phonon dispersion suggests that we will see substantial phonon focusing in this material as well. We obtain phonons with second order force constants including neighbor atoms up to 6Å away and a real space cutoff of 3Å for the third order anharmonic force constants. We calculate the thermal conductivity using an anisotropic q-grid of $27 \times 19 \times 19$. The thermal conductivity is 48.3 $\mathrm{Wm^{-1}K^{-1}}$ at room temperature at a pressure of 0.781 GPa. This is an increase in the thermal conductivity of over 3 orders of magnitude compared to the low pressure phase. In some ways, this increase is not too surprising since it is known that pressure induced phase transitions can significantly alter

the thermal conductivity, but typically phase transitions decreases thermal conductivity [172, 187].

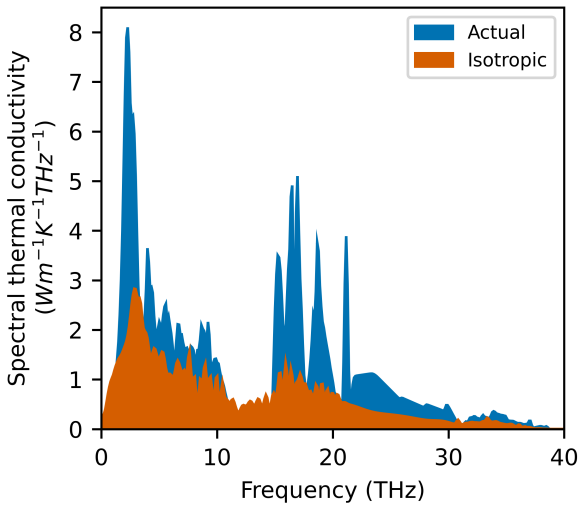

Figure 2.9: Isotropic and actual spectral thermal conductivity for PTFE. The isotropic thermal conductivity is 25.3 $Wm^{-1}K^{-1}$ compared to the actual thermal conductivity of 48.3 $Wm^{-1}K^{-1}$.

To see the extent to which phonon focusing affects the thermal conductivity, we again calculate the isotropic thermal conductivity with group velocity magnitudes unchanged but group velocity vectors aligned with the wave vector. The resulting thermal conductivity is 25.3 $Wm^{-1}K^{-1}$, almost half the actual value. The decomposition of thermal conductivity versus frequency is shown for the actual case against this isotropic case in Fig. 2.9. As in PT, we see that there are non-negligible contributions to the thermal conductivity up to 40 THz which includes many optical modes. We attribute this again to the phonon focusing of the optical modes. For the opposite case of a fully focused PTFE, we see only a 4.1% increase in the thermal conductivity, indicating that the degree of phonon focusing is close to maximal. We thus have further evidence that phonon focusing is of vital importance in setting the high thermal conductivity of polymer crystals by showing that it also has a dramatic effect on the thermal conductivity of PTFE.

2.6 Summary

We calculated the first-principles thermal conductivity including quantum nuclear effects and finite temperature anharmonicity in crystalline unsubstituted

polythiophene and in the high-pressure phase of polytetrafluoroethylene. We obtain a thermal conductivity of 198 $Wm^{-1}K^{-1}$ for crystalline PT at room temperature and 48 $Wm^{-1}K^{-1}$ for PTFE at room temperature and 0.6 GPa. We find that exceptional phonon focusing of both acoustic and optical branches that affects nearly all of the modes in the Brillouin zone permits even modes with short, picosecond range lifetimes to contribute to conduction. Our work indicates that the intrinsic upper bound for the chain axis thermal conductivity of polymer crystals may rival the values of metals and semiconductors, as phonon focusing occurs in any anisotropic crystal.

Looking at the degree to which phonon focusing enhances the thermal conductivity in PT, PE, and PTFE compared to their hypothetical isotropic equivalent, we can see that the focusing factor is between 2 to 5, which is not so different from the value of around 3 expected for just a spherical Brillouin zone and analysis for acoustic modes only [35]. However, when assessing the intrinsic upper limits, first-principles calculations are especially well suited, because they reveal the quantitative balance of all of the factors relevant to thermal conductivity like atom density, mode specific lifetimes and velocities, and of course phonon focusing.

The field of first principles phonon calculations is now around 15 years old, and seeks to understand the physics and expand the materials boundaries at the extremes of thermal conductivity. For high thermal conductivity, we have already mentioned the success of BAs, while achieving the lowest possible thermal conductivity is important in applications like thermoelectrics and thermal barrier coatings [188]. Polymers have been studied for both extremes of low [189] and high thermal conductivity. For the first-principles thermal transport field, the primary approach to achieving high thermal conductivity has been to increase the phonon lifetime by reducing phonon-phonon scattering. Our study of intrinsic thermal conductivity of polymers shows that another possible route to high thermal conductivity is through phonon focusing in quasi-1D, highly anisotropic solids.

Chapter 3

THEORY AND METHODS FOR HIGH-FIELD TRANSPORT AND ELECTRONIC NOISE FROM FIRST PRINCIPLES

This chapter has been adapted, in part, from:

> Alexander Y. Choi, Peishi Cheng, Benjamin Hatanpää, and Austin J. Minnich (Apr 2021). Electronic noise of warm electrons in semiconductors from first principles. In: *Phys. Rev. Materials* 5, pp. 044603. DOI: 10.1103/PhysRevMaterials.5.044603
>
> Peishi Cheng, Shi-Ning Sun, Alexander Y. Choi, and Austin J. Minnich (Jan 2022). High-field transport and hot electron noise in GaAs from first principles: role of two-phonon scattering. In: arXiv:2201.11912

The goal of this chapter is to establish the theory and equations for the calculation of high-field transport and hot electron noise from first principles. Let us begin with a brief background on the prior literature for these topics.

Early work on high-field charge transport in semiconductors focused on dielectric breakdown in polar semiconductors, establishing an early treatment of electronic interactions with polar longitudinal optical phonons [190]. Subsequent experimental work focused on the nonlinear trends of drift velocity versus electric field in elemental semiconductors [63–65], the Gunn effect in III-V semiconductors [66, 67], measurement of the negative differential resistance region associated with the Gunn effect [191–193], and measurement of the high frequency AC mobility that provided insight into the energy relaxation time [194–197]. Initial theoretical studies using the Boltzmann equation employed model distribution functions [198, 199] or numerically solved the BTE under various approximations [200–202] to investigate high-field transport phenomena such as energy relaxation and intervalley scattering processes. Beginning in the 1970s, Monte Carlo calculations became the predominant method for modeling high-field transport [203–205], with an important review given in Ref. [68]. First-principles studies of high field transport from first principles have been reported by time stepping the BTE to steady state [95], or by the Monte Carlo method [96], but not by direct solution to the high-field, steady state BTE.

The history of the theoretical description of fluctuations about a non-equilibrium steady-state was briefly discussed in Ch. 1, and expanded here. As noted previously, in 1935, Leontovich used kinetic theory to examine velocity fluctuations of a non-equilibrium gas [106]. Around 20 years later, Wannier established the definition of a diffusion coefficient for transport about a non-equilibrium steady state [206]. Hashitsume considered a microscopic description of occupancy fluctuations about a steady distribution using the Fokker-Planck equation with a random source term [207]. In analogy with earlier works on fluctuational Maxwell equations, Kadomotsev introduced Langevin sources into the Boltzmann equation [208]. Shortly thereafter, Price derived the fluctuation-diffusion relation for spatially homogeneous fluctuations, linking Wannier's diffusion coefficient to the spectral density of current fluctuations even outside of equilibrium [107]. In the same year, Lax formulated a general kinetic theory of fluctuations for a Markovian system [209]. Throughout the 1960s, Gantsevich and co-workers applied Lax's kinetic theory to dilute gases for which the evolution of the one particle distribution function is governed by the linear Boltzmann Equation [108]. Their technique, termed the "method of moments," demonstrated how to compute the spectral density of current fluctuations using only the solutions of the linear Boltzmann equation. Concurrently with Gantsevich, starting from Kadomotsev's Boltzmann-Langevin equation, Kogan and Shul'man developed a Langevin treatment of the current density fluctuations [210]. Lax, van Vliet, and Kogan and Shul'man independently confirmed that the method of moments and the Langevin approach are equivalent [211–213].

Numerical studies of noise proliferated around the same time that Monte Carlo simulations were used to study high-field transport, as they could also be used simulate the real time trajectories of electrons to calculate non-equilibrium diffusion and thus PSD [214]. Initial calculations in GaAs primarily reported that the high-field diffusion coefficient differed substantially from that predicted using the Einstein relation [215, 216], which is to be expected as the Nyquist relation is no longer valid and the PSD is an independent transport observable. Later Monte Carlo calculations [114, 115, 217] and analytical models [218–220] of transport in GaAs used PSD as an additional observable to study intervalley processes and their role in the Gunn effect and intervalley diffusion. Calculations of PSD were also made in Si [221–224], and other compound semiconductors [225–227]. The most recent works studies of noise focus

on the effect of short channels [228] or impurities [229] on PSD at cryogenic temperatures, noise in modern heterostructure devices [230, 231], and PSD in graphene [232, 233]. However, as with the study of high-field transport, a first-principles framework with no adjustable parameters for the calculation of noise is desirable.

3.1 Boltzmann equation for charge transport

We are interested in charge transport in semiconductors studied using the BTE. In contrast to the BTE for phonon transport where no forces act on the phonons, we are interested in studying how charge carriers behave under the influence of an electric field. We therefore assume spatial homogeneity. The BTE with no diffusion and only force term, with the same variables as Eq. 1.3 is given as:

$$\frac{\partial f}{\partial t} + \mathbf{F} \cdot \nabla_{\mathbf{p}} f = \left(\frac{\partial f}{\partial t} \right)_{\text{coll}} \tag{3.1}$$

To manipulate this into the form we want, let us first consider wave vectors instead of momentum where we have $\mathbf{p} = \hbar\mathbf{k}$ by the de Broglie relation. Our gradient must be calculated for wave vectors in the first Brillouin zone. The force on electrons due to the electric field is given by $\mathbf{F} = e\mathbf{E}$ where e is the elementary charge, and $\mathbf{E}$ is the electric field vector. Finally, we write the collision integral as a function of the electron occupation since the scattering due to Fermi's Golden Rule depends on the density of the initial and final states, making the collision integral a function of the solution itself. Thus the charge BTE that we are interested in is:

$$\frac{\partial f_{m\mathbf{k}}}{\partial t} + \frac{e\mathbf{E}}{\hbar} \cdot \nabla_{\mathbf{k}} f_{m\mathbf{k}} = \mathcal{I}[f_{m\mathbf{k}}] \tag{3.2}$$

Here, $f_{m\mathbf{k}}$ is occupation of the electron state at wave vector $\mathbf{k}$ with band index m, and e is the fundamental charge. $\mathcal{I}$ is the collision integral that describes scattering experienced by electrons. As discussed in Ch. 1, the dominant interaction near room temperature for non-degenerate carrier concentrations is electron-phonon scattering [70]. When solving for charge transport observables, we often consider the system at steady state where the time derivative term vanishes by definition, and the solution of the Boltzmann equation is the non-equilibrium steady-state distribution function $f^s_{m\mathbf{k}}$. Our work focuses on

the conduction band of GaAs for which there are no interband transitions in the energies of interest, so we omit the electron band indices in the remaining equations for simplicity.

One of the most important charge transport observables is the DC conductivity, defined by $J^\alpha = \sum_\beta \sigma^{\alpha\beta} E^\beta$ where $\mathbf{J}$ is the current density due to the electric field. The current density can be expressed as a sum over all electron occupations:

$$\mathbf{J} = \frac{2e}{V_0} \sum_{\mathbf{k}} \mathbf{v}_{\mathbf{k}} f^s_{\mathbf{k}} \tag{3.3}$$

Here, V_0 is the volume of the supercell, $\mathbf{v}_{\mathbf{k}}$ is the group velocity of the electron at state $\mathbf{k}$, and the factor of 2 comes from the assumption of spin degeneracy. So we can see that obtaining the conductivity is a matter of solving the BTE for the distribution function.

Next, let us discuss the form of the collision integral with scattering from electron-phonon interactions. The transition rates based on Fermi's Golden Rule are given by [1]:

$$\mathcal{I}[f_{\mathbf{k}}] = -\frac{2\pi}{\hbar} \frac{1}{N} \sum_{\nu\mathbf{q}} |g_{\mathbf{k},\nu\mathbf{q}}|^2 \left(\delta(\epsilon_{\mathbf{k}} - \hbar\omega_{\nu\mathbf{q}} - \epsilon_{\mathbf{k}+\mathbf{q}}) H^{\text{em}} + \delta(\epsilon_{\mathbf{q}} + \hbar\omega_{\nu\mathbf{q}} - \epsilon_{\mathbf{k}+\mathbf{q}}) H^{\text{abs}} \right) \tag{3.4}$$

where the sum is over phonon wave vector $\mathbf{q}$ and phonon branch indices ν for scattering phonons which satisfy momentum conservation, the delta functions ensure energy conservation, and $g_{\mathbf{k},\nu\mathbf{q}}$ is the e-ph matrix element calculated from first principles for a given scattering process. N is the total number of $\mathbf{q}$-points sampled from the Brillouin zone. H^{em} and H^{abs} weight the scattering probabilities to account for the electron and phonon occupations and are given below:

$$\begin{aligned} H^{\text{em}} &= f_{\mathbf{k}}(1 - f_{\mathbf{k}+\mathbf{q}})(N_{\nu\mathbf{q}} + 1) - (1 - f_{\mathbf{k}}) f_{\mathbf{k}+\mathbf{q}} N_{\nu\mathbf{q}} \\ H^{\text{abs}} &= f_{\mathbf{k}}(1 - f_{\mathbf{k}+\mathbf{q}}) N_{\nu\mathbf{q}} - (1 - f_{\mathbf{k}}) f_{\mathbf{k}+\mathbf{q}}(N_{\nu\mathbf{q}} + 1) \end{aligned} \tag{3.5}$$

We can see that the collision integral itself depends on the distribution function we are trying to solve for, and that the dependence is, in general, a nonlinear function of the distributions themselves.

A common way to make progress on this nonlinearity is to write the distribution functions as expansions about the equilibrium, Fermi-Dirac distribution $f^0_{\mathbf{k}}$ with a deviational occupation $\Delta f_{\mathbf{k}}$ so that the total electron occupation is $f_{\mathbf{k}} = f^0_{\mathbf{k}} + \Delta f_{\mathbf{k}}$. At low fields, we can drop higher order terms of the form $\mathcal{O}(\Delta f^2)$. To solve at high electric fields, we need to move past this approximation, but the expressions before dropping higher order terms are useful for understanding the approach to the collision integral at high fields, so we show it here.

As an example, consider the expression for the emission weight H^{em}. The expressions for the absorption weight will be similar. After substituting the definition of the electron distribution expanded about equilibrium, we have for phonon emission:

$$\begin{aligned} H^{\text{em}} =& (f^0_{\mathbf{k}} + \Delta f_{\mathbf{k}})(1 - f^0_{\mathbf{k+q}} - \Delta f_{\mathbf{k+q}})(N_{\nu\mathbf{q}} + 1) \\ & - (1 - f^0_{\mathbf{k}} - \Delta f_{\mathbf{k}})(f^0_{\mathbf{k+q}} + \Delta f_{\mathbf{k+q}})N_{\nu\mathbf{q}} \end{aligned} \tag{3.6}$$

Then, grouping similar terms and without removing any higher order terms, we get:

$$\begin{aligned} H^{\text{em}} = & \Delta f_{\mathbf{k}} \Big[(1 - f^0_{\mathbf{k+q}} - \Delta f_{\mathbf{k+q}})(N_{\nu\mathbf{q}} + 1) + (f^0_{\mathbf{k+q}} + \Delta f_{\mathbf{k+q}})N_{\nu\mathbf{q}} \Big] \\ & - \Delta f_{\mathbf{k+q}} \Big[f^0_{\mathbf{k}}(N_{\nu\mathbf{q}} + 1) + (1 - f^0_{\mathbf{k}})N_{\nu\mathbf{q}} \Big] \\ & + f^0_{\mathbf{k}}(1 - f^0_{\mathbf{k+q}})(N_{\nu\mathbf{q}} + 1) - (1 - f^0_{\mathbf{k}})f^0_{\mathbf{k+q}}N_{\nu\mathbf{q}} \end{aligned} \tag{3.7}$$

Often, the e-ph collision integral is solved under the assumption of constant lattice temperature, meaning that the phonon occupations are equal to the Bose-Einstein function $N^0_{\nu\mathbf{q}}$ for the temperature of interest. In this case, the third line with terms not grouped with $\Delta f_{\mathbf{k}}$ or $\Delta f_{\mathbf{k+q}}$ will vanish due to identities based on conservation of energy. Recall the mathematical identities that $(1 - f^0_{\mathbf{k}}) = e^{\epsilon_{\mathbf{k}}/k_{\text{B}}T} f^0_{\mathbf{k}}$, and $(N^0_{\nu\mathbf{q}} + 1) = e^{\hbar\omega_{\nu\mathbf{q}}/k_{\text{B}}T} N^0_{\nu\mathbf{q}}$. Thus the terms on the third line of Eqn. 3.7 become:

$$\begin{aligned} & f^0_{\mathbf{k}}(1 - f^0_{\mathbf{k+q}})(N^0_{\nu\mathbf{q}} + 1) - (1 - f^0_{\mathbf{k}})f^0_{\mathbf{k+q}}N^0_{\nu\mathbf{q}} \\ & \qquad = e^{(\epsilon_{\mathbf{k+q}} + \hbar\omega_{\nu\mathbf{q}})/k_{\text{B}}T} f^0_{\mathbf{k}} f^0_{\mathbf{k+q}} N^0_{\nu\mathbf{q}} - e^{\epsilon_{\mathbf{k}}/k_{\text{B}}T} f^0_{\mathbf{k}} f^0_{\mathbf{k+q}} N^0_{\nu\mathbf{q}} \end{aligned}$$

The expression equals zero due to conservation of energy for the phonon emission process since $\epsilon_{\mathbf{k}} = \epsilon_{\mathbf{k+q}} + \hbar\omega_{\nu\mathbf{q}}$.

After eliminating the third line of Eq. 3.7 and simplifying the expressions within the square brackets, we obtain the emission weight expression for this collision integral as

$$H^{\text{em}} = \Delta f_{\mathbf{k}}\left[N_{\nu\mathbf{q}} + 1 - f^0_{\mathbf{k+q}} - \Delta f_{\mathbf{k+q}}\right] - \Delta f_{\mathbf{k+q}}\left[f^0_{\mathbf{k}} + N_{\nu\mathbf{q}}\right] \tag{3.8}$$

We note here that this is the fully non-linear weight for phonon emission, with only algebraic simplifications. The only nonlinear term corresponds to the $-\Delta f_{k+q}$ term inside the first set of square brackets, and we have arbitrarily chosen to group it with the Δf_k term, but could also group it with the Δf_{k+q} term.

Applying a similar analysis yields the following expression for the fully non-linear weight for phonon absorption:

$$H^{\text{abs}} = \Delta f_{\mathbf{k}}\left[N_{\nu\mathbf{q}} + f^0_{\mathbf{k+q}} + \Delta f_{\mathbf{k+q}}\right] - \Delta f_{\mathbf{k+q}}\left[N_{\nu\mathbf{q}} + 1 - f^0_{\mathbf{k}}\right] \tag{3.9}$$

Let us now discuss how these weights are simplified in the low-field case.

Low field approximations to the BTE

Electrical mobility is often of interest in the region where the response of the system is linear with respect to the electric field, so the linear response coefficient corresponds to application of low electric fields, which allows simplification to the BTE. The following derivation follows largely from Ref. [73].

If we reasonably assume that at low-fields we have $\Delta f_{m\mathbf{k}} \ll f^0_{m\mathbf{k}}$, then we simply neglect higher order terms of the form $\Delta f_{\mathbf{k}} \Delta f_{\mathbf{k+q}}$ in Eqs. 3.8 and 3.9 which gives us a collision integral that is linear in the Δf. The weights associated with this linearization are:

$$\begin{aligned} \hat{H}^{\text{em}} &= \Delta f_{\mathbf{k}}(N_{\nu\mathbf{q}} + 1 - f^0_{\mathbf{k+q}}) - \Delta f_{\mathbf{k+q}}(N_{\nu\mathbf{q}} + f^0_{\mathbf{k}}) \\ \hat{H}^{\text{abs}} &= \Delta f_{\mathbf{k}}(N_{\nu\mathbf{q}} + f^0_{\mathbf{k}}) - \Delta f_{\mathbf{k+q}}(N_{\nu\mathbf{q}} + 1 - f^0_{\mathbf{k+q}}) \end{aligned} \tag{3.10}$$

Another consequence of the assumption that $\Delta f_{m\mathbf{k}} \ll f^0_{m\mathbf{k}}$ is that the electric field term can be approximated as coming from only the effect of the field on the equilibrium occupation, which leads to an analytical expression:

$$\nabla_{\mathbf{k}} f_{\mathbf{k}} \approx \nabla_{\mathbf{k}} f^0_{\mathbf{k}} = \left(\frac{df^0_{\mathbf{k}}}{d\epsilon_{\mathbf{k}}}\frac{d\epsilon_{\mathbf{k}}}{d\mathbf{k}}\right) = -\frac{\hbar}{k_B T}\mathbf{v}_{\mathbf{k}} f^0_{\mathbf{k}}(1 - f^0_{\mathbf{k}}) \tag{3.11}$$

Using this approximation, with the assumption of steady state $\frac{\partial f_{\mathbf{k}}}{\partial t} = 0$, and substituting the linearized weights of Eq. 3.10 into the collision integral, we obtain the low-field BTE:

$$\begin{aligned}\frac{e\mathbf{E}}{k_B T} \cdot \mathbf{v}_{\mathbf{k}} f^0_{\mathbf{k}}(1 - f^0_{\mathbf{k}}) = &\frac{2\pi}{\hbar}\frac{1}{N}\sum_{\nu\mathbf{q}} |g_{\mathbf{k},\nu\mathbf{q}}|^2 \Big[\\ &\left(\delta^{\text{abs}}_{\mathbf{k},\nu\mathbf{q}}(N_{\nu\mathbf{q}} + f^0_{\mathbf{k}+\mathbf{q}}) + \delta^{\text{em}}_{\mathbf{k},\nu\mathbf{q}}(N_{\nu\mathbf{q}} + 1 - f^0_{\mathbf{k}+\mathbf{q}})\right)\Delta f_{\mathbf{k}} \\ &- \left(\delta^{\text{abs}}_{\mathbf{k},\nu\mathbf{q}}(N_{\nu\mathbf{q}} + 1 - f^0_{\mathbf{k}}) + \delta^{\text{em}}_{\mathbf{k},\nu\mathbf{q}}(N_{\nu\mathbf{q}} + f^0_{\mathbf{k}})\right)\Delta f_{\mathbf{k}+\mathbf{q}}\Big]\end{aligned} \tag{3.12}$$

where we have multiplied -1 through the entire BTE, and used $\delta^{\text{em}}_{\mathbf{k},\nu\mathbf{q}}$ and $\delta^{\text{abs}}_{\mathbf{k},\nu\mathbf{q}}$ for the delta functions for phonon emission and absorption, respectively, for a given scattering process. We write them explicitly below.

$$\begin{aligned}\delta^{\text{em}}_{\mathbf{k},\nu\mathbf{q}} &= \delta(\epsilon_{\mathbf{k}} - \hbar\omega_{\nu\mathbf{q}} - \epsilon_{\mathbf{k}+\mathbf{q}}) \\ \delta^{\text{abs}}_{\mathbf{k},\nu\mathbf{q}} &= \delta(\epsilon_{\mathbf{k}} + \hbar\omega_{\nu\mathbf{q}} - \epsilon_{\mathbf{k}+\mathbf{q}})\end{aligned} \tag{3.13}$$

Finally, when solving for mobility, the deviational occupation is often rewritten in the form given below that simplifies the whole BTE:

$$\Delta f_{\mathbf{k}} = f^0_{\mathbf{k}}(1 - f^0_{\mathbf{k}})\frac{e\mathbf{E}}{k_B T} \cdot \mathbf{F}_{\mathbf{k}} \tag{3.14}$$

The physical meaning of this expression is that the deviational occupation scales linearly with electric field, and the solution is captured by a new dummy variable $\mathbf{F}_{\mathbf{k}}$. If we substitute this expression into the low-field BTE of Eq. 3.12, we can see that terms of the form $f^0_{\mathbf{k}}(1 - f^0_{\mathbf{k}})\frac{e\mathbf{E}}{k_B T}$ appear on both sides of the BTE and can be divided out due to the linearity of both the collision integral and the dot product.

The resulting BTE is given below:

$$\mathbf{v_k} = \frac{2\pi}{\hbar}\frac{1}{N}\sum_{\nu\mathbf{q}}|g_{\mathbf{k},\nu\mathbf{q}}|^2 \Bigg[\left(\delta^{\text{abs}}_{\mathbf{k},\nu\mathbf{q}}(N_{\mathbf{q}} + f^0_{\mathbf{k+q}}) + \delta^{\text{em}}_{\mathbf{k},\nu\mathbf{q}}(N_{\mathbf{q}} + 1 - f^0_{\mathbf{k+q}})\right)\mathbf{F_k} - \frac{f^0_{\mathbf{k+q}}(1 - f^0_{\mathbf{k+q}})}{f^0_{\mathbf{k}}(1 - f^0_{\mathbf{k}})}\left(\delta^{\text{abs}}_{\mathbf{k},\nu\mathbf{q}}(N_q + 1 - f^0_{\mathbf{k}}) + \delta^{\text{em}}_{\mathbf{k},\nu\mathbf{q}}(N_q + f^0_{\mathbf{k}})\right)\mathbf{F_{k+q}}\Bigg] \tag{3.15}$$

A common approximation in the literature is to obtain a solution while disregarding the second term in the sum on the right hand side of the equation above. This is known as the relaxation time approximation (RTA), and the resulting electron occupations for each state are independent of the occupations of all other states, since each $\mathbf{F_k}$ requires no knowledge of the $\mathbf{F_{k+q}}$. However, it is known that the full solution to the BTE beyond the RTA will be substantially different if the scattering is anisotropic [234], and this has been shown to be the case in GaAs [97]. Whether through the RTA, or through the full solution, once the $\mathbf{F_k}$ are obtained, the conductivity can be calculated using the following expression [73]:

$$\sigma_{\alpha\beta} = \frac{2e^2}{V_0 k_B T}\sum_{\mathbf{k}} f^0_{\mathbf{k}}(1 - f^0_{\mathbf{k}})v^{\alpha}_{\mathbf{k}}F^{\beta}_{\mathbf{k}} \tag{3.16}$$

Finally, we can calculate the mobility which normalizes the conductivity by n_{c}, the carrier density:

$$\mu_{\alpha\beta} = \frac{\sigma_{\alpha\beta}}{en_{\text{c}}} \tag{3.17}$$

The purpose of this derivation is to show that the BTE formalism when solving for low-field mobility does not involve the electric field at all. One can see that in Eq. 3.15, the electric field does not appear in the expression since the solution being sought is the linear response. The nonlinearity of the collision integral is ignored due to nearness to equilibrium. This is the framework that we move beyond to solve for charge transport at high fields.

Wannier interpolation of e-ph matrix elements

The e-ph matrix elements $g_{\mathbf{k},\nu\mathbf{q}}$ of Eq. 3.4 are perhaps the most important ingredients for a first principles charge transport calculation. For a scattering

process that takes an electron from state $\psi_{\mathbf{k}}$ to another state $\psi_{\mathbf{k+q}}$ through a phonon at $\mathbf{q}$ of branch ν, the e-ph matrix element is:

$$g_{\mathbf{k},\nu\mathbf{q}} = \langle \psi_{\mathbf{k+q}} | \partial_{\nu\mathbf{q}} V | \psi_{\mathbf{k}} \rangle \tag{3.18}$$

Typically, the electronic states are taken to be the DFT eigenstates, and $\partial_{\nu\mathbf{q}} V$ is the perturbation induced in the self-consistent DFT potential due the phonon indexed by $\nu\mathbf{q}$. The perturbation potential is typically obtained from DFPT from which the phonons are calculated.

However, when calculating transport quantities like mobility, fine grids for the electrons and phonons are required. This is because the phonon energy scale is on the order of tens of meV whereas the electron energy scale is on the order of eV, so dense sampling is required to include the possible scattering channels and thus obtain the converged scattering rates. This means calculating the e-ph matrix elements for up to millions of combinations of electrons and phonons, a computationally demanding task often limited by the cost of DFPT. The development of Wannier interpolation made the fully ab initio calculation possible [235–237].

Wannier functions have a broad range of purposes and physical interpretations [237], but we concern ourselves here only to their application to transport calculations. The reason Wannier functions are able to provide interpolation of the necessary quantities like the e-ph matrix elements on fine grids throughout the entire Brillouin zone is because the e-ph interaction is short ranged in non-polar materials [236]. This fact alone is not enough, but by selecting the Wannier functions that are maximally localized, one obtains an efficient representation of the e-ph interaction that allows interpolation to fine grids.

Achieving maximal localization requires a definition of the real space spread of Wannier functions, which are composed of electron eigenstates, or Bloch functions, that are defined to be spatially delocalized. A definition for a localization functional was established [238] that relied on a gradient in reciprocal space through a finite difference scheme. Coincidentally, this is the same finite difference scheme we use in Sec. 3.2 to calculate the reciprocal space gradient at high electric fields.

Finally, we note that in polar materials, the e-ph interaction is not short range due to the interactions of electrons with polar LO phonons. This long range contribution must be included separately [239, 240].

A more detailed outline of the theory behind the interpolation of the e-ph interaction using Wannier functions requires a not insubstantial amount of derivation which we consider beyond the scope of this thesis given that many accessible electronic structure codes are able to perform such interpolations, not necessarily with Wannier functions. An important review of Wannier functions can be found in Ref. [237] and a review of their use in the context of mobility calculations can be found in Ref. [71]. Our work uses the Perturbo code [241] developed at Caltech by the Bernardi group.

3.2 Effect of high electric fields on the Boltzmann equation

There must be changes to the BTE at high fields since we no longer satisfy the condition that $\Delta f_{\mathbf{k}} \ll f^0_{\mathbf{k}}$. This prevents the use of an analytical expression for the field term, and the collision integral no longer has negligible nonlinear terms.

Electric field term using finite differences

At high fields, the gradient term can no longer be approximated by the gradient on the equilibrium distribution only; $\nabla_{\mathbf{k}} f_{\mathbf{k}} \neq \nabla f^0_{\mathbf{k}}$. This occurs because the reciprocal space gradient on the deviational occupation $\Delta f_{\mathbf{k}}$ is non-negligible.

Instead of treating the field term entirely numerically, we keep the analytical expression for the equilibrium distribution and employ a finite difference formula [242, 243] to obtain the reciprocal space gradient on $\Delta f_{\mathbf{k}}$:

$$\nabla_{\mathbf{k}}[\Delta f_{\mathbf{k}}] = \sum_{\mathbf{b}} w_b \mathbf{b} (\Delta f_{\mathbf{k}+\mathbf{b}} - \Delta f_{\mathbf{k}}) \tag{3.19}$$

Here, $\mathbf{b}$ is a set of vectors connecting a grid point in reciprocal space $\mathbf{k}$ to its neighbors, and w_b is a weight factor that is unique for each set of neighbor vectors of the same magnitude $b = |\mathbf{b}|$. The vectors and weights are chosen so that the gradient is correct to linear order, which, depending on the symmetry of the crystal and the grid points in the Brillouin zone, may require more than one "shell" of neighbor vectors [242]. However, in GaAs this condition can be satisfied with just one shell and we write the simplified constraint for a single shell that gives the correct gradient:

$$w_b \sum_i b_\alpha^i b_\beta^i = \delta_{\alpha\beta} \tag{3.20}$$

where i indexes the vectors of the shell and α and β are Cartesian directions. In GaAs, the shell that satisfies this constraint is simply the set of vectors connecting the point $\mathbf{k}$ to its first nearest neighbors. The meaning of the weights w_b becomes somewhat more intuitive if we consider a one dimensional derivative of some function $f(x)$ which has two nearest neighbor points at $f(x \pm \Delta x)$ where instead of neighbor vectors we simply have $\pm\Delta x$. Then we have that $w_b = 1/(2\Delta x^2)$ and the finite difference scheme of Eq. 3.19 gives the familiar central difference formula:

$$\frac{df}{dx} = \sum_{\pm\Delta x} \frac{\pm\Delta x}{2\Delta x^2}(f_{x\pm\Delta x} - f_x) = \frac{(f_{x+\Delta x} - f_{x-\Delta x})}{2\Delta x} \tag{3.21}$$

As noted previously, the finite difference formula of Eq. 3.19 is the same used to calculate spatial spread when constructing maximally localized Wannier functions.

The finite difference scheme can be expressed as a matrix acting on a vector of the distribution function at each grid point in the Brillouin zone with entries in each row of the finite difference matrix at locations corresponding to the nearest neighbors of the grid point for the row, and with a matrix vector product that satisfies Eq. 3.19. If we further incorporate the dot product with the electric field that appears in the field term of the BTE, then we can write the matrix as:

$$\sum_\alpha \sum_{\mathbf{k}'} \frac{eE_\alpha}{\hbar} D^\alpha_{\mathbf{k},\mathbf{k}'} \Delta f_{\mathbf{k}'} = \sum_\alpha \sum_{\mathbf{b}} E_\alpha b_\alpha w_b (\Delta f_{\mathbf{k}+\mathbf{b}} - \Delta f_{\mathbf{k}}) \tag{3.22}$$

where $D^\alpha_{\mathbf{k},\mathbf{k}'}$ is the finite difference matrix for Cartesian direction α, and has entries of 0 except when $\mathbf{k}' = \mathbf{k} + \mathbf{b}$ or $\mathbf{k}' = \mathbf{k}$. The dot product is now a sum over matrix vector products for each of the Cartesian directions. This may seem like a more tedious way to write the gradient term, but we do so to clearly formulate the BTE as a set of linear equations, which we will solve using numerical techniques for large linear systems. We can now write the BTE for high fields as follows:

$$-\frac{e\mathbf{E}}{k_B T}\cdot\mathbf{v}_{\mathbf{k}} f^0_{\mathbf{k}}(1-f^0_{\mathbf{k}}) + \sum_{\alpha}\sum_{\mathbf{k}'}\frac{eE_\alpha}{\hbar}D^{\alpha}_{\mathbf{k},\mathbf{k}'}\Delta f_{\mathbf{k}'} = \mathcal{I}[f_{\mathbf{k}}] \tag{3.23}$$

On the left hand side, we have both the analytical expression for the field term on the equilibrium occupation and the numerical expression for the field term on the deviational occupation. The task is to now address the form of the collision integral $\mathcal{I}[f_{\mathbf{k}}]$ for high electric fields. We have said previously that non-linearities are non-negligible at high fields, but we will show that certain approximations can be made to obtain a collision integral for high fields that remains linear on the deviational occupations.

Collision integral at high electric fields

Previously, we neglected higher order terms of the form $\Delta f_{\mathbf{k}}\Delta f_{\mathbf{k}+\mathbf{q}}$ in the fully non-linear weights of Eqs. 3.8 and 3.9, since $\Delta f_{\mathbf{k}} \ll f^0_{\mathbf{k}}$, a condition we know is violated at high electric fields. However, for non-degenerate electrons, the distribution function values are always much less than the phonon occupations ($f_{\mathbf{k}} \ll N_q$) even at high fields. Therefore, if we look at the fully nonlinear expressions in Eqs. 3.8 and 3.9, we see that there are electron occupation terms that are added or subtracted from phonon occupations that will have negligible effect. Thus, we remove these electron occupation terms and the resulting weights are:

$$\begin{aligned} H^{\text{em}} &= \Delta f_{\mathbf{k}}(N_{\nu\mathbf{q}}+1) - \Delta f_{\mathbf{k}+\mathbf{q}}(N_{\nu\mathbf{q}}) \\ H^{\text{abs}} &= \Delta f_{\mathbf{k}}(N_{\nu\mathbf{q}}) - \Delta f_{\mathbf{k}+\mathbf{q}}(N_{\nu\mathbf{q}}+1) \end{aligned} \tag{3.24}$$

The physical meaning of neglecting the electron occupations in the weights is that, for non-degenerate carrier concentrations, the e-ph scattering rate does not depend on the electron occupation unless it multiplies the phonon occupation. This is a consequence of our definition of the electron distribution function expanded about equilibrium, $f_{\mathbf{k}} = f^0_{\mathbf{k}} + \Delta f_{\mathbf{k}}$, which led to the cancellation of many terms as outlined in the derivation leading to Eq 3.8. The approximation is particularly well-satisfied for GaAs owing to its relatively low Debye temperature of 360 K [244], yielding phonon occupations $N_q \sim 1$ even at optical phonon energies.

We numerically verify the validity of this approximation by solving for the deviational occupation using the weights of Eq. 3.24 which allows the BTE to

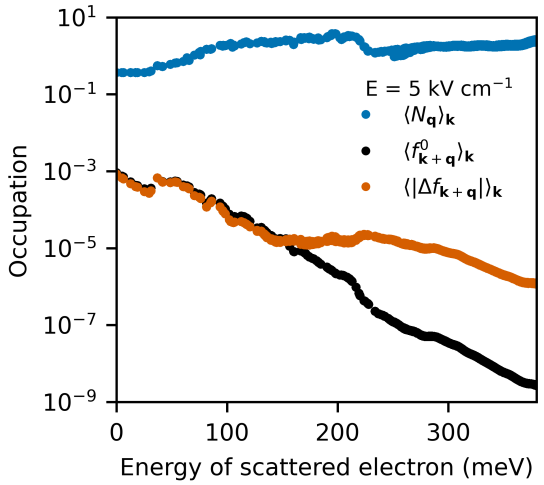

Figure 3.1: Average occupation of the phonons and electrons involved in scattering a state at a given energy, using the solution to the BTE at a field of 5 kV cm^{-1}. The averages are weighted by the delta functions as given in Eq. 3.25. It can be seen that the electron occupations are at least two orders of magnitude smaller than the phonon occupations, justifying the solution of the BTE without reference to the electron occupations in the collision integral.

be solved as a linear system. We plot the equilibrium and deviational electron occupation as well as the phonon occupation at the highest electric field of interest in Fig. 3.1. Note that since the weights in the occupation factor depend on the final state that can be coupled, we are not simply plotting the Fermi Dirac distribution versus energy. There is a phase space factor that depends on the allowed e-ph scattering processes, and we account for this by plotting the average value of the phonon and electron occupations weighted by the delta functions. The averages are given by the equations below:

$$\begin{aligned} \langle N_{\mathbf{q}} \rangle_{\mathbf{k}} &= \sum_{\mathbf{q}'} \delta^{\text{em}}_{\mathbf{k},\nu\mathbf{q}} (N_{\mathbf{q}'} + 1) + \delta^{\text{abs}}_{\mathbf{k},\nu\mathbf{q}} N_{\mathbf{q}'} \\ \langle f^0_{\mathbf{k}+\mathbf{q}} \rangle_{\mathbf{k}} &= \sum_{\mathbf{q}'} (\delta^{\text{em}}_{\mathbf{k},\nu\mathbf{q}} + \delta^{\text{abs}}_{\mathbf{k},\nu\mathbf{q}}) f^0_{\mathbf{k}+\mathbf{q}'} \\ \langle |\Delta f_{\mathbf{k}+\mathbf{q}}| \rangle_{\mathbf{k}} &= \sum_{\mathbf{q}'} (\delta^{\text{em}}_{\mathbf{k},\nu\mathbf{q}} + \delta^{\text{abs}}_{\mathbf{k},\nu\mathbf{q}}) |\Delta f_{\mathbf{k}+\mathbf{q}'}| \end{aligned} \tag{3.25}$$

We see in Fig. 3.1 that the electron occupations are indeed much smaller than the phonon occupations, justifying our solution of the BTE without electron occupations in the collision integral. When comparing the high-field weights

of Eq. 3.24 to the low-field weights of Eq. 3.10, we see that they are identical except for the presence of electron occupations in Eq. 3.10. It may seem like the low-field weights are "less approximate" since they use information about the electron occupations, but what we are saying with our high-field collision integral is that even if we included the non-linear terms, we would obtain the same distribution as if we had not included any electron occupations in the weights to begin with. Thus, to be consistent with the approximation, we do not include any electron occupations.

We have established that at high fields, the collision integral is still linear on the deviational occupations, so we now formally write the high-field BTE as a set of linear equations, where we replace $\mathcal{I}[f_{\mathbf{k}}]$ with a matrix:

$$-\frac{e\mathbf{E}}{k_B T}\cdot\mathbf{v}_{\mathbf{k}} f^0_{\mathbf{k}}(1-f^0_{\mathbf{k}}) + \sum_{\alpha}\sum_{\mathbf{k}'}\frac{eE_\alpha}{\hbar}D^{\alpha}_{\mathbf{k},\mathbf{k}'}\Delta f_{\mathbf{k}'} = \sum_{\mathbf{k}'}\Theta_{\mathbf{k},\mathbf{k}'}\Delta f_{\mathbf{k}'} \tag{3.26}$$

where we denote $\Theta_{\mathbf{k},\mathbf{k}'}$ as the scattering matrix, which corresponds to the linear, high-field collision integral. We explicitly give its expression below:

$$\begin{aligned}\sum_{\mathbf{k}'}\Theta_{\mathbf{k},\mathbf{k}'}\Delta f_{\mathbf{k}'} = -\frac{2\pi}{\hbar}\frac{1}{N}\sum_{\nu\mathbf{q}}|g_{\mathbf{k},\nu\mathbf{q}}|^2\Big[&\left(\delta^{\text{abs}}_{\mathbf{k},\nu\mathbf{q}}N_{\nu\mathbf{q}} + \delta^{\text{em}}_{\mathbf{k},\nu\mathbf{q}}(N_{\nu\mathbf{q}}+1)\right)\Delta f_{\mathbf{k}} \\ &+\left(\delta^{\text{abs}}_{\mathbf{k},\nu\mathbf{q}}(N_{\nu\mathbf{q}}+1) + \delta^{\text{em}}_{\mathbf{k},\nu\mathbf{q}}N_{\nu\mathbf{q}}\right)\Delta f_{\mathbf{k}+\mathbf{q}}\Big]\end{aligned} \tag{3.27}$$

Here, $\mathbf{k}'$ ranges over all possible electronic states, and the diagonal ($\mathbf{k}' = \mathbf{k}$) entries of the scattering matrix correspond to the first term on the right hand side of the equation which is a sum over all possible scattering channels, and thus are equal to the scattering rates times -1. The off diagonal entries of the matrix are only nonzero when $\mathbf{k}' = \mathbf{k}+\mathbf{q}$, and contain exactly the amount of coupling between states at $\mathbf{k}$ and $\mathbf{k}+\mathbf{q}$, mediated by all possible phonon branches ν at the wave vector $\mathbf{q}$.

We rearrange terms so that we have a linear system of the form $\mathbf{A}x = b$:

$$\sum_{\mathbf{k}'}\left[\sum_{\alpha}\frac{eE_\alpha}{\hbar}D^{\alpha}_{\mathbf{k},\mathbf{k}'} - \Theta_{\mathbf{k},\mathbf{k}'}\right]\Delta f_{\mathbf{k}'} = \frac{e\mathbf{E}}{k_B T}\cdot\mathbf{v}_{\mathbf{k}} f^0_{\mathbf{k}}(1-f^0_{\mathbf{k}}) \tag{3.28}$$

We have now transformed the BTE from a set of coupled integro-differential equations into a linear system of differential equations where the inhomogenous term is the equilibrium field term on the right hand side.

We now define a relaxation operator which captures the effect of both the electric field and the scattering matrix:

$$\sum_{\mathbf{k}'} \Lambda_{\mathbf{k},\mathbf{k}'} \Delta f_{\mathbf{k}'} \equiv \sum_{\mathbf{k}'} \left[\sum_{\alpha} \frac{eE_{\alpha}}{\hbar} D^{\alpha}_{\mathbf{k},\mathbf{k}'} - \Theta_{\mathbf{k},\mathbf{k}'} \right] \Delta f_{\mathbf{k}'} \tag{3.29}$$

The solution to the BTE can now be expressed symbolically using the inverse of this relaxation operator.

$$\Delta f_{\mathbf{k}} = \sum_{\mathbf{k}'} \Lambda^{-1}_{\mathbf{k},\mathbf{k}'} \left(\frac{e\mathbf{E}}{k_B T} \cdot \mathbf{v}_{\mathbf{k}'} f^0_{\mathbf{k}'} (1 - f^0_{\mathbf{k}'}) \right) \tag{3.30}$$

The field dependent conductivity can now be written:

$$\sigma_{\alpha\beta}(\mathbf{E}) = \frac{2e^2}{k_B T V_0} \sum_{\mathbf{k}} v_{\mathbf{k},\alpha} \sum_{\mathbf{k}'} \Lambda^{-1}_{\mathbf{k},\mathbf{k}'} (v_{\mathbf{k}',\beta} f^0_{\mathbf{k}'} (1 - f^0_{\mathbf{k}'})) \tag{3.31}$$

which reduces to the low field conductivity of Eq. 3.16 when the electric field is small, and the relaxation operator contains no field term on the deviational occupation, reducing to just the scattering matrix.

Another commonly reported high-field observable is the drift velocity which describes the mean velocity of of electrons at steady state for a given electric field:

$$\mathbf{V} = \frac{1}{n} \sum_{\mathbf{k}} \mathbf{v}_{\mathbf{k}} f^s_{\mathbf{k}} \tag{3.32}$$

Here $n = \sum_{\mathbf{k}} f_{\mathbf{k}}$ is the total particle number. There are many studies reporting the drift velocity versus field curve in GaAs [191–193] since GaAs is a material that exhibits the Gunn effect, which manifests as a region of negative slope in the drift velocity curve.

AC conductivity and differential conductivity

Another important transport quantity at high fields is the AC small-signal conductivity $\sigma^{\omega}_{\alpha\beta}$, which describes the linear response of the system about

steady-state [99]. The AC conductivity at zero frequency is known as the differential conductivity. The differential conductivity is identical to the DC conductivity at low fields, but deviates from the DC value at high fields where there is a non-equilibrium steady state.

With the steady distribution $f^s_{\mathbf{k}}$ being set by a DC field $\mathbf{E}$ as described above, an AC field perturbation given by $\delta\mathbf{E}e^{i\omega t}$, induces a fluctuation of the electron distribution $\delta f_{\mathbf{k}}(t) = \delta f_{\mathbf{k}}(\omega)e^{i\omega t}$. This fluctuation is governed by the Fourier transformed Boltzmann equation:

$$\sum_{\mathbf{k}'}(i\omega\mathbb{I} + \Lambda)_{\mathbf{k},\mathbf{k}'}\ \delta f_{\mathbf{k}'} = -\frac{e\delta\mathbf{E}}{\hbar}\cdot\nabla_{\mathbf{k}} f^s_{\mathbf{k}} \tag{3.33}$$

Here, $\mathbb{I}$ is the identity matrix and the $i\omega$ term comes from the Fourier transform of the time derivative in Eq. 3.2. The fluctuation in the distribution function induces a current fluctuation about the DC value, given as:

$$\delta j_\alpha = \frac{2e}{V_0}\sum_{\mathbf{k}} v_{\mathbf{k},\alpha}\ \delta f_{\mathbf{k}} \tag{3.34}$$

Again the factor of 2 comes from the assumption of spin degeneracy. The small-signal AC conductivity is defined as the linear response coefficient of the current density to the field perturbation, $\sigma^{\mathrm{AC}}_{\alpha\beta}(\omega,\mathbf{E}) \equiv \delta j_\alpha/\delta E_\beta$. This is why the zero frequency AC conductivity is known as the differential conductivity. An explicit expression for AC conductivity can be obtained by combining the above expressions:

$$\sigma^{\mathrm{AC}}_{\alpha\beta}(\omega,\mathbf{E}) = \frac{2e^2}{V_0\hbar}\sum_{\mathbf{k}} v_{\mathbf{k},\alpha}\sum_{\mathbf{k}'}(i\omega\,\mathbb{I} + \Lambda)^{-1}_{\mathbf{k},\mathbf{k}'}\left[-\frac{\partial f^s_{\mathbf{k}'}}{\partial k_\beta}\right] \tag{3.35}$$

At equilibrium the steady distribution reduces to the equilibrium distribution $f^s_{\mathbf{k}} = f^0_{\mathbf{k}}$, the relaxation operator reduces to the scattering matrix, $\Lambda_{\mathbf{k},\mathbf{k}'} = \Theta_{\mathbf{k},\mathbf{k}'}$. By examining Eq. 3.16 and Eq. 3.35, we see that at equilibrium the zero-frequency AC conductivity, or differential conductivity, is equal to the low-field conductivity as expected.

The differential mobility will become negative in the region of negative slope of the drift velocity (Eq. 3.32).

3.3 Ab initio computation of electronic noise

As discussed in Ch. 1, the behavior of fluctuations at high electric fields probes the e-ph interactions in a qualitatively different way that cannot be described by mean transport quantities like drift velocity alone [99, 105]. Since the fluctuations themselves obey the BTE, the dissipation of fluctuations at low fields is already captured by the linear response of the system about the equilibrium state, represented in the low-field conductivity we calculate using the BTE. At high fields, the fluctuations are not dissipating back to equilibrium but rather to a non-equilibrium steady state, and the associated non-equilibrium noise is termed "hot electron noise."

Let us now describe the equations used to calculate hot electron noise. Suppose that the steady state distribution $f^s_{\mathbf{k}}$ is known. Just as in equilibrium, fluctuations in the instantaneous occupation of the quantum states occur. Microscopically, these fluctuations arise because of the stochastic nature of the scattering described by $\Theta_{m\mathbf{k}m'\mathbf{k}'}$. At steady state, detailed balance requires that the mean flux of particles into every quantum state is zero. However, the flux of particles into or out of a quantum state is a Poissonian process and is characterized by a variance. Therefore, the instantaneous net flux into a quantum state is in general non-zero due to instantaneous imbalance between the incoming and outgoing fluxes [245]. Consequently, the occupation of quantum states fluctuates under both equilibrium and non-equilibrium conditions. In the macroscopic limit at which fluctuations are observed in the laboratory, these distribution function fluctuations appear as instantaneous current fluctuations, or equivalently, as electronic noise. A non-random characteristic of these fluctuations is the power spectral density (PSD) of current density fluctuations, which, by the Wiener-Khintchine Theorem, is related to the single-sided Fourier transform of the autocorrelation of the current density fluctuations [99, 246]:

$$S_{j_\alpha j_\beta}(\omega) \equiv (\delta j_\alpha \delta j_\beta)_\omega = 2\int_{-\infty}^{\infty} \overline{\delta j_\alpha(t)\delta j_\beta} e^{-i\omega t} dt \tag{3.36}$$

where the overbar indicates ensemble average over the states in the system, and the factor of 2 comes from the even and real nature of the autocorrelation which gives the single-sided Fourier transform as twice the amplitude of the double-sided spectrum.

We seek to link the macroscopic current density fluctuations to microscopic distribution function fluctuations. Following Ref. [245], we now consider random fluctuations about the non-equilibrium steady state, $\delta f_{\mathbf{k}}(t) = f_{\mathbf{k}}(t) - f^s_{\mathbf{k}}$. In contrast to the fluctuations associated with the small signal conductivity, these fluctuations are induced by the stochastic nature of scattering rather than an external perturbation. The corresponding current density fluctuations can be expressed in terms of the fluctuation in the distribution function as in Eq. 3.34.

It follows that the ensemble average of the correlation function of instantaneous current fluctuations along axes α and β, $\overline{\delta j_\alpha(t)\delta j_\beta}$, can be expressed in terms of the correlation function of the occupation fluctuations, $\overline{\delta f_{\mathbf{k}}(t)\delta f_{\mathbf{k}_1}}$:

$$\overline{\delta j_\alpha(t)\delta j_\beta} = \left(\frac{2e}{V_0}\right)^2 \sum_{\mathbf{k}} \sum_{\mathbf{k}_1} v_{\mathbf{k},\alpha}\, v_{\mathbf{k}_1,\beta}\, \overline{\delta f_{\mathbf{k}}(t)\delta f_{\mathbf{k}_1}} \tag{3.37}$$

Equation 3.37 shows that computing the spectral density of current density fluctuations requires calculating the correlation of occupation fluctuations for states at $\mathbf{k}$ and $\mathbf{k}_1$: $\overline{\delta f_{\mathbf{k}}(t)\delta f_{\mathbf{k}_1}}$. This function is known as the time-displaced, two particle correlation function [245]. Through a quantum statistical mechanical treatment, Gantsevich and coauthors have demonstrated that the time-displaced, two particle correlation function obeys the same Boltzmann equation as the fluctuation itself [108]:

$$\frac{\partial}{\partial t}\overline{\delta f_{\mathbf{k}}(t)\delta f_{\mathbf{k}_1}} + \sum_{\mathbf{k}'} \Lambda_{\mathbf{k},\mathbf{k}'}\, \overline{\delta f_{\mathbf{k}'}(t)\delta f_{\mathbf{k}_1}} = 0 \tag{3.38}$$

where $\Lambda_{\mathbf{k},\mathbf{k}'}$ is the same relaxation operator of Eq. 3.29 which now acts on the correlation function. The result of Eqn. 3.38 can also be justified less mathematically rigorously but with more physical intuition from Onsager's regression hypothesis (in particular, see Sec. 1 of Ref. [245]).

Solving Eqn. 3.38 requires specifying an initial condition, $\overline{\delta f_{\mathbf{k}}(t)\delta f_{\mathbf{k}_1}}|_{t=0}$, which is known as the one-time, two-particle correlation function. For a non-degenerate system with a fixed number of particles N, Fowler [247] and Lax [209] derived the required condition as:

$$\overline{\delta f_{\mathbf{k}}(t)\delta f_{\mathbf{k}_1}}|_{t=0} = f^s_{\mathbf{k}}\delta_{\mathbf{k}\mathbf{k}_1} - \frac{f_{\mathbf{k}} f_{\mathbf{k}_1}}{N} \tag{3.39}$$

where the second term on the right-hand side indicates that a correlation exists between occupations due to the fixed particle number.

Now, substituting the current fluctuation expression of Eq. 3.37 into the Wiener-Khintchine relation of Eq. 3.36 allows us to express the current PSD explicitly in terms of the correlation function solution to the Boltzmann equation of Eq. 3.38:

$$(\delta j_\alpha \delta j_\beta)_\omega = \left(\frac{2e}{V_0}\right)^2 \sum_{\mathbf{k}} \sum_{\mathbf{k}_1} v_{\mathbf{k},\alpha}\, v_{\mathbf{k}_1,\beta}\, (\delta f_{\mathbf{k}} \delta f_{\mathbf{k}_1})_\omega \tag{3.40}$$

Here, $(\delta f_{\mathbf{k}} \delta f_{\mathbf{k}_1})_\omega$ is the Fourier transform of the correlation function solution to the Boltzmann equation:

$$(\delta f_{\mathbf{k}} \delta f_{\mathbf{k}_1})_\omega = \int_{-\infty}^{\infty} \overline{\delta f_{\mathbf{k}}(t) \delta f_{\mathbf{k}_1}}\, \mathrm{e}^{-i\omega t}\, dt \tag{3.41}$$

This also has the meaning of the spectral density of occupation fluctuations by the Wiener-Khintchine theorem. Since we are interested in the power spectral density at a given frequency, as opposed to the full time dependence of the time-displaced two particle correlation function, we can instead solve the Fourier transformed version of Eq. 3.38. The result, which exploits the stationary property of the autocorrelation function, allows us to express the Fourier transformed correlation function as [245]:

$$(\delta f_{\mathbf{k}} \delta f_{\mathbf{k}_1})_\omega = 2\Re\left[\sum_{\mathbf{k}'} (i\omega \mathbb{I} + \Lambda)^{-1}_{\mathbf{k}\mathbf{k}'}\, \overline{\delta f_{\mathbf{k}'}(t) \delta f_{\mathbf{k}_1}}|_{t=0} \right] \tag{3.42}$$

Where the initial condition of Eq. 3.39 becomes the inhomogeneous term for the Boltzmann equation of Eq. 3.38. Combining Eqs. 3.39, 3.40, and 3.42, we obtain the following expression:

$$\begin{aligned} S_{j_\alpha j_\beta}(\omega) &= 2\left(\frac{2e}{V_0}\right)^2 \Re\left[\sum_{\mathbf{k}} v_{\mathbf{k},\alpha} \sum_{\mathbf{k}'} (i\omega \mathbb{I} + \Lambda)^{-1}_{\mathbf{k}\mathbf{k}'} \sum_{\mathbf{k}_1} v_{\mathbf{k}_1,\beta} \left(f^s_{\mathbf{k}'} \delta_{\mathbf{k}'\mathbf{k}_1} - \frac{f^s_{\mathbf{k}'} f^s_{\mathbf{k}_1}}{N} \right) \right] \\ &= 2\left(\frac{2e}{V_0}\right)^2 \Re\left[\sum_{\mathbf{k}} v_{\mathbf{k},\alpha} \sum_{\mathbf{k}'} (i\omega \mathbb{I} + \Lambda)^{-1}_{\mathbf{k}\mathbf{k}'} \left(f^s_{\mathbf{k}'} (v_{\mathbf{k}',\beta} - V_\beta) \right) \right] \end{aligned} \tag{3.43}$$

Here, V_β is the drift velocity (Eq. 3.32) along the β axis. As a check of the above derivation, consider an equilibrium system for which $\mathbf{E} = 0$ and $V_\beta = 0$. The equation is simplified with $f^s_{\mathbf{k}} = f^0_{\mathbf{k}}$ and $\Lambda_{\mathbf{k}\mathbf{k}'} = \Theta_{\mathbf{k}\mathbf{k}'}$. Then, we have:

$$S_{j_\alpha j_\beta}(\omega, \mathbf{E}=0) = 2\left(\frac{2e}{V_0}\right)^2 \Re\left[\sum_{\mathbf{k}} v_{\mathbf{k},\alpha} \sum_{\mathbf{k}'} (i\omega\mathbb{I} + \Theta)^{-1}_{\mathbf{k}\mathbf{k}'} (f^0_{\mathbf{k}'} v_{\mathbf{k}',\beta})\right] \tag{3.44}$$

With the same simplifications, the equilibrium AC conductivity from Eq. 3.35 is:

$$\sigma^{\mathrm{AC}}_{\alpha\beta}(\omega, \mathbf{E}=0) = \frac{2e^2}{\hbar V_0} \sum_{\mathbf{k}} v_{\mathbf{k},\alpha} (i\omega\mathbb{I} + \Theta)^{-1}_{\mathbf{k}\mathbf{k}'} \left[-\frac{\partial f^0_{\mathbf{k}'}}{\partial k_\beta}\right] \tag{3.45}$$

Combining the above expressions, we obtain the familiar Nyquist relationship [104]:

$$S_{j_\alpha j_\beta}(\omega, \mathbf{E}=0) = \frac{4k_B T_0}{V_0} \Re\left[\sigma^{\mathrm{AC}}_{\alpha\beta}(\omega, \mathbf{E}=0)\right] \tag{3.46}$$

The "effective distribution function"

An alternative but mathematically equivalent perspective can be gained by re-arranging the order of certain summations which gives some physical intuition for the expressions derived above and more clearly indicates the quantities that are calculated in practice.

First, note that there are 3 sums in the first line of Eq. 3.43, where the first and last sums over $\mathbf{k}$ and $\mathbf{k}_1$ come from expressing the current fluctuations as occupation fluctuations in 3.40. The middle sum over $\mathbf{k}'$ comes from the relaxation operator acting on the correlation function. The second line of Eq. 3.43 shows that multiplying the initial condition of Eq. 3.39 by the group velocity and summing over $\mathbf{k}_1$ gives a simplified expression. So we can consider a situation where we seek the Fourier transformed solution indicated in Eq. 3.42, but multiplied by the group velocity and summed over $\mathbf{k}_1$. This quantity would correspond to a modified and Fourier transformed version of Eq. 3.38:

$$\sum_{\mathbf{k}_1} v_{\mathbf{k}_1,\beta} \sum_{\mathbf{k}'} (i\omega\mathbb{I} + \Lambda)_{\mathbf{k},\mathbf{k}'} (\delta f_{\mathbf{k}} \delta f_{\mathbf{k}_1})_\omega = \sum_{\mathbf{k}_1} v_{\mathbf{k}_1,\beta} \left(f^s_{\mathbf{k}} \delta_{\mathbf{k}\mathbf{k}_1} - \frac{f^s_{\mathbf{k}} f^s_{\mathbf{k}_1}}{N}\right) \tag{3.47}$$

Let us now define a new variable which has been denoted the "effective distribution function" [233]:

$$g^\omega_{\mathbf{k},\beta} = \sum_{\mathbf{k}_1} v_{\mathbf{k}_1,\beta} (\delta f_{\mathbf{k}} \delta f_{\mathbf{k}_1})_\omega \tag{3.48}$$

With this definition, and with the same simplification of the initial condition as given in the second line of Eq. 3.43, we obtain a Boltzmann equation for the effective distribution function:

$$\sum_{\mathbf{k}'} (i\omega\mathbb{I} + \Lambda)_{\mathbf{k},\mathbf{k}'}\, g^{\omega}_{\mathbf{k}',\beta} = f^{s}_{\mathbf{k}}(v_{\mathbf{k},\beta} - V_{\beta}) \tag{3.49}$$

In practice, Eq. 3.49 is the equation that is actually solved, since the effective distribution function also offers a more simple expression for the current PSD:

$$S_{j_\alpha j_\beta}(\omega) = 2\left(\frac{2e}{\mathcal{V}_0}\right)^2 \Re\left[\sum_{\mathbf{k}} v_{\mathbf{k},\alpha}\; g^{\omega}_{\mathbf{k},\beta}\right] \tag{3.50}$$

Thus, calculating the spectral density of curent fluctuations requires solving the inhomogeneous Boltzmann equation twice. First, the steady state distribution function must be obtained using Eq. 3.28. Then, the Boltzmann equation is solved again with inhomogeneous term $f^{s}_{\mathbf{k}}(v_{\mathbf{k},\beta} - V_{\beta})$ with $f^{s}_{\mathbf{k}} \equiv f^{0}_{\mathbf{k}} + \Delta f_{\mathbf{k}}$. The Brillouin zone integration of Eq. 3.50 is then performed to calculate the power spectral density.

Equations 3.49 and 3.50 also give some physical intuition for what can produce a large current PSD. The right hand side of Eq. 3.49 tells us that the current PSD is larger for steady-state distributions with occupation in states for which there is a larger difference between the group velocity and the drift velocity, roughly corresponding to distributions with larger variance. This accords with the intuition that noise power is larger when you have a wider distribution of velocities, but that the magnitude of the velocities cannot be too small, otherwise the noise power is reduced. This is the meaning of the velocity term in the sum in Eq. 3.50.

3.4 Numerical methods

We now describe the numerical methods and parameters used to calculate of the equations described above for electronic noise and high-field transport in GaAs. The observables of interest are the drift velocity and current PSD versus electric field. These require solution to the Boltzmann equation whose inputs are the electronic structure and e-ph matrix elements, which are computed for GaAs from first principles. These quantities are first computed on a coarse grid using Density Functional Theory (DFT) and Density Functional Pertur-

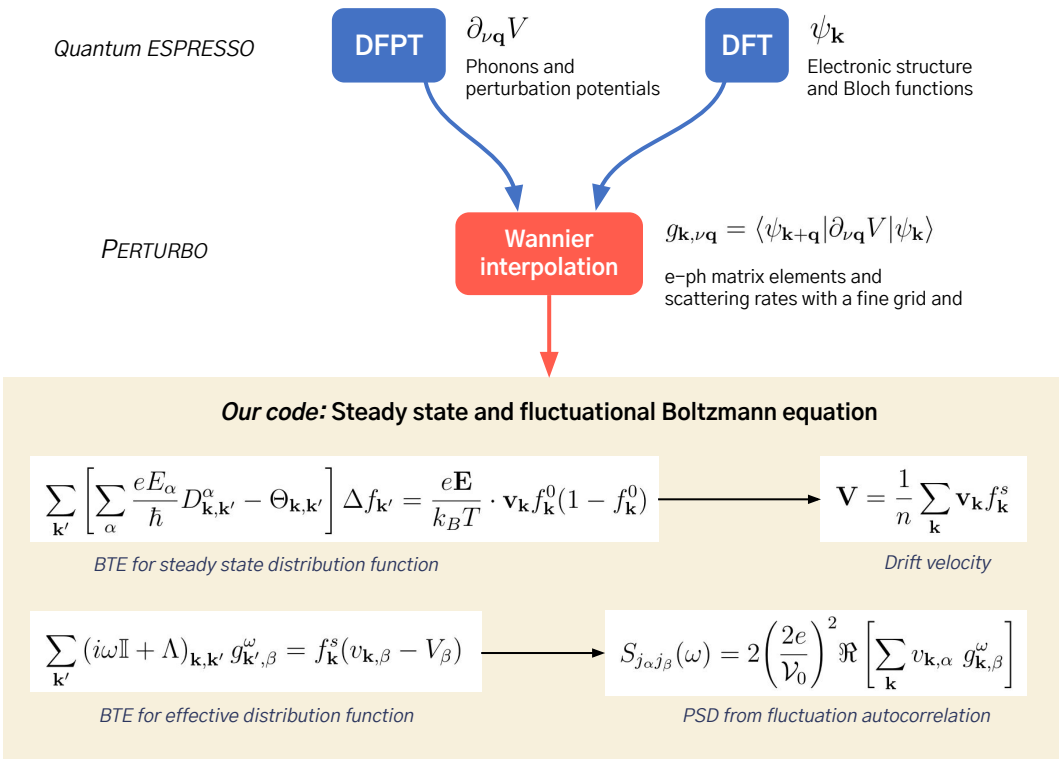

Figure 3.2: The computational workflow for obtaining high-field transport and electronic noise from first principles. The phonon and electron states are obtained from QUANTUM ESPRESSO through DFT and DFPT. The electron band energies, phonon energies, and e-ph matrix elements are then interpolated to a fine grid using PERTURBO. The steady state BTE is then constructed and solved as a linear system as given in Eq. 3.28, from which the drift velocity is obtained. Next, the effective distribution function is calculated with the steady state distribution as an input according to Eq. 3.49 which allows the current PSD to be calculated.

bation Theory (DFPT). They are then obtained on a fine grid using Wannier interpolation. Using the matrix elements and band structure on these fine grids, we solve the respective Boltzmann equations to obtain the steady state distribution for drift velocity, and the effective distribution function for the current PSD. This process is outlined schematically in Fig. 3.2.

Numerical parameters

For the DFT and DFPT calculations, we use QUANTUM ESPRESSO (QE) [248, 249]. The coarse grid for the electronic structure and electron-phonon matrix elements is $8 \times 8 \times 8$. The electronic structure calculations using QE

employ the same simulation parameters as in Ref. [77] where the plane wave cutoff is 72 Ryd and the lattice parameter is 5.556 Å.

The Wannier interpolation to finer grids is performed using PERTURBO [241]. PERTURBO includes corrections for polar materials that are necessary in GaAs [239]. Our calculations were reported in two papers. In the first paper [250], we reported results up to an intermediate electric field of 800 V $cm^{-1}$and used fine grid of $200 \times 200 \times 200$ with a 10 meV broadening parameter for the delta function in the electron-phonon scattering rates [77]. We found that with this grid density, the PSD at the highest field calculated differed by less than 1% from the value obtained on a grid with twice the number of grid points. In the second paper [251], we reported calculations up to a large electric field of 5000 V $cm^{-1}$and used a fine grid of $250 \times 250 \times 250$ with a 5 meV broadening parameter. The transition rates of Eq. 3.27 were calculated at 300 K in both papers, and the phonons are considered to be in equilibrium. In both papers, we set the Fermi level to obtain a carrier concentration of 10^{15} cm^{-3} corresponding to a non-degenerate electron gas.

In PERTURBO, an energy window is specified to limit the points sampled in the Brillouin zone to only those in the relevant energy range. As the electric field increases, electrons are driven to higher energies compared to the energies relevant to thermal equilibrium at room temperature, so this energy window must be larger compared to that used for low-field mobility calculations. In the first paper, the energy window is set to 325 meV above the conduction band minimum (CBM), and in the second paper the energy window is 375 meV above the CBM. Increasing the energy window significantly increases the number of points in part due to the inclusion of the L valley. The primary limitation on computational tractability is the number of k-points sampled since we explicitly construct the matrices that constitute the BTEs of interest, for reasons discussed in the following section. The computational cost grows quickly as the energy window increases since the size of the matrices grows quadratically with the number of k-points. For an energy window of 375 meV and a grid density of $250 \times 250 \times 250$, we have around 61,000 k-points.

Solving the BTE as a linear system

Our code explicitly constructs the relaxation operator of Eq. 3.29 as a matrix by first calculating the scattering matrix given by 3.27 and then adding

the effect of the finite difference matrix (Eq. 3.22). Next, we calculate the inhomogeneous term of Eq. 3.28 and solve for the steady state distribution function. We use this steady state distribution function to calculate the inhomogeneous term of Eq. 3.49 and obtain the effective distribution function which is summed to obtain the current PSD. We note that the typical approach for solving the BTE when calculating low-field mobility as in Eq. 3.15 involves an iterative scheme which begins from the RTA solution and iterates to self consistency [73]. This reduces the memory cost since no matrix is constructed, however we found that this iterative method was numerically unstable for the high-field case. Instead, we construct the linear system and solve it directly using the Generalized Minimal Residual (GMRES) algorithm which is suitable for large matrices. In the first paper, we use the GMRES implementation from the Scientific Python library [252], and in the second paper we use a Fortran implementation of GMRES given by Ref. [253].

Other e-ph interactions

Recent studies have report the effect of the quadrupole electron-phonon interaction on charge transport [91, 254]. The quadrupole interaction is the leading order polar interaction in non-polar materials since there are no dipole interactions like with LO phonons. In polar materials like GaAs, the quadrupole interaction is higher order due to the presence of LO phonons. The work of Ref. [91] predicted a significant correction to the mobility in GaAs limited by acoustic mode scattering, but our calculations were performed at 300 K where the scattering is dominated by polar optical phonons so we neglected quadrupole interactions.

Another higher-order e-ph interaction is due to electrons scattered by two consecutive phonons, which was reported to be necessary to achieve quantitative agreement of mobility in GaAs [98]. We discuss this process in the following section.

3.5 Two-phonon (2ph) scattering

The computational framework for the first-principles calculation of 2ph scattering, where electrons are scattered by two consecutive one-phonon events, was recently developed and reported to be non-negligible for low-field mobility in GaAs [98]. As we will show, the level of theory with first order e-ph scattering where electrons are scattered by one phonon (1ph) is insufficient for

high-field transport and hot electron noise. Therefore, we included scattering from 2ph processes with approximations to ensure computational tractability for the high-field case.

The 2ph scattering rate, as derived in Ref. [98], is given by:

$$\Gamma_{n\mathbf{k}}^{(\mathrm{2ph})} = \frac{2\pi}{\hbar}\frac{1}{N^2}\sum_{\nu\mathbf{q}}\sum_{\mu\mathbf{p}}\left[\tilde{\Gamma}^{(\mathrm{1e1a})} + \tilde{\Gamma}^{(\mathrm{2e})} + \tilde{\Gamma}^{(\mathrm{2a})}\right] \tag{3.51}$$

where N is the number of phonon points sampled from the Brillouin zone, and sums are over all pairs of phonons that couple two electronic states, with the second phonon identified by branch index μ and wave vector $\mathbf{p}$. The superscripts refer to the three types of 2ph processes: emission and then absorption of a phonon (1e1a), emission of two phonons (2e), and absorption of two phonons (2a). The contribution of each type of 2ph process, indexed by superscript i, is given by:

$$\tilde{\Gamma}^{(i)} = A^{(i)}W^{(i)}\delta(\epsilon_{\mathbf{k}} - \epsilon_{\mathbf{k}'} - \alpha_{\mathbf{p}}^{(i)}\omega_{\mu\mathbf{p}} - \alpha_{\mathbf{q}}^{(i)}\omega_{\nu\mathbf{q}}) \tag{3.52}$$

where $\mathbf{k}'$ indexes the final state reached in the 2ph scattering process given by $\mathbf{k}' = \mathbf{k} + \mathbf{q} + \mathbf{p}$, $A^{(i)}$ is the weighting factor based on phonon and electron occupations which we discuss later to include the same modifications we make for high fields, $W^{(i)}$ is the 2ph process amplitude, and the constants $\alpha^{(i)}$ are determined by the type of scattering process, taking on the values given below:

$$\begin{array}{lll} \alpha_{\mathbf{p}}^{(\mathrm{1e1a})} = 1, & \alpha_{\mathbf{p}}^{(\mathrm{2e})} = 1, & \alpha_{\mathbf{p}}^{(\mathrm{2a})} = -1, \\ \alpha_{\mathbf{q}}^{(\mathrm{1e1a})} = -1, & \alpha_{\mathbf{q}}^{(\mathrm{2e})} = 1, & \alpha_{\mathbf{q}}^{(\mathrm{2a})} = -1 \end{array}$$

The 2ph process amplitude is given by:

$$W^{(i)} = \left|\left(\frac{g_\nu(\mathbf{k},\mathbf{q})g_\mu(\mathbf{k}+\mathbf{q},\mathbf{p})}{\epsilon_{\mathbf{k}'} - \epsilon_{\mathbf{k}+\mathbf{q}} + \alpha_{\mathbf{p}}^{(i)}\omega_{\nu\mathbf{p}} + i\eta - \Sigma_{\mathbf{k}+\mathbf{q}}} + \frac{g_\mu(\mathbf{k},\mathbf{p})g_\nu(\mathbf{k}+\mathbf{p},\mathbf{q})}{\epsilon_{\mathbf{k}'} - \epsilon_{\mathbf{k}+\mathbf{p}} + \alpha_{\mathbf{q}}^{(i)}\omega_{\nu\mathbf{q}} + i\eta - \Sigma_{\mathbf{k}+\mathbf{p}}}\right)\right|^2 \tag{3.53}$$

where $g_\nu(\mathbf{k},\mathbf{q})$ is the one-phonon matrix element corresponding to coupling between an electron at $\mathbf{k}$ scattering to an electron at $\mathbf{k}+\mathbf{q}$ through a phonon of mode ν at $\mathbf{q}$, and so on for the other matrix elements. The ϵ correspond to the band eigenvalues, ω are the phonon energies, $i\eta$ is an infinitesimal required to prevent divergences in the denominator, and $\Sigma_{n_1\mathbf{k}+\mathbf{q}}$ is the self-energy of the electron at $\mathbf{k}+\mathbf{q}$.

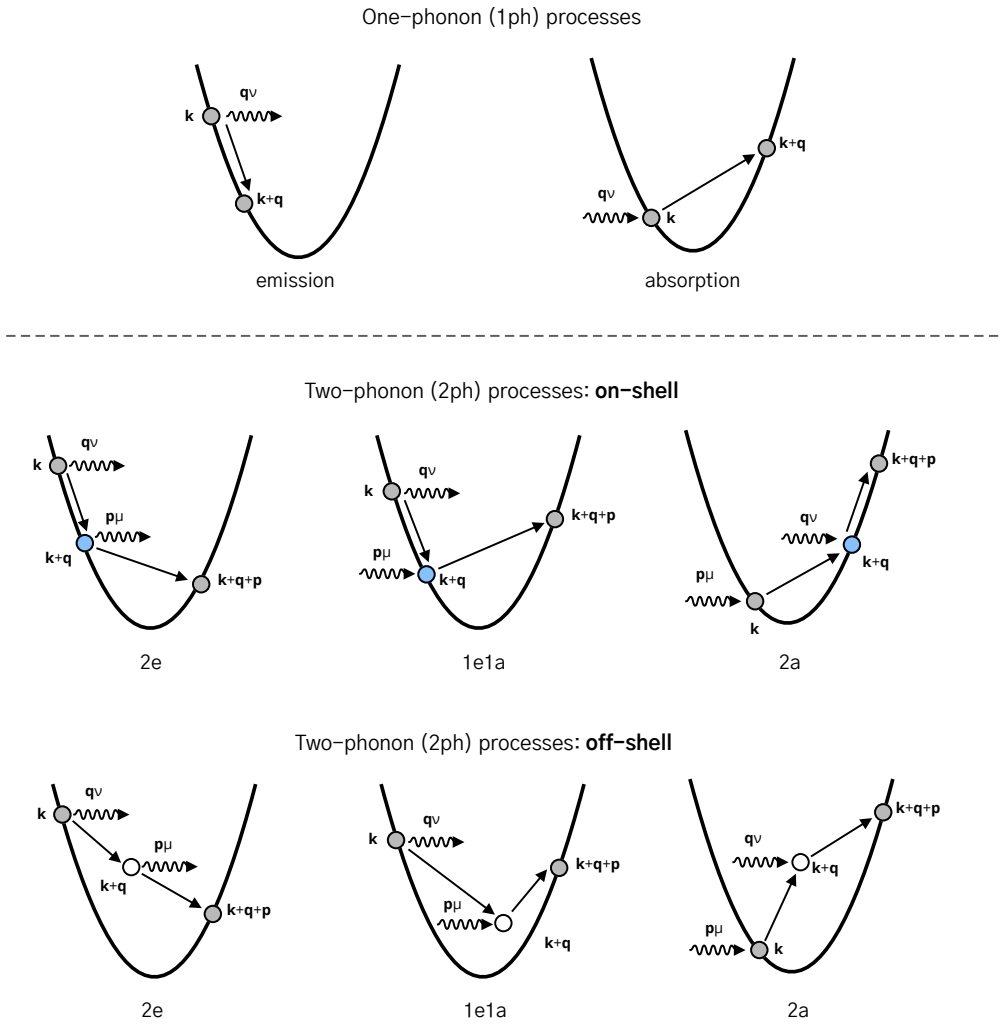

Figure 3.3: Schematic comparing one-phonon (1ph) scattering processes to two-phonon (2ph) processes. For 1ph, there is only phonon emission and absorption, whereas for 2ph there are 3 possible processes. For each of the three processes, we show both cases where the intermediate state can be on-shell, meaning the intermediate state reached is equal to the band energy; or off-shell, meaning the intermediate state is not equal to the band energy. The second row shows on-shell processes which are included in our calculation, and the intermediate state is blue to indicate the difference.

The 2ph framework differs from the 1ph framework in several ways; we note two particularly important differences indicated by Eqn. 3.53. First, the intermediate electron state reached after being scattering by the first phonon ($\epsilon_{\mathbf{k}} \pm \hbar\omega_{\mathbf{q}}$) is a virtual state that does not necessarily have the band energy ($\epsilon_{\mathbf{k+q}}$) at the corresponding point in the Brillouin zone. If the virtual state energy coincides with the band energy, the 2ph process is called "on-shell" or "resonant," and if it does not coincide with the band energy, the process is called "off-shell" or "non-resonant." The difference between the virtual energy and the band energy is called the off-shell extent. Second, the amplitude of a given 2ph scattering process depends on the self-energy of the intermediate state (Σ in the denominators of Eq. 3.53). We consider only the imaginary part of the self-energy which is directly proportional to the scattering rate at the intermediate state. Since the scattering rate should include both 1ph and 2ph scattering, the calculation for 2ph processes requires iteration until self-consistency, where the initial iteration approximates the intermediate state scattering rate as containing only 1ph processes and the resulting 2ph scattering rate is used in the next iteration. We show a schematic of all three types of 2ph processes alongside the conventional 1ph processes in Fig. 3.3. The 1e1a process is shown to be on-shell.

Including 2ph scattering at the fully ab initio level for high-field transport is prohibitively computationally expensive. We impose several approximations to make the calculation feasible. First, we include only 2ph processes with an intermediate state that is within a specified threshold of off-shell extent, meaning that the process is nearly "on-shell." This on-shell approximation is expected to capture many relevant 2ph processes owing to the 2ph rate being inversely proportional to the square of the off-shell extent (c.f. the denominator of Eq. 3.53). Although these on-shell 2ph processes consist of successive 1ph pathways, they directly couple electronic states that are not coupled by 1ph processes and may therefore qualitative alter the momentum and energy relaxation compared to the 1ph level of theory.

Second, we found empirically that increasing the number of self-consistent iterations beyond three did not lead to qualitative changes in the trend of computed observables, and we therefore employed three iterations rather than ten as in Ref. [98].

Next, we neglect the second term in the 2ph process amplitude of Eq. 3.53, which corresponds to the symmetric 2ph process where the order of scattering by phonons at wave vector $\mathbf{q}$ and $\mathbf{p}$ is reversed, leading to an intermediate state at $\mathbf{k}+\mathbf{p}$ instead of at $\mathbf{k}+\mathbf{q}$. Inclusion of this term increased the computational cost by around an order of magnitude while only changing the observables by around 10%, likely because the $\mathbf{k}+\mathbf{p}$ intermediate state is, in general, not on-shell if $\mathbf{k}+\mathbf{q}$ is on-shell.

Finally, let us discuss the form of the occupation weights $A^{(i)}$ which have the following expressions:

$$\begin{aligned} A^{(1e1a)} &= N_{\nu\mathbf{q}} + N_{\nu\mathbf{q}}N_{\mu\mathbf{p}} + N_{\mu\mathbf{p}}f_{\mathbf{k}'} - N_{\nu\mathbf{q}}f_{\mathbf{k}'} \\ A^{(2e)} &= \frac{1}{2}\Big[(1+N_{\nu\mathbf{q}})(1+N_{\mu\mathbf{p}}-f_{\mathbf{k}'}) - N_{\mu\mathbf{p}}f_{\mathbf{k}'}\Big] \\ A^{(2a)} &= \frac{1}{2}\Big[N_{\nu\mathbf{q}}(N_{\mu\mathbf{p}}+f_{\mathbf{k}'}) + (1+N_{\mu\mathbf{p}})f_{\mathbf{k}'}\Big] \end{aligned}$$

To be consistent with our approximations used to extend the 1ph collision integral to high fields, we also consider the electron occupation terms to be negligible. The resulting expressions are given by:

$$\begin{aligned} \tilde{A}^{(1e1a)} &= N_{\nu\mathbf{q}} + N_{\nu\mathbf{q}}N_{\mu\mathbf{p}} \\ \tilde{A}^{(2e)} &= \frac{1}{2}\Big[(1+N_{\nu\mathbf{q}})(1+N_{\mu\mathbf{p}})\Big] \\ \tilde{A}^{(2a)} &= \frac{1}{2}\Big[N_{\nu\mathbf{q}}N_{\mu\mathbf{p}}\Big] \end{aligned} \tag{3.54}$$

The 2ph rates we obtain with these approximations we term "on-shell 2ph" for the remainder of the paper. For the 2ph calculations, we include only processes with an off-shell extent of 25 meV or less, meaning the intermediate virtual state is within 25 meV of the band eigenvalue. We find that increasing this tolerance to 30 meV increases the 2ph rates by only 1.2%. When calculating noise and transport quantities with 2ph scattering, we are limited by computational tractability to a fine grid of $200 \times 200 \times 200$.

3.6 Summary

We have described the theoretical framework and numerical methods we use to calculate high-field transport and hot electron noise from first principles.

It required extending the collision integral to high fields by recognition of the important terms in the occupation weights which provided justification for neglecting non-linearities arising at high fields in GaAs. We also applied the reciprocal space gradient numerically to the deviational occupation expressed in terms of a linear operator. We then solve the steady state BTE directly as a linear system.

We then derived the expressions necessary for calculating the current PSD from the BTE. It required solving a Fourier transformed BTE for the occupation correlation function, which requires the steady stsate distribution function as an input. We simplified the expressions to show that, in practice, we solve for an "effective distribution function" which is summed to obtain the hot electron noise.

We discussed our method for including 2ph scattering processes which includes only on-shell type processes to permit computational tractability.

Finally, we note that while we have applied the method to GaAs in particular, it is easily extendable to other technologically interesting semiconductors where the Debye temperature is not too high and the carrier concentration is non-degenerate.

Chapter 4

ELECTRONIC NOISE AND HIGH-FIELD TRANSPORT IN GALLIUM ARSENIDE

This chapter has been adapted, in part, from:

> Alexander Y. Choi, Peishi Cheng, Benjamin Hatanpää, and Austin J. Minnich (Apr 2021). Electronic noise of warm electrons in semiconductors from first principles. In: *Phys. Rev. Materials* 5, pp. 044603. DOI: 10.1103/PhysRevMaterials.5.044603
>
> Peishi Cheng, Shi-Ning Sun, Alexander Y. Choi, and Austin J. Minnich (Jan 2022). High-field transport and hot electron noise in GaAs from first principles: role of two-phonon scattering. In: arXiv:2201.11912

We now show the results of our calculations based on the theory and numerical approach detailed in the previous chapter. As mentioned in Sec. 3.4, our results were reported in two papers [250, 251]. The first paper [250] reported calculations at intermediate electric fields less than 800 V cm^{-1} beyond the linear response regime of low fields, but without 2ph scattering. In this field range, we studied mechanisms important to non-equilibrium transport to establish concepts relevant to high-field transport. In the second half of the chapter, we show the calculations of the second paper [251] which extent to 5000 V cm^{-1}.

4.1 The warm electron regime

While at high fields the deviational occupation $\Delta f_{\mathbf{k}}$ exceeds the equilibrium population $f^0_{\mathbf{k}}$, there is a region of moderate electric fields where the nonlinearity in the collision integral is still small, but the field term can no longer be approximated by the effect of the electric field only on the equilibrium distribution, $\nabla_{\mathbf{k}} f_{\mathbf{k}} \neq \nabla f^0_{\mathbf{k}}$ since the reciprocal space gradient on the deviational occupation $\Delta f_{\mathbf{k}}$ is non-negligible. By including this additional electric field term but without modification of the collision integral, an appropriate solution can be obtained. This approximation was originally denoted as the "warm electron" approximation since the excess energy of the electrons over the thermal value can be non-zero while remaining small on that scale [255],

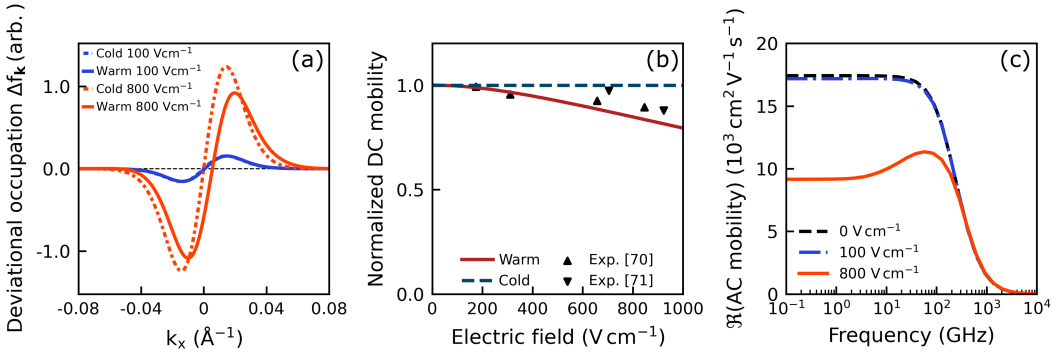

Figure 4.1: Deviational occupation, DC mobility, and AC mobility versus field in GaAs at warm electric fields. (a) Deviational occupation of the Γ valley in GaAs at 300 K versus electric field. Curves plotted for $E = 100$ V cm^{-1}(blue), and $E = 800$ V cm^{-1}(orange). The dashed black line is a guide to the eye. (b) Normalized longitudinal (||) DC mobility versus electric field of the cold (dashed blue line) and warm electrons (solid red line). The heating of the electrons leads to a decreased mobility. The trend of the normalized mobility agrees well with experiments: Figure 1, Ref. [228] (Upward black triangles) and Figure 4, Ref. [256] (Downward black triangles). (c) Real part of the longitudinal small-signal AC mobility versus frequency for equilibrium (dashed black line), $E = 100$ V cm^{-1}(dash-dot blue line), and $E = 800$ V cm^{-1}(solid orange line) under the warm electron approximation. The AC mobility exhibits spectral features at frequencies that are characteristic of the inverse momentum and energy relaxation times (see Section 4.2).

in contrast to the "cold electron" regime which entails the low-field approximations of Sec. 3.1.

We begin by examining the steady state distribution and associated transport observables in the cold and warm electron regimes. Figure 4.1a plots the deviational steady state distribution functions under the two approximations versus wave vector parallel to the electric field, k_x. We refer to this direction as the longitudinal direction. At low fields E < 100 V cm^{-1}, the solutions are nearly identical, but as the field increases, differences in the distribution functions emerge. Under the cold electron approximation, Eq. 3.15 shows that $\Delta f_{\mathbf{k}}$ is required to possess odd symmetry about the Brillouin zone center because $\partial f^0_{\mathbf{k}}/\partial_{\mathbf{k}}$ is odd with respect to k_x while the scattering matrix is even ($\Theta_{\mathbf{k}\mathbf{k}'} = \Theta_{-\mathbf{k}-\mathbf{k}'}$); this symmetry is evident in Fig. 4.1a. In contrast, in the warm electron case the electrons can be heated and the solution becomes asymmetric with increasing field.

The transport properties of the warm electron distribution differ from those of the cold distribution because warm electrons in the high energy tail are able to emit optical phonons and hence exhibit higher scattering rates. As reported previously [98], the predicted mobility of GaAs exceeds the experimental mobility owing to the exclusion of higher-order phonon scattering processes and the lower calculated effective mass (0.055 m_0) compared to experiment (0.067 m_0) [257].

Therefore, to facilitate comparison we examine the DC mobility normalized by its low-field value in Fig. 4.1b. The low-field value of the computed mobility is 17,420 $\mathrm{cm^2V^{-1}s^{-1}}$. At low fields $E < 100$ V $\mathrm{cm^{-1}}$, the mobility under the warm and cold electron approximations agrees to within 1%. At $E = 800$ V $\mathrm{cm^{-1}}$, the DC mobility of the warm electrons has decreased by more than 10%. This behavior is qualitatively consistent with the sublinear current voltage characteristic (CVC) of n-type GaAs [99], or a decrease in mobility with increasing electron temperature. The field dependence of the normalized mobility shows favorable comparison to experiment, implying that our calculation is properly capturing the heating with the field.

In addition to steady quantities, the small-signal AC mobility can be computed as in Eqn. 3.35. Figure 4.1c presents the small-signal AC mobility for the warm electron gas versus frequency for several electric fields. At zero frequency, the equilibrium AC mobility is equal to the equilibrium DC mobility, as expected. The decrease of the AC mobility with electric field at is also consistent with the trend observed in the DC mobility. At $f \sim 1$ THz, the AC field frequency exceeds the phonon-mediated scattering rates which redistribute the electrons, and thus the AC mobility rolls off at all fields. This result reflects the electrical response transitioning from a purely resistive to a purely reactive regime as the frequency exceeds the highest scattering rates.

The frequency dependence of the AC mobility indicates the relevant timescales of momentum and energy relaxation [258]. In particular, for 800 V $\mathrm{cm^{-1}}$, we observe a lower value of the AC mobility at low frequency, followed by a maximum at around 100 GHz. This feature is due to energy exchange with phonons and will be discussed in Section 4.2.

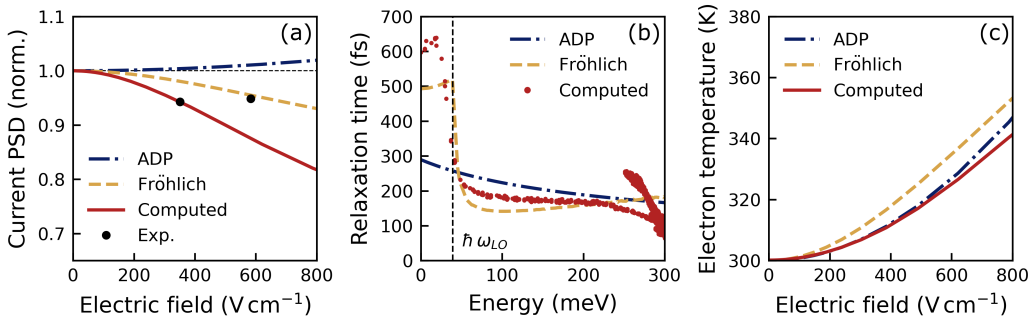

Figure 4.2: Longitudinal current power spectral density in GaAs versus electric field, relaxation times versus energy, and electron temperature versus electric field. (a) Spectral density of longitudinal current density fluctuations (solid red line) normalized to the Nyquist value versus electric field along with Davydov spectral densities calculated using ADP (dash-dot blue line) and Fröhlich (dashed yellow line). At equilibrium, the noise agrees with Nyquist-Johnson noise (dotted black line). The ab initio calculation predicts a steeper decrease in current PSD with field compared to the approximations. The symbols correspond to experimental measurements (Figure 11, Ref. [110]). (b) Relaxation time versus energy above conduction band minimum for GaAs at 300 K using ADP (dash-dot blue line), Fröhlich potential (dashed yellow line), and computed (red circles). The energy of the zone-center LO phonon is shown for reference (dashed black line). (c) Effective electron gas temperature versus electric field for ADP (dash-dot blue line), Fröhlich (dashed yellow line), and computed (solid red line). The magnitude of electron heating is similar among the various calculations.

PSD comparison to parameterized model

We now calculate the spectral density of current fluctuations from the non-equilibrium steady state in GaAs. Figure 4.2a shows the spectral density of longitudinal current fluctuations versus electric field at an observation frequency of 1 MHz, far smaller than any scattering rate. At equilibrium, the noise is given by the Nyquist relation, Eqn. 3.46. It is conventional to report the spectral density normalized to the Nyqist value to allow comparison between samples of different carrier density [100].

As the electric field increases, the computed noise decreases below the Nyquist value. Few experimental studies of noise in GaAs cover the fields of present interest, but reasonable agreement is observed with measurements by Bareikis *et al.* [110]. We note that a decrease with field is observed in other studies in

GaAs [217, 228] though the sparsity of data in the relevant electric field range prevents direct comparison.

To better understand the decreasing trend, we use an approximate solution of the Boltzmann equation for an electron gas interacting quasi-elastically with a thermal phonon bath [102, 201]. Under the quasi-elastic approximation, the distribution function is expanded in momentum space using Legendre polynomials. Because the distribution is nearly isotropic in momentum space under quasi-elastic scattering, only the two lowest Legendre polynomials need be retained [259]; the zeroth-order term gives the occupancy versus energy and is known as the Davydov distribution. The model is parameterized by the energy dependence of the momentum and energy relaxation times, τ and τ_ϵ respectively, and the inelasticity ratio τ/τ_ϵ [99]. Once these parameters are specified, the Davydov distribution can be computed and used with Eq. 3.43 to calculate the spectral density of current fluctuations [245].

Approximate analytic expressions for the electron relaxation times in semiconductors are available [234]. Previous works have calculated the Davydov distribution for a power-law energy dependence of the relaxation times such as that from the acoustic deformation potential (ADP) [260–262]. However, in GaAs at room temperature, the long-ranged Fröhlich interaction with longitudinal optical (LO) phonons is the dominant scattering mechanism [77, 78].

In Fig. 4.2a, we compare the ab initio longitudinal spectral density to that predicted using the Davydov distribution with the ADP and Fröhlich scattering rates. The approximate relaxation times have been scaled to match the computed low-field mobility, and the inelasticity ratio has been selected using an estimation of the energy and momentum relaxation times (see Fig. 4.3). The spectral density is observed to decrease monotonically with the electric field. This decrease is captured qualitatively by the Fröhlich calculation. In contrast, the ADP noise increases monotonically with field.

These trends can be understood in terms of the different energy dependencies of the relaxation times in the various approximations. Figure 4.2b shows the phonon-mediated relaxation times versus energy for electrons in GaAs at 300 K for the three cases. Below the zone-center LO phonon energy $\hbar\omega_{\mathrm{LO}} \sim$ 35 meV, the computed relaxation times are set by LO phonon absorption [77]. Above the LO phonon energy, LO emission becomes dominant and the relaxation times sharply decrease to a value that remains roughly constant

until electron energies are near the L-valley minimum at ~ 0.25 eV above the CBM. This absorption-to-emission transition is qualitatively captured by the Fröhlich approximation. The ADP relaxation times agree reasonably well with the computed ones in the emission-dominated region but do not exhibit the absorption-to-emission transition.

The electric field dependence of the spectral noise power reflects the balance between the growth of scattering rates with electron energy and the heating of the electron gas by the DC field [263]. To understand this balance, we examine the effective electron temperature of the steady distribution for the three cases in Figure 4.2c. The effective electron temperature is calculated as the temperature of a Maxwell-Boltzmann distribution that yields the same energy density as the steady state distribution. At low fields $E < 100$ V cm^{-1}, the temperature is equal to the lattice temperature. As the electric field increases, the effective temperature increases, corresponding to occupation at higher energies and increased scattering rates. Near equilibrium where the mobilities are equivalent, the temperature rise predicted from each approximation is similar, but at higher fields, the ab initio calculation predicts a slightly lower temperature than do either the ADP or Fröhlich approximations.

As the electron gas heats, higher energy states are occupied and thus the spectral noise power, Eq. 3.43, includes contributions from fluctuations in those states; hence, the spectral noise power may increase on heating. On the other hand, at these high energies, the scattering events which damp out fluctuations are more frequent, tending to decrease the noise. The competition between these mechanisms sets the trends shown in Figure 4.2a. For both Fröhlich and the present calculations, the sharp increase in scattering rates associated with the absorption-to-emission transition dominates, and the spectral density decreases monotonically with electric field. In contrast, the ADP approximation shows increasing noise with electric field as the heating of the electrons dominates the weak increase of the scattering rates.

The evolution of the spectral density with electric field demonstrates the sensitivity of the spectral noise power to the energy dependence of the scattering rates. Although the mobility at equilibrium is equivalent for all three cases, the non-equilibrium noise behavior exhibits qualitatively different trends depending on the energy dependence and inelasticity of the scattering mechanisms.

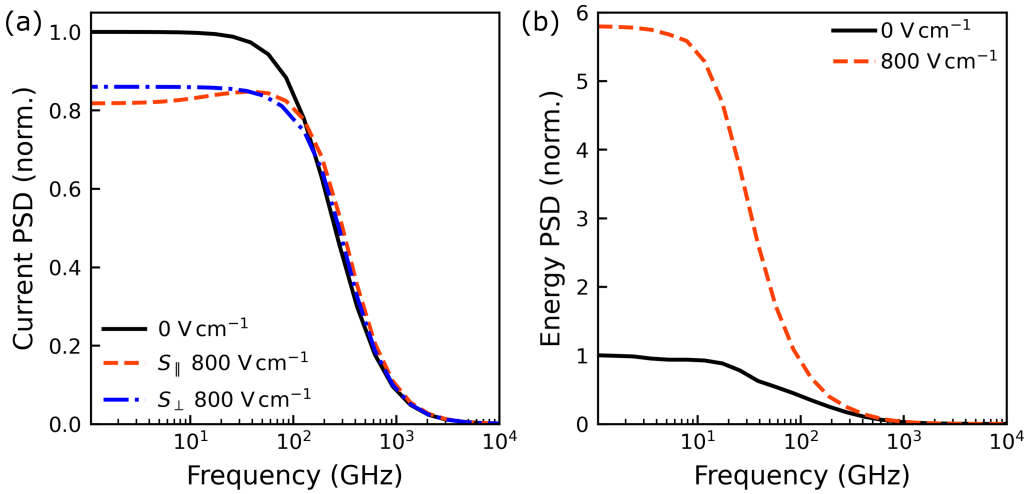

Figure 4.3: Longitudinal vs transverse PSD and spectral density of energy fluctuations versus frequency as a measure of energy relaxation time. (a) Computed power spectral density (PSD) of longitudinal ($\parallel$, dashed orange line) and transverse ($\perp$, dashed-dotted blue line) current density fluctuations versus frequency at $E = 800$V cm^{-1}, along with the Nyquist-Johnson prediction for $E = 0$ (solid black line). (b) Spectral density of energy fluctuations versus frequency at equilibrium (solid black line), $E = 800$ V cm^{-1}(dashed orange line). The time scale for electron temperature fluctuations sets the upper frequency limit for the convective mechanism.

4.2 Frequency dependence of electronic noise

The non-equilibrium noise exhibits spectral features that are not present in the Nyquist-Johnson case. Figure 4.3a shows the spectral density of longitudinal (L) and transverse (T) current fluctuations (relative to the electric field axis) versus frequency at $E = 800$ V cm^{-1}. There are several notable features of the spectral density in this figure. First, the spectral density is constant at low frequencies and rolls off as frequency increases, decreasing to 50% of its low frequency value at 300 GHz. Secondly, an anisotropy exists between the longitudinal and transverse spectral densities. Finally, the longitudinal noise exhibits a non-monotonic trend for frequencies around 50 GHz, similar to that observed for the AC mobility in Fig. 4.1c. Spectroscopic measurements of the noise power at these frequencies have not been performed, but these trends are qualitatively similar to those observed in recent Monte Carlo simulations [264].

We discuss each of these points in turn. Consider first the noise at equilibrium. The zero-field curve shows that the longitudinal and transverse spectral densities are equal and coincide with the Nyquist-Johnson value, Eqn. 3.46. As with the AC mobility, the spectral density rolls off at frequencies exceeding the phonon-mediated scattering rates because the electronic system cannot redistribute in response to the fluctuation. This roll-off behavior has been noted previously [255] and has also been observed for phonon thermal conductivity (see Fig. 1b in Ref. [265]).

Now consider the noise with $E = 800$ V cm^{-1}. A similar roll-off with increasing frequency as the equilibrium case is observed. At low frequency, both the longitudinal and transverse spectral densities are lower than the Nyquist value because of the increased electron temperature. However, an anisotropy exists in the spectral densities. The origin of this feature is the "convective" mechanism [99, 102, 266] and can be understood by decomposing the current fluctuations into two sources. The first is the fluctuation of the drift velocity, due to scattering between states of differing group velocity. The second is the fluctuation of the electron temperature, due to the energy exchange with the thermal phonon bath which depends on the energy of the states undergoing scattering. Under non-equilibrium conditions, these fluctuations couple. As the gas is heated by the electric field, the fluctuating current induces a variation in the Joule heating. The resulting electron temperature fluctuation changes the conductivity, which in turn modifies the current. This coupling only exists for fluctuations longitudinal to the electric field because transverse fluctuations do not affect Joule heating. In sublinear CVC materials such as GaAs, the conductivity decreases with electron temperature, and the convective mechanism suppresses longitudinal fluctuations. This feature is indeed observed in Fig. 4.3a.

The convective mechanism is only present at frequencies $\omega\tau_\epsilon \ll 1$, where τ_ϵ is the energy relaxation time. As discussed above, the local maxima from the convective contribution appears at $\omega\tau_\epsilon = 1$ in the longitudinal direction (see Ref. [99], Chapter 7). The energy relaxation time can also be extracted by calculating the spectral density of electron temperature fluctuations versus frequency. This calculation is the energy analogue of Eqn. 3.43, where the relevant state quantity is the energy instead of the group velocity. The expression

is given below:

$$S_{\delta T_e \delta T_e}(\omega) = 2\left(\frac{2e}{V_0}\right)^2 \Re\left[\sum_{\mathbf{k}} \epsilon_{\mathbf{k}} \sum_{\mathbf{k}'} (i\omega\mathbb{I} + \Lambda)^{-1}_{\mathbf{k}\mathbf{k}'} \sum_{\mathbf{k}_1} \epsilon_{\mathbf{k}_1} \left(f^s_{\mathbf{k}'}\delta_{\mathbf{k}'\mathbf{k}_1} - \frac{f^s_{\mathbf{k}'} f^s_{\mathbf{k}_1}}{N}\right)\right] \tag{4.1}$$

Figure 4.3b shows the spectral density of energy fluctuations versus frequency for several electric fields. At low frequencies, $f < 10$ GHz, the spectral density increases with field as the temperature fluctuations rise with higher Joule heating. At higher frequencies, $f \sim 50$ GHz, the energy fluctuations decrease to 50% of their low frequency values and begin to converge for the two fields shown. This convergence signifies that the temperature of the electron gas cannot change sufficiently rapidly due to its finite thermal capacitance. Consequently, the convective noise mechanism is removed and the anisotropy of the densities in Fig. 4.3a also disappears; the longitudinal and transverse spectral densities converge. The convective mechanism is also responsible for the non-monotonic trend of the AC mobility seen in Fig. 4.1c.

4.3 Quasi-elastic scattering

The present formalism for electronic noise permits the study of the microscopic processes responsible for electronic noise in a manner that is difficult to obtain by other methods. As an example, consider the spectral features present in Fig. 4.3. Comparing the frequency where the current power spectral density and energy power spectral density reach half of their low frequency values (300 GHz versus 50 GHz, respectively), the energy relaxation time is inferred to be around 6 times longer than the momentum relaxation time, implying that the quasi-elastic assumption is valid. This observation is surprising given the well-known dominance of high-energy LO phonon emission in GaAs [77] and that inelasticity is expected when the physical temperature is comparable to the Debye temperature [255]. Analytical treatments of noise under dominant LO phonon coupling typically assume strongly inelastic interactions between the electrons and lattice (see Sec. 3.8 of Ref. [102], Sec. 7.3 of Ref. [99], or Ref. [267]).

We identify the origin of this discrepancy by examining how individual scattering events contribute to the momentum and energy relaxation of the electron system to the phonons. These transfers can be expressed as sums over each of

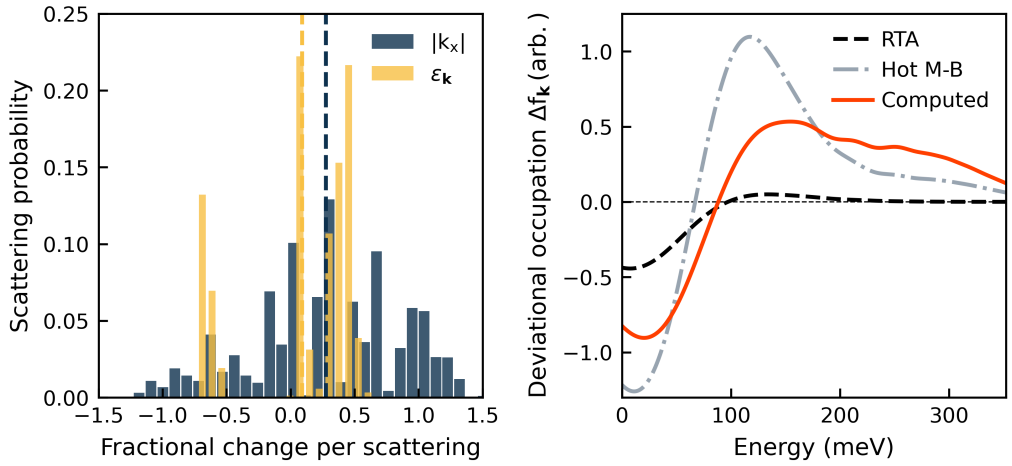

Figure 4.4: Histogram of momentum and energy loss, and deviational occupation versus energy of calculated cases versus various approximations. (a) Probability histograms of longitudinal momentum loss $R_{\mathbf{k}}$ (blue bars) and energy loss $R_{\epsilon_{\mathbf{k}}}$ (yellow bars) normalized by the thermal averages at 800 V cm^{-1}. The dashed lines represent the average transfer per scattering event. At this field, the average fractional dissipation of longitudinal momentum is $\sim 3\times$ larger than that for energy. (b) Deviational occupation $\Delta f_{\mathbf{k}}$ in GaAs at 300 K versus energy calculated under the RTA (dashed black line), hot Maxwell-Boltzmann (dashed-dotted grey line), and ab initio warm electron approximation (solid orange line) at 800 V cm^{-1}. The dashed black line is added as a guide to the eye. Neither the RTA nor the Maxwell-Boltzmann capture the hot electron tail.

the electron-phonon scattering processes in the collision integral weighted by the energy and momentum of the mediating phonon. Every electronic state in the BZ is coupled via phonons to other states; by summing over all possible scattering processes, we obtain the average energy and momentum exchanged in a single scattering event. More precisely, the fractional change in momentum and energy per scattering event are calculated from:

$$R_{k_x}(\mathbf{k}) = \frac{1}{\Theta_{\mathbf{k}}|k_x|}\sum_{\mathbf{k}'}(k_x - {k'}_x)\Theta_{\mathbf{k}'\mathbf{k}} \tag{4.2}$$

$$R_{\epsilon_{\mathbf{k}}}(\mathbf{k}) = \frac{1}{\Theta_{\mathbf{k}}\epsilon_{\mathbf{k}}}\sum_{\mathbf{k}'}(\epsilon_{\mathbf{k}} - \epsilon_{\mathbf{k}'})\Theta_{\mathbf{k}'\mathbf{k}} \tag{4.3}$$

$\Theta_{\mathbf{k}}$ is the scattering rate for state $\mathbf{k}$ which is -1 times the diagonal element of the scattering matrix. $\Theta_{\mathbf{k}'\mathbf{k}}$ is the scattering rate from state $\mathbf{k}$ to state $\mathbf{k}'$.

These expressions capture the dissipation of momentum and energy for a given state as a fraction of the momentum and energy at that state.

These fractional changes at 800 V cm^{-1}are plotted as a probability histogram in Figure 4.4a. In this figure, we have binned each state by the value of $R_{\mathbf{k}}$ and $R_{\epsilon_{\mathbf{k}}}$. For all the states in a given bin, we calculate the probability of scattering $\mathcal{P} \propto \sum_{\text{bin}} \Theta_{\mathbf{k}} f^s_{\mathbf{k}}$ (the final quantity is normalized to unity). The horizontal position indicates the average fractional change in energy or momentum induced by the event. Positive values of the fractional change correspond to net transfers to the lattice, or dissipation, while negative values correspond to transfers to the electrons, or accumulation. The height of a bar represents the probability of scattering in a given time interval, weighted by the steady state distribution at 800 V cm^{-1}.

Figure 4.4a reveals several important features. First, energy transfers are clustered into two groups. The grouping of accumulation events around -0.75 corresponds to the ~ 35 meV energy gain associated with LO absorption, which dominates scattering of electrons below the emission threshold $\hbar\omega_{\text{LO}}$. The relatively disperse grouping of the dissipation events reflects a balance between LO emission and absorption for states above the threshold. Second, in contrast to energy transfers, momentum transfers grow with the wave vector of the mediating phonon. Consequently, a broader and more disperse distribution of momentum transfers is available. Finally, the balance between dissipation and accumulation differs between energy and momentum. In equilibrium, these processes are balanced, but at 800 V cm^{-1}, the net transfers for both quantities are dissipative as the warm electrons transfer excess momentum and energy to the lattice. The dashed lines in the figure represent the average fractional transfer per scattering event and indicate that the net momentum dissipation exceeds the energy dissipation by around a factor of 3. This imbalance is partly responsible for the disparate time scales of energy and momentum relaxation observed in Fig. 4.3.

The second contributing factor to the relatively long energy relaxation time is the presence of a hot electron tail in the calculated distribution. In Fig. 4.4b, we plot the steady deviation distribution, Δf_s, calculated under the warm electron approximation using the full e-ph scattering matrix versus energy. For reference, the corresponding distributions for a hot Maxwell-Boltzmann at the non-equilibrium electron temperature and a 'relaxation-time distribution'

obtained under the warm electron approximation with only the on-diagonal elements of the scattering matrix. The ab initio treatment predicts a hot electron tail that is not observed with either approximate method. Although representing only a small fraction of the population, these hot electrons are at energies 5-10× the thermal average value. Consequently, many scattering events are needed to return these electrons to equilibrium, further increasing the energy relaxation time. The result is that the quasi-elastic approximation is unexpectedly accurate despite the inelastic nature of optical phonon scattering, and thus explaining the features in the spectral noise power and AC mobility.

Summary of findings from warm electron regime

We have calculated the transport and noise properties in GaAs beyond the low-field linear response approximations employed in studies of mobility only. We have shown that the distribution function becomes asymmetric as a result of relaxing the low field approximations. We have also shown how the trend of the PSD versus field can be thought of as a balance between scattering and electron heating, where scattering damps out fluctuations and reduces PSD while heating the electrons to high energies tends to increase the PSD. We show how using the Davydov distribution predicts the wrong trend for the PSD due to incorrectly capturing this balance of scattering and electron heating. We have shown how the frequency dependence of the PSD reflects the timescales of the e-ph scattering rates, and that anisotropy in the PSD can be understood through the differing timescales of energy and momentum relaxation. We showed that at these intermediate electric fields less than 800 V cm^{-1}, the scattering is still approximately quasi-elastic.

4.4 High field transport: Drift velocity

Let us now show the transport behavior at high electric fields. We first consider the drift velocity versus electric field at the 1ph level of theory, presented in Fig. 4.5. The base calculation is observed to qualitatively reproduce several trends, including the linear increase of the drift velocity with electric field below 1 kV/cm, followed by a rapid decrease and a region of negative differential mobility. However, the low-field mobility, corresponding to the slope of the drift velocity at low electric fields, is markedly overestimated, with the

predicted mobility of 18,570 $cm^2V^{-1}s^{-1}$ exceeding the experimental value of around 8,000 $cm^2V^{-1}s^{-1}$[257] by over a factor of two.

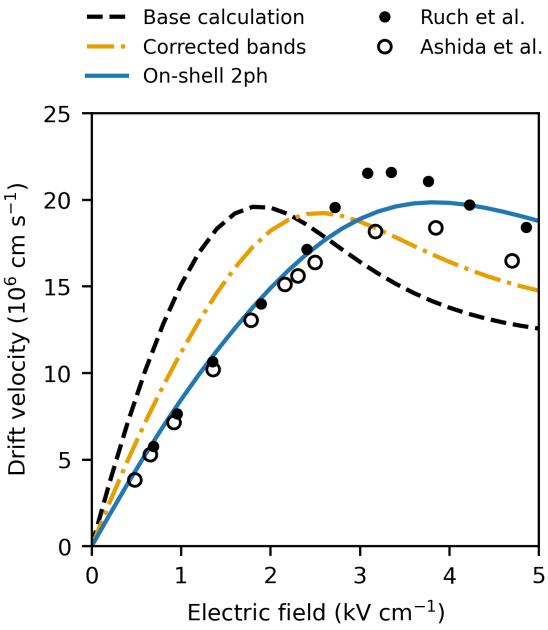

Figure 4.5: Drift velocity versus electric field for the base calculation (dotted black curve), the corrected bands case (dot dashed orange curve), and the on-shell 2ph case (solid blue curve), as described in the text. The inclusion of on-shell 2ph processes gives the best agreement of the three cases with the experimental drift velocity measurements of Ruch et al. [191] and Ashida et al. [268].

Some of the discrepancies in the drift velocity curve can be attributed to inaccuracies in the DFT band structure. First, the computed effective mass is overestimated compared to experiment (0.055 m_e versus $0.067m_e$, respectively) [97]. Second, the minimum of the L valley in the DFT band structure are at 250 meV above the conduction band minimum (CBM) instead of 300 meV as in experiments [257, 269]. To quantify the correction to the drift velocity due to the band structure, we replace the energy eigenvalues of states in the Γ valley with those calculated using a spherically symmetric band structure model [201] with the experimental effective mass of $0.067m_e$ and a non-parabolicity of 0.64 [234]. We also rigidly shift the DFT band energies in the L valleys by 50 meV to achieve the experimental Γ-L valley separation of 300 meV. We note that while other works have obtained band structures closer to experiment using *GW* corrections [78, 97, 98], prior analysis for GaAs has argued that the main

effect of these corrections is to alter the effective mass rather than the e-ph coupling strength [97].

The drift velocity versus electric field with these corrections, denoted "corrected bands," is plotted in Fig 4.5. The agreement of the velocity field curves with experiment is improved, with a low-field mobility of 12,674 $cm^2V^{-1}s^{-1}$, but the slope of the drift velocity curve remains overpredicted.

4.5 Two-phonon scattering rates

It has been reported that the low-field mobility of GaAs, and thus the slope of the drift velocity versus field curve, is overestimated even with corrections to the band structure, and that additional scattering from 2ph processes is necessary to achieve improved agreement with experiment [98]. To assess the impact of these corrections on the high-field drift velocity, we computed the on-shell 2ph scattering rates as specified in Sections 3.5 and 3.4. These calculations employed the corrected band structure described above to facilitate comparison of the effects of 2ph scattering relative to the effective mass correction.

The effect of the additional on-shell 2ph scattering on the drift velocity is shown in Fig. 4.5. The agreement of the calculated drift velocity with experiment improves further, with the low-field mobility computed to be 9086 $cm^2V^{-1}s^{-1}$, within 15% of the experimental value. Further, the threshold field for the onset of negative differential resistance is around 3.8 kV/cm, which agrees better with the experimental value around 3.5 kV/cm [257] than either of the cases with 1ph scattering.

To gain more insight, we examine various features of the on-shell 2ph rates, which have not yet been reported for energies above 100 meV where processes relevant to high-field transport such as intervalley scattering and energy relaxation occur. In Fig. 4.6a, we show the on-shell 2ph scattering rates versus energy above the CBM along with the 1ph scattering rates with the corrected bands. We find that the on-shell 2ph rates are comparable to the 1ph rates over the entire energy range up to 375 meV, with a magnitude slightly less than half of the 1ph rates. Between 100 meV and 300 meV, the 2ph scattering rates are roughly constant, and increase above 300 meV. This trend is also observed in the 1ph rates and is attributed to the onset of intervalley scattering.

The on-shell 2ph rates are smaller but within a factor of 2 of the full 2ph rates reported in Ref. [98] for energies below 100 meV. This underestimate is expected given the neglect of most off-shell 2ph processes in our calculation. The full 2ph rates include scattering from virtual states that can be arbitrarily far from the band energy and thus include many additional processes. Although the contribution to the scattering rate of an individual off-shell process decreases with off-shell extent per Eqn. 3.53, the large phase space for such processes may compensate so that the final off-shell scattering rate is non-negligible.

Figure 4.6b shows the fraction of processes involving two LO phonons versus energy. Below 200 meV, greater than 90% of the on-shell 2ph processes involve only LO phonons, but at higher energies near and above the minimum of the L valleys, a substantial fraction of the 2ph processes involve phonons other than the LO mode. In Ref. [98], only 2ph processes involving LO phonons were considered, and the figure shows that such an approximation is justified for the low-energy scattering rates relevant for the low-field mobility. However, it is known that intervalley scattering is mediated through all phonon modes, [77, 78, 97, 124, 125] not just the LO mode, thereby explaining why the contribution of non-LO phonons becomes increasingly important at higher energies. For energies exceeding 350 meV, more than half of the scattering processes involve non-LO phonons.

To assess the magnitude of intervalley scattering due to 2ph processes, we plot the intervalley scattering rates for transitions from the Γ valley to the L valley in Fig. 4.6c. The 2ph intervalley rates become non-negligible around 275 meV and are around half the magnitude of the intervalley rates in the 1ph framework, enhancing the overall strength of intervalley scattering when including on-shell 2ph. Prior numerical studies of transport experiments have not included 2ph intervalley scattering processes, which has consequences for the interpretation of transport experiments as discussed in Section 4.9.

Figure 4.6d shows the 2ph scattering rates in the L valleys. We observe that the scattering rates are up to half of the values for 1ph scattering, particularly near the L valley minimum. At higher energies, the 2ph rates are a smaller fraction of the 1ph rates due to the dependence of the 2ph rates on the self-energy of the intermediate state in the denominator of the 2ph process amplitude (Eqn. 3.53). The scattering rates and thus imaginary part of the self-energies

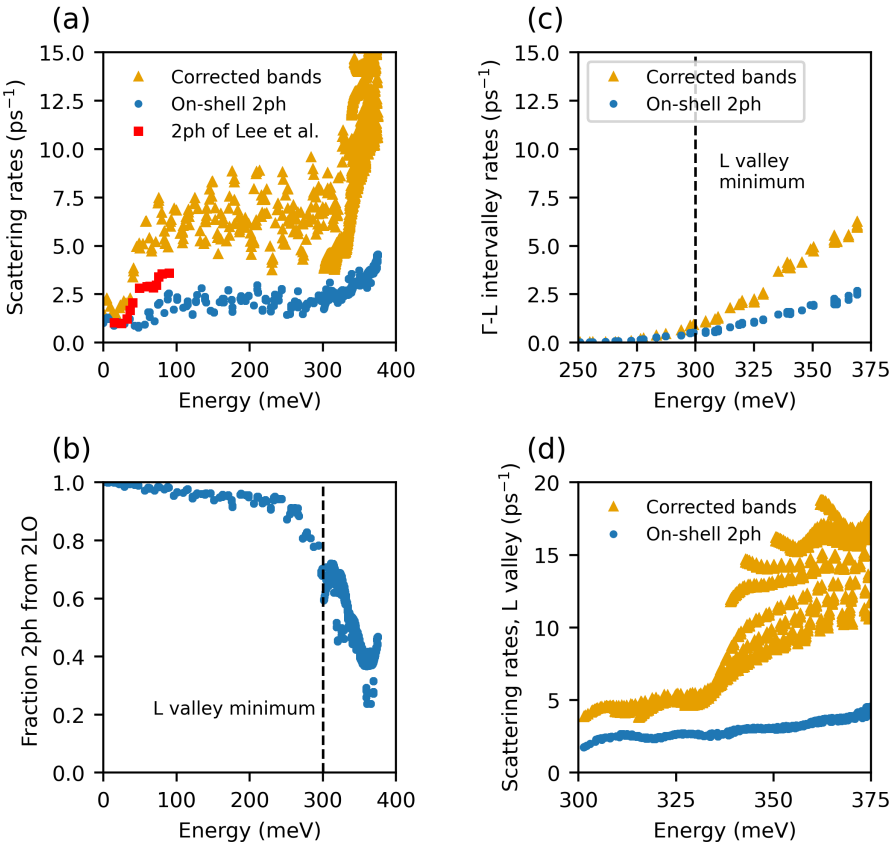

Figure 4.6: Scattering rates from on-shell 2ph processes versus energy. (a) 1ph scattering rates from the corrected bands case (orange triangles), the on-shell 2ph rates (blue dots), and the full 2ph rates iterated to self consistency as given in Fig. 4 of Ref. [98] (red squares). The increase in scattering rates around 0.3 eV is due to the onset of intervalley 2ph processes. (b) Fraction of the on-shell 2ph rates coming from processes mediated by LO phonons only. As intervalley scattering becomes permitted, non-LO phonons participate in 2ph scattering. (c) Intervalley scattering rate for states in Γ scattered to the L valley. The on-shell 2ph intervalley scattering is around half of the magnitude of 1ph intervalley scattering. (d) On-shell 2ph rates in the L valley. The on-shell 2ph rates are comparable to the 1ph rates below 330 meV, but become a smaller proportion of the 1ph scattering rates above 330 meV due to the increase in the intermediate state scattering rate.

for the intermediate states becomes larger at higher energies, and the 2ph process amplitude decreases, reducing the strength of 2ph scattering.

4.6 Valley occupation and high field distribution

We now consider how the steady-state distribution function and valley occupations are altered by the inclusion of on-shell 2ph scattering. Intervalley scattering causes the transfer of population from the light Γ valley to the higher mass L valley, which is the origin of negative differential resistance underlying the Gunn effect. We first investigate this transfer by plotting the fraction of the steady-state population in the L valley versus electric field in Fig. 4.7a. We observe that the base calculation predicts the most carriers in the L valley, followed by the corrected bands case and then the 2ph case. This feature can be partly attributed to the L valley being lower in energy in the DFT bands compared to the other two cases. In the corrected bands case where the valley separation was increased by 50 meV and the effective mass increased, fewer electrons have sufficient energy to transfer, and hence the L valley population is lower. However, the on-shell 2ph case has substantially fewer carriers in the L valley than even the corrected bands case, despite having increased intervalley scattering rate as shown in Fig. 4.6d.

To identify the origin of this unintuitive feature, we plot the steady-state distribution function for an electric field of 3 kV/cm in Fig. 4.7b. The distribution function for the base calculation exhibits a clear peak around 250 meV, indicating that substantial population has transferred to the L valley. In the corrected bands case, the peak is weaker and begins at 300 meV, reflecting the rigid shift in the L valley energy. The corrected bands distribution function also has a higher population in the Γ valley, consistent with Fig. 4.7a, due to the higher effective mass which inhibits the heating of the carriers. Finally, the distribution for the on-shell 2ph case exhibits still higher population for energies below 200 meV and markedly reduced L valley population.

4.7 The effect of two-phonon scattering on energy relaxation rate

These features of the distribution function in the on-shell 2ph case reflect the increased momentum and energy dissipation contributed by 2ph processes. First, the on-shell 2ph scattering rates increase the total scattering rate by about 50%, decreasing the mobility by around the same factor. Recalling that the Joule heating per carrier is given by μE^2 [270], the Joule heating of the electrons therefore decreases with the on-shell 2ph rates added. In addition to this reduced Joule heating, energies of the final states reached by 2ph scattering processes involve combinations of phonons and thus the energy

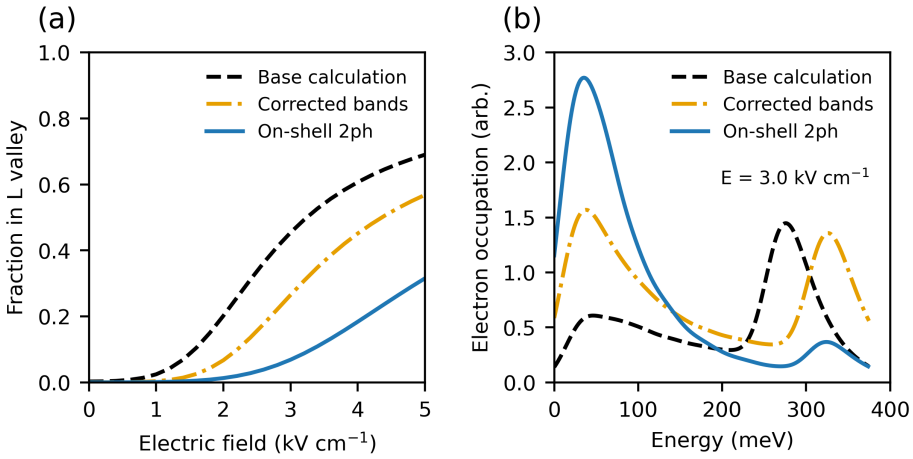

Figure 4.7: Occupation of L valley versus electric field, and steady state distribution at a representative electric field. (a) Fraction of carriers in t. he L valley at steady state versus electric field for the three cases described in the text. The on-shell 2ph case has the slowest accumulation of carriers in the L valley despite having increased intervalley scattering compared to the other two cases. (b) Steady-state distribution function versus energy at 3 kV/cm for the three cases. The on-shell 2ph distribution has fewer carriers at high energy.

relaxation mechanisms due to 2ph processes may qualitatively differ from those of 1ph processes in which phonons are only emitted or absorbed.

To gain more insight into energy relaxation by 2ph processes, we first disaggregate the 2ph scattering rate by the process type. Recall that there are three types of 2ph processes: emission and then absorption of a phonon (1e1a), emission of two phonons (2e), and absorption of two phonons (2a). For 1ph scattering events, the electrons gain energy when absorbing a phonon and lose energy when emitting a phonon. For 2ph scattering, 2a processes cause energy gain, 2e processes cause energy loss, and 1e1a processes lead to little energy change when mediated by phonons of similar energy, which is approximately true for 2ph scattering below 200 meV involving only LO phonons with little dispersion. When considering only LO phonon processes, the 2e and 2a processes produce approximately twice the energy loss or gain of the corresponding 1ph process. Thus, 2ph processes may substantially alter the energy relaxation compared to the 1ph case.

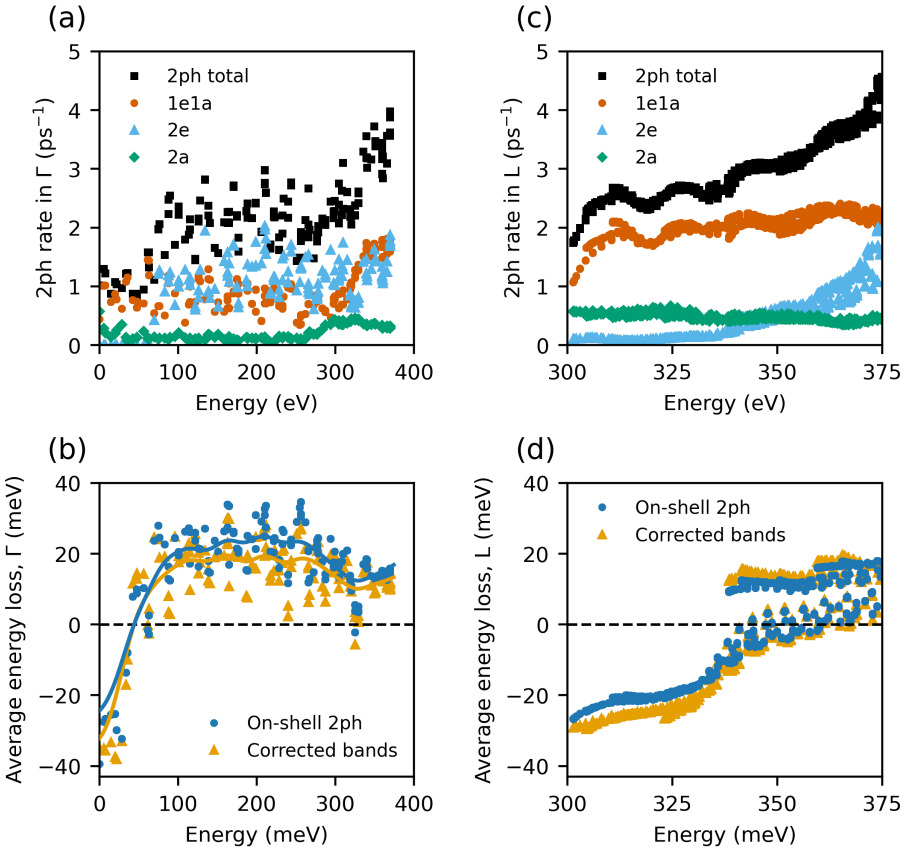

Figure 4.8: 2ph rates by process type and corresponding energy loss. (a) Breakdown of 2ph process type versus energy in the Γ valley. At low energies, the 1e1a rate (red dots) comprises nearly all of the total 2ph rate (black squares). Above 100 meV, the 2e rate (blue triangles) has the largest contribution of the three types. The 2a rate (green diamonds) remains small at all energies. (b) Average energy loss versus electron energy in the Γ valley. The on-shell 2ph case has noticeably higher energy loss between 100 meV and 300 meV where the 2e rates are strongest. (c) Breakdown of 2ph process type versus energy in the L valley. The 1e1a rates are the dominant type, with 2a rates having a weak energy dependence and contributing most at the L valley minimum. The 2e rates are small but within an order of magnitude of the 1e1a and 2a rates even at the valley minimum. (d) Average energy loss versus energy in the L valley showing the less negative (closer to zero) energy loss of the on-shell 2ph case near the valley minimum due to the dominance of 1e1a processes.

The scattering rate for each type of 2ph process in the Γ valley is shown in Fig. 4.8a. We observe that at low energies below 60 meV, only 1e1a and 2a processes are present, with the 1e1a being the dominant process. This result is consistent with that reported for the full 2ph calculation (Fig. 5 in Ref. [98]). No 2e processes are allowed below 60 meV since the emission of two LO phonons would result in a final state with an energy in the band gap. Starting around 60 meV, 2e processes are energetically allowed, and above 100 meV they are larger in magnitude than the 1e1a processes. The 1ph case exhibits less structure because the only allowed processes are single phonon absorption and emission, leading to a single transition to phonon emission dominated scattering at around 35 meV as in Fig. 4.6a. As intervalley transitions become possible around 275 meV, 2a and 1e1a processes increase their contribution, while 2e processes do not increase until slightly above 300 meV since reaching the L valley minimum through emission of two phonons requires starting at higher energies in the Γ valley.

We next compute the average energy loss versus the energy of electrons in the Γ valley. The average energy loss for a state at wave vector $\mathbf{k}$ is given by the following equation:

$$\langle \epsilon^{\text{loss}} \rangle_{\mathbf{k}} = \frac{1}{\Theta_{\mathbf{k}}} \sum_{\mathbf{k}'} (\epsilon_{\mathbf{k}} - \epsilon_{\mathbf{k}'}) \Theta_{\mathbf{k},\mathbf{k}'} \tag{4.4}$$

where $\Theta_{\mathbf{k}}$ is the total scattering rate for state $\mathbf{k}$ due to all scattering processes, $\epsilon_{\mathbf{k}}$ is the energy of the state at $\mathbf{k}$, and $\Theta_{\mathbf{k},\mathbf{k}'}$ is the scattering rate from state $\mathbf{k}$ to state $\mathbf{k}'$. This weighted average quantifies the average energy exchanged with the lattice by an electron after scattering considering all types of emission and absorption processes. A positive energy loss means that, on average, carriers at that energy tend to emit phonons and lose energy, while a negative energy loss means that carriers tend to absorb phonons and gain energy.

The result for the corrected bands and on-shell 2ph cases are given in Fig. 4.8c, with the average value at each energy plotted as a solid line as a guide to the eye. Below 35 meV, the average energy loss is negative with a value around −35 meV for the corrected bands case, corresponding to the LO phonon absorption dominated scattering. The on-shell 2ph case shows a slightly less negative energy loss because the 1e1a processes which dominate at low energy are nearly elastic, shifting the average energy loss towards zero. Above 35 meV in the corrected bands calculation, LO phonon emission processes are energetically

allowed and begin to dominate the scattering, leading to a positive energy loss. For the on-shell 2ph case, as 2e processes start to dominate above 100 meV, the average energy loss increases and ends up about 20% higher (5 meV) than the corrected bands result between 100 and 250 meV. Near the energy of the L valley minimum, the increased contribution of 1e1a and 2a processes above 275 meV reduces the difference in energy loss between the on-shell 2ph and the corrected bands case.

We note that there is a difference between the quantity calculated here in Fig. 4.8 versus the quantity calculated for the warm electron regime in Fig. 4.4. The quantity in Fig. 4.4 is given as a fraction of the energy and momentum at a given state, weighted by the steady state distribution function at some electric field. The quantity here is independent of electric field. This explains the quasi-elastic result of Fig. 4.4, since at the moderate electric field of 800 V cm^{-1}, the steady state distribution function is still heavily weighted to lower energies, meaning that the energy absorption at low energy states balances out the dominance of energy loss at higher energy states, resulting in a small net energy loss and thus long energy relaxation time that leads to the quasi-elastic condition.

The observation of higher average energy loss for 2ph processes in Fig. 4.8 helps to explain the slower accumulation of carriers in the L valley for the on-shell 2ph case. In addition to the decreased power input from Joule heating owing to the lower mobility, 2ph processes are able to more effectively cool the electronic system, decreasing the population with sufficient energy to transfer to the L valley.

We now examine the categorization by 2ph scattering process and the average energy loss for the L valley, shown in Figs. 4.8b and 4.8d, respectively. For the scattering categorization, we observe a qualitatively similar trend as in the Γ valley, where the majority of the 2ph scattering near the L valley minimum is 1e1a, with 2a scattering rates depending only weakly on energy. The 2e rates increase rapidly around 330 meV and exceed the 1e1a rates near the edge of the energy window (375 meV).

A difference in the 2e rates compared to the Γ valley is that the L valley 2e rates are within an order of magnitude of the 1e1a and 2a rates for energies less than 60 meV above the valley minimum (< 360 meV), while those in the Γ valley are orders of magnitude smaller. This nonzero 2e rate can be attributed to

two factors. First, the e-ph matrix elements for acoustic mode scattering in the L valley are around 4 to 10 times larger than those in the Γ valley so that the scattering rate associated with the emission of two low energy, zone-center acoustic modes is much larger than in Γ, though still weaker than either 1e1a or 2a processes by at least a factor of five due to the low density of states for zone-center acoustic phonons.

Second, electronic states exist in Γ at energies below the L valley minimum whereas they do not exist below the Γ minimum. However, these states can only be reached through intervalley scattering. Since our 2ph calculation is restricted to on-shell processes, 2e processes involving L to Γ intervalley transitions must take successive 1ph pathways, which are few in comparison to other scattering pathways in L due to the small effective mass of the Γ valley. Thus, the 2e processes are nonzero but still smaller in magnitude than 1e1a or 2a for energies below 330 meV. However, once an intermediate state can be reached that is near the L valley minimum, the 2e rate rises because 2ph processes involving L-L intervalley or L-intravalley phonons together with an L-Γ intervalley phonon may occur. The L-L intervalley phonons have large wave vector with energies on the order of 30 meV [78], and the L-intravalley phonons are LO phonons of comparable energy, explaining why the 2e rate rises around 330 meV.

Next, we plot the average energy loss from the on-shell 2ph case versus the corrected bands case in Fig. 4.8d. The corrected bands case with 1ph scattering has negative energy loss (energy gain) below 340 meV because scattering is dominated by phonon absorption, as was the case for the Γ valley. The Γ states that are below the L valley minimum in energy are not immediately accessible via phonon emission due to the large wave vector and high energy phonons needed to mediate intervalley scattering, restricting scattering to phonon absorption processes.

We observe that the energy loss in the on-shell 2ph case is noticeably higher between 300 meV and 340 meV. Above 340 meV, the difference between the two cases is smaller due to the 2ph rates in the L valley becoming less significant in comparison to the 1ph rates, as discussed for Fig. 4.6b. The reason for the less negative energy loss near the L valley minimum is the same as in the Γ valley; namely, the 1e1a processes are nearly elastic, causing the average energy loss to be less negative.

4.8 PSD at high electric fields: Hot electron noise

The PSD is sensitive to the strength of intervalley scattering processes [114, 220], and hence a stricter test of the present level of theory can be obtained by computing the PSD of the hot electrons. The normalized hot electron PSD versus electric field along with experimental measurements from the literature is given in Fig. 4.9. The experimental PSD exhibits a characteristic non-monotonic trend of an initial decrease, followed by a marked increase around the onset of negative differential mobility and a subsequent decrease. The data have been obtained by various methods including time of flight [256] for the diffusion coefficient and direct measurements of noise power [217, 271]. The time of flight results of Ref. [256] are suggested to overestimate the magnitude of the peak [272], but despite scatter in the data and the possibility of experimental inaccuracies the same qualitative trend has been reproduced in several studies.

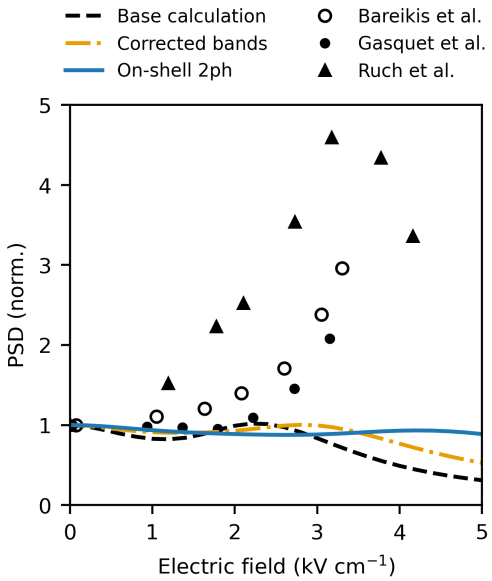

Figure 4.9: PSD versus electric field for the three cases as described in the text. None of the calculated cases are able to reproduce the peak in the PSD near 3 kV cm^{-1} that appears in the experimental data: PSD from noise temperature and differential mobility measurements (filled circles [271] and open circles [217]), and from time of flight experiments (triangles [256]).

This trend has been attributed to the following factors. First, the PSD weakly decreases at low fields as carriers are heated to higher energies with higher scattering rates, leading to a decrease in mobility. As a result, the PSD also

decreases since the proportionality relation between mobility and PSD [102–104] is approximately satisfied at low fields. Near the threshold field for negative differential mobility, intervalley transitions become possible, and the peak in the PSD has been attributed to intervalley diffusion that arises due to scattering between two valleys of highly dissimilar effective masses [61, 107, 109]. Finally, the PSD decreases at high fields due to the accumulation of carriers in the L valley. The decrease occurs because the group velocities in the L valley are substantially lower than those in the Γ valley and hence make a lesser contribution to the electric current and PSD as indicated by the group velocity factor in the sum in Eq. 3.50.

The PSD from the base calculation predicts some features of the experimental non-monotonic trend, with the initial decrease at low field originating from the increase in scattering rates [250], followed by a weak peak and decrease above 2.5 kV/cm. However, overall the calculated PSD is in poor agreement with the experiments, with the rise in the PSD being significantly underestimated. In the corrected bands case, the initial decrease of the PSD versus field is weaker, consistent with the increased effective mass which inhibits electron heating, and the subsequent decrease of the PSD after the peak occurs at a larger field (3 kV/cm), consistent with the L valley minimum having been shifted to higher energies. However, little improvement in the magnitude of the PSD peak is observed.

Surprisingly, however, the inclusion of on-shell 2ph scattering does not yield improved agreement for the PSD, with the weak peak largely unchanged compared to either calculation at the 1ph level of theory. Further, in all three cases the onset of intervalley scattering by itself does not produce a peak in the PSD, suggesting that the precise details of how intervalley scattering mediates transitions between valleys are of high importance to producing this characteristic feature. Further discussion on this point is given in Sec. 4.10.

4.9 Resolving a discrepancy in the intervalley scattering strength

We have established that the on-shell 2ph level of theory yields improved agreement with experiment for the drift velocity compared to the 1ph level of theory but does not predict the trend of PSD in GaAs. We have also shown how the on-shell 2ph contributes substantially to intervalley scattering and qualitatively affects the evolution of the electron distribution function with

electric field, in particular by increasing the energy relaxation rate. We now discuss how these findings allow for the resolution of a discrepancy in the IDP inferred from different experiments [113], and we discuss the possible reasons for the lack of a peak in the PSD.

Interpretation of experimental studies of intervalley scattering

Intervalley scattering in GaAs has been the subject of intensive experimental and theoretical study owing to its importance to negative differential resistance and the Gunn effect. Many studies aimed to quantify the strength of intervalley scattering as measured by the IDP in the semi-empirical expression originally derived by Conwell [255]. While this model is now known to be inaccurate [124, 125], the IDP in the model nevertheless captures the magnitude of intervalley processes in a single number that is comparable across studies [273].

The IDP value in GaAs has been inferred primarily from two classes of experiments, charge transport and photoluminescence response to optical excitation. In transport studies, an external field was applied to a sample and the current or noise response was measured. The transport was simultaneously modeled with Monte Carlo methods based on semi-empirical scattering rates, and the IDP was obtained by fitting simulation and experiment. This approach has been used on samples subjected to uniaxial stress along the [111] crystal axis [117] to identify the shift in threshold field for onset of negative differential mobility with stress, with additional modeling performed in Ref. [118]; and measurements of the diffusion coefficient [256] with modeling in Ref. [114]. The value of the IDP extracted from these experiments is approximately $D \sim 2 \times 10^8$ eV/cm.

In the other class of experiments, the sample was subjected to optical excitation and the resulting photoluminescence was measured. Although the details vary between experiments, the electron lifetime below and above the L valley energy can be directly extracted from the measurements, thereby providing the intervalley scattering rate. This approach does not require assumptions regarding the physical origin of the scattering. This approach has been employed by Dymnikov et al., who measured the depolarization of photoluminescence in a magnetic field [274]; Karlik et al., who deduced a lifetime based on relative photoluminescence intensities [122]; and Fasol et al. using the broadening of the photoluminescence peak [275]. The value of the IDP from these methods

is generally around a factor of four larger than that inferred from transport studies. We show the differing values of IDP from both classes of experiments in Fig. 4.10. An extensive review of the discrepancy was given by Reklaitis et al. [113], and it remains unresolved.

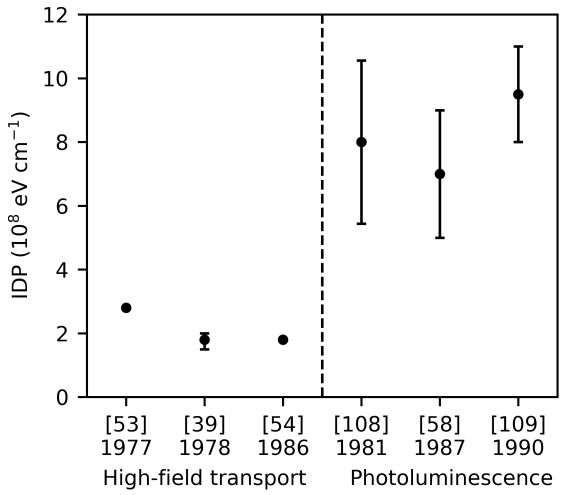

Figure 4.10: Intervalley deformation potential (IDP) values inferred from high-field transport and photoluminescence experiments. The high-field transport experiments require modeling to fit the data [114, 117, 118]. The photoluminescence experiments extract a lifetime that is used to deduce the IDP [122, 274, 275]. A clear discrepancy exists in the IDP inferred from the two sets of experiments.

Our observation that on-shell 2ph scattering has a marked effect on the high-field transport properties in GaAs provides a means to reconcile the differing conclusions. An important difference between the two types of experiments is that determining the intervalley scattering strength from transport experiments requires interpretation using simulations, while the optical experiments directly provide a lifetime. The IDP values inferred from transport experiments are therefore susceptible to inaccuracies in the assumed scattering rates. We have shown in Fig. 4.7b that the inclusion of 2ph scattering qualitatively changes the steady-state distribution function at high fields due to contributions to momentum as well as energy relaxation (Fig. 4.8b and 4.8d). Specifically, the 1ph level of theory underpredicts the energy relaxation and hence overpredicts the population at high energies, leading to an overprediction of

the L valley population and hence a suppression of the PSD peak. In the MC simulations used to interpret the experiments, a lesser value of the IDP would therefore be needed to compensate, explaining the smaller value inferred from transport studies. Even if the 1ph scattering rates are increased in magnitude to achieve the same mobility from the 2ph calculation, we find that the energy relaxation remains underpredicted and the artificially large heating at the 1ph level of theory remains. Further, based on the semi-empirical expressions for the 1ph rates used in MC studies, the magnitude of the 1ph rates required to prevent the overpopulation at high energies would lead to a substantial underprediction of the low-field mobility.

We therefore conclude that the correct intervalley scattering rates are those inferred from optical studies, resolving the discrepancy regarding the strength of intervalley scattering in GaAs as described in Ref. [113]. Our work also provides a clear physical origin for the underprediction of the IDP from transport studies.

4.10 Possible origin for lack of PSD peak

Finally, we consider possible origins of the discrepancy in the PSD versus electric field. Recall that the non-monotonic trend of the PSD in GaAs can be separated into three regimes: an initial decrease due to carriers experiencing larger scattering rates, a peak attributed to "intervalley diffusion," and a subsequent decrease due to accumulation of carriers in the L valley [61]. In prior MC studies, the intervalley scattering was described by a single parameter, the IDP, which was obtained by fitting the simulated and experimental PSD, thus providing a means to reproduce the experimental trend even if the intervalley processes responsible for the trend are missing or inaccurately described.

Fitting 1ph results to get PSD peak

In fact, we find that we can reproduce the PSD peak if alter the 1ph scattering rates in an ad hoc way that is comparable to the artificially small IDP fitted from experiments. This fitting requires using the model band structure, increasing the strength of LO phonon scattering by 50%, and also reducing the strength of all 1ph intervalley scattering by a factor of 5. The resulting PSD increases dramatically at intermediate fields while the drift velocity remains qualitatively similar. We show this result in Fig. 4.11 where the curves corresponding to modifications described above are denoted "Fitted 1ph."

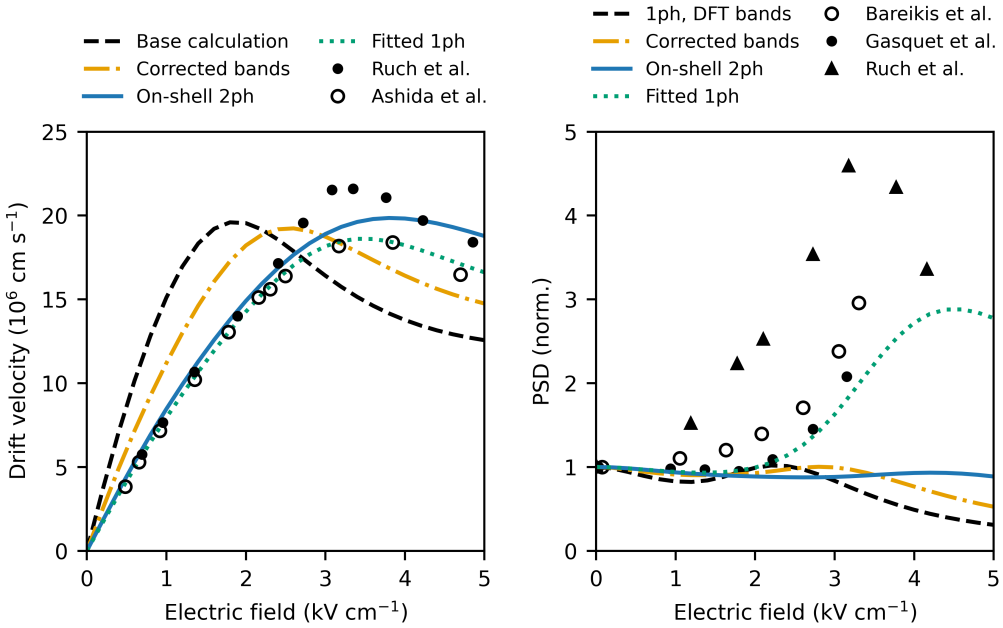

Figure 4.11: Drift velocity and PSD with parameterized 1ph rates. The "Fitted 1ph" curve uses a model band structure, and with all intervalley scattering rates reduced by a factor of 5. The fitted 1ph curve has a much larger PSD peak, but represents the unphysical nature of parameterized models.

The interpretation here is that reducing intervalley scattering not only slows the accumulation of electrons in the L-valley, but also significantly reduces the scattering experienced by the fluctuations themselves. As we discussed in Sec. 4.1, the PSD is suppressed as scattering rates increase, so a lower intervalley scattering rate means there is less suppression of fluctuations, especially at the high energy states where intervalley scattering can occur. This leads to an increase in the PSD. However, the arbitrary increase of the LO phonon scattering rates by 50% could only be justified using our post-hoc knowledge of the strength of 2ph scattering rates. And further, we know that a five-fold reduction in 1ph scattering rates, exclusive only to intervalley processes, is unphysical as there is no reason to doubt such a large deviation of the e-ph scattering rates calculated from first principles. Thus we see how a parameterized model can lead to an incorrect physical interpretation.

Missing 2ph processes

What the above analysis shows is that predicting the experimentally observed PSD trend requires correctly describing not only the overall scattering rate magnitude but also incorporating the correct couplings between electronic states, since the energies of the initial and final states involved in the process correspond to the location of the off-diagonal elements of the collision matrix. In the Γ valley, these off-diagonal elements determine the energy relaxation rate which in turn affects the electron population capable of undergoing intervalley scattering. For Γ-L scattering, these elements determine the the steady-state population in the L valley but also the specific states that undergo intervalley transitions. Intervalley transitions at higher energies may increase the PSD owing to the larger difference between their group velocities and the drift velocity as in Eqn. 3.48. Therefore, all relevant scattering processes must be present to achieve the correct steady-state distribution as well as the correct scattering rates experienced by the fluctuations about that steady state if the PSD is to be accurately predicted.

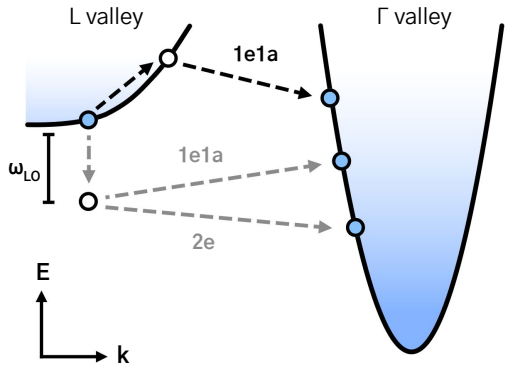

Figure 4.12: Schematic of on-shell 2ph processes and missing off-shell intervalley processes in the L valley of GaAs. The open circles correspond to the intermediate virtual state. The black arrows correspond to an on-shell 2ph process which are included in our calculation since the intermediate virtual state is close to the band energy. We show a 1e1a process, which is the predominant type of 2ph scattering in the L valley. The gray arrows show representative off-shell processes that are not included in the present calculation. Both an off-shell 1e1a and off-shell 2e process are shown, beginning with the emission of an LO phonon which has a large e-ph matrix element due to the Frohlich interaction. We suggest that missing off-shell processes like the ones shown may be necessary to predict the peak in PSD.

We suggest that the missing scattering processes that are necessary for the PSD peak are off-shell 2ph transitions. The processes that mediate intervalley transfers at energies exceeding the L valley minimum are one example of such missing processes. We schematically illustrate some of these missing processes alongside the included on-shell processes in Fig. 4.12. As an example, a 2ph intervalley transition from the L valley minimum to the Γ valley could be achieved by the emission of a zone-center LO phonon, with a large e-ph matrix element due to the Frohlich interaction, followed by emission or absorption of an acoustic intervalley phonon. The 1e1a process in particular would yield a transition at high energies that could lead to an increase in PSD. Another location where the missing off-shell 2ph processes could change the trends is at low electron energy. We can see in Fig. 4.6 that our on-shell rates are lower than the full calculation of Ref. [98], and in particular are missing the double "step" feature in the full calculation, which was attributed to the 1e1a rates increasing as the intermediate state starts to include more on-shell processes. Such an energy dependence is not possible in our calculation, and indeed we see in Fig. 4.8 that the on-shell 1e1a rates lack the non-monotonic trend. The energy dependence of the 2ph rates at low energies may play a significant role in the trends versus electric field. Still, including off-shell 2ph processes remains a formidable computational task and is the subject of future work.

4.11 Summary

The primary numerical tools used to study electronic noise have been Monte Carlo (MC) methods [231, 264, 276–278]. These simulators have many advantages, including the ability to incorporate realistic device geometries and space charge effects through coupled Poisson solvers, and they are thus useful to interpret experimental measurements on devices. However, MC studies rely upon semi-empirical models of scattering and electronic structure that require parameters such as deformation potentials, sound velocities, effective masses, and energy gaps to be specified and calibrated against experiment. The methods are thus most useful for well-characterized materials for which these empirical models are available.

The development of ab initio methods to study transport phenomena without adjustable parameters enable an understanding of the microscopic scattering processes that underlie macroscopic properties and permit the prediction of

new materials. However, thus far these methods have been restricted to the low-field, cold electron regime.

In our work, we have described an ab initio theory of electronic noise and high-field transport in semiconductors, and applied the method to GaAs. The method requires no adjustable parameters, with the phonon dispersion, band structure, and electron-phonon coupling calculated from first-principles. We have demonstrated the ability of the method to show disparate timescales of energy and momentum relaxation, as well as the frequency dependence of the PSD. Although the 1ph theory has been thought to be adequate for GaAs and used extensively in Monte Carlo simulations, we have found that on-shell 2ph processes play a fundamental role in all aspects of high-field transport, including energy relaxation and intervalley scattering. This finding resolves a long-standing discrepancy regarding the value of the IDP as inferred from transport and optical studies in favor of the stronger value obtained from photoluminescence measurements. Further, the characteristic peak in the PSD versus electric field is not predicted at this level of theory. We suggest that off-shell 2ph intervalley scattering processes may be required to observe this feature. Our work demonstrates that the ab initio computation of high-field transport and noise properties may provide considerable insight into the e-ph interaction in semiconductors.

Chapter 5

SUMMARY AND FUTURE WORK

The unifying theme of this thesis has been the study of transport phenomena using the Boltzmann transport equation with ab initio inputs. As discussed in Ch. 1, the main complication in the BTE is the formulation of the collision integral, and including the proper form of the interactions in the collision integral is necessary to achieve experimental agreement. Approximate forms of scattering can lead to qualitatively different results and thus the ab initio approach provides a way to rigorously assess the importance of various mechanisms on the transport properties without the ambiguity of adjustable parameters. Furthermore, a first-principles formulation of the BTE requires calculation of phonon and electron properties throughout the Brillouin zone instead of using some average quantity, permitting an analysis of which phonon or electron states contribute most substantially to transport and the reasons for their contribution.

In the realm of thermal transport (Ch. 2), we studied the intrinsic upper limits of thermal conductivity using unsubstituted polythiophene as an example of a complex polymer crystal with high uniaxial thermal conductivity. We found that despite the short phonon lifetimes of many modes, an extreme degree of phonon focusing results in a large total contribution to phonon conductivity when summing over the entire Brillouin zone, a result we show would have been difficult to predict based on heuristic analysis of average group velocities and average lifetimes. We showed that the isoenergy contours for branches where there is a much stronger anisotropy have almost complete focusing in the chain axis, which allowed even optical modes at high frequency to contribute non-negligibly to thermal transport. In a fictitious isotropic version of PT with no phonon focusing, the thermal conductivity would be over 80% lower. To further validate the importance of the phonon focusing mechanism, we performed the same calculation in the high-pressure phase of PTFE and found a similar result, with the thermal conductivity in this high-pressure phase over 3 orders of magnitude larger than in the ambient pressure phase. In both PT and PTFE, further aligning the group velocity along the chain axis only

increased the thermal conductivities by less than 10%, indicating that in both materials, the degree of phonon focusing is close to maximal.

We then used the BTE to study charge transport and fluctuations at high electric fields. In Ch. 3, we gave an overview of the typical approach for solving the BTE at low fields and the required theoretical and numerical techniques to overcome the typical low-field approximations. The two main advances were the inclusion of the reciprocal space gradient on the deviational occupation and the analysis of the non-linearities in the collision integral that allowed us to make the physically justified approximation of neglecting all electron occupations when compared to phonon occupations. Together, these two modifications yielded a steady-state BTE for high electric fields that we solved directly as a linear system. Next, we described the theory used to describe the behavior of fluctuations at high fields characterized by the current power spectral density and also called hot electron noise. Two important facts established the BTE approach to hot electron noise: first, that the current PSD is the Fourier transform of the current autocorrelation due to the Wiener-Khintchine theorem, and second, the current autocorrelation itself obeys the BTE. From there, we showed that a rearrangement of the order of summation allowed for a direct computation of the PSD through a Fourier transformed BTE whose solution is an effective distribution function that is summed over the Brillouin zone with velocity to give the PSD. We also included two phonon scattering, and made approximations to permit the calculation of this higher-order e-ph scattering process for the large number of electronic states at high energies. We calculated only processes that were within some energy tolerance of being on-shell.

We discussed the results of applying this theoretical and numerical framework to GaAs in Ch. 4. We analyzed results in the warm electron regime first, showing that the slope of the PSD versus field at moderate electric fields indicates the balance of increasing scattering rates against the heating of the electrons to higher energies, and that semi-empirical models failed to predict the right trend. We showed that the frequency dependence and anisotropy of the PSD revealed the timescales of energy and momentum relaxation. We analyzed these relaxation timescales by calculating the fractional energy and momentum loss from individual scattering processes, weighted by the steady state distribution function, to show that in the warm electron regime the scattering

can be considered quasi-elastic. In the hot electron regime, we showed that the inclusion of 2ph scattering was essential for achieving the best agreement with the drift velocity curve. Two-phonon scattering also qualitatively changed the nature of energy relaxation and intervalley scattering in GaAs, which explains a discrepancy in the literature regarding the strength of intervalley scattering, as 1ph scattering leads to excessive heating of the electrons. We showed that even with 2ph scattering, the increase of the PSD is not reproduced which we attribute to the lack of off-shell intervalley 2ph processes. Our study indicates the importance of achieving not just the correct scattering rates, but also the correct energies of the final states reached after scattering, showing how the behavior of fluctuations provides a new observable against which ab initio methods can be measured.

5.1 Future work

We discuss some new directions of investigation suggested by our findings.

Phonon lifetimes between polymer crystals

In our study of polymer thermal transport, we showed that PT indeed has much lower phonon lifetimes than a simple crystal like Si, but we did not discuss the difference in lifetimes *between* various polymers. Analyzing the difference between the scattering rates of different polymers may yield additional insights. For example, it has been shown that flexural phonons are the dominant contributor to thermal conductivity in graphene due, in part, to a symmetry based selection rule involving the reflection symmetry of graphene that reduces anharmonic scattering [180, 279]. The polythiophene rings in each polymer chain are also planar like graphene, and while the symmetry of the PT crystal is of course different from graphene, the flexural modes of the PT chains may also obey certain selection rules that eliminate certain anharmonic interactions and thus enhance the phonon lifetime compared to other polymers. This may explain how PT has a higher thermal conductivity than PE, despite a more complicated unit cell.

Hot electron noise in other semiconductor materials

The BTE framework for the ab initio computation of electronic noise and high field transport described in Ch. 3 may be applied to other materials where the approximation of negligible electron occupations is valid. Another

semiconductor similar to GaAs is InP which also has a direct gap and exhibits negative differential resistance. However, its satellite valleys have a larger energy separation from the conduction band minimum, meaning the onset of intervalley processes occurs at higher electric fields compared to GaAs [99], producing different trends of noise versus electric field. If two phonon processes are not significant in InP and the ab initio calculation of hot electron noise at the 1ph level yields reasonable agreement with experimental data, the results may provide additional insight into the influence of intervalley scattering on the behavior of fluctuations, since the analysis in GaAs is hampered by missing 2ph processes and a lack of experimental agreement.

Inclusion of off-shell two-phonon processes in GaAs

As we have already discussed, only on-shell 2ph processes were included in our calculation for GaAs due to computational limitations, but the off-shell 2ph processes may be vital for reproducing the experimental trend of PSD. The off-shell 2ph processes necessary for reproducing the experimental trends might be made computationally tractable by employing by different approximations that more accurately capture the 2ph scattering present in GaAs. For example, instead of calculating all off-shell processes, it may be the case that 1e1a or 2e processes dominate the intervalley scattering processes we are interested in studying so that 2a processes can be neglected. A large source of computational cost comes from the ab initio calculation of the e-ph matrix elements entering into the 2ph process amplitude of Eq. 3.53. Although ab initio matrix elements are known to differ from those of simple physical models, employing semi-empirical expressions like those for the acoustic deformation potential, and polar optical phonon scattering [1], may reduce the computational burden enough to determine which 2ph scattering channels are most responsible for the experimental trends.

More interactions for electrons from first principles

Our framework for high-field transport and hot electron noise has treated only electron-phonon scattering, but there are other interactions that can scatter electrons and would alter the trends versus electric field. Our calculation in GaAs was performed at room temperature for low carrier concentrations precisely to avoid these other interactions, but transport at low temperatures and higher carrier concentrations involves electron-impurity scattering. Semi-

conductors are typically doped by introducing impurities that are ionized to provide free carriers, but these ionized impurities can scatter electrons, and an ab initio description of both neutral and charged impurities has only recently been developed [280, 281]. The ab initio study of high-field transport and hot electron noise at low temperatures where both impurity and e-ph scattering are present may reveal new dynamics when compared to prior Monte Carlo studies of the same phenomena.

Electron-electron interactions are also important at higher carrier concentrations, and become especially relevant at electric fields even higher than those studied here, on the order of 10^5 V cm^{-1}in GaAs [282], as the carriers are heated to energies above the band minimum that are greater than the band gap and impact ionization can occur. One way the impact ionization rate can be calculated is through the imaginary part of the self energy of a *GW* calculation [283, 284]. For hot electron noise however, electron-electron interactions introduce additional correlations between fluctuations (c.f. Ch. 2 of Ref. [245]) which requires modification of the equations of Ch. 3 and thus additional theory development. At high carrier concentrations, the interaction of electrons with plasmons or coupled plasmon-phonon modes [285] also become important. In general, electron-electron interactions are a many-body physics problem [286] that are the focus of much contemporary solid state research, and their inclusion requires careful treatment within the quasiparticle Boltzmann framework.

Non-equilibrium phonon occupations

The framework presented in Ch. 3 for hot electron noise assumes equilibrium occupations of phonons given by the lattice temperature, which is valid when the phonon-phonon (ph-ph) scattering rate is large enough such that the energy from the electrons is dissipated on a timescale much shorter than the electron-phonon scattering rate. When this does not occur, it can lead to non-equilibrium phonon populations that qualitatively alter the scattering in the electron and phonon systems, and one may be required to consider not just the e-ph and the ph-ph interaction but also the scattering of phonons by electrons (ph-e). This is a well known phenomena for electrons driven by photoexcitation in semiconductors [287], and non-thermal phonon populations have also been observed in graphene [288] and aluminum [289]. For relaxation of photoexcited carriers without an applied field, recent efforts have been made to

develop ab initio descriptions beyond the standard two-temperature model by coupling the phonon and electron BTEs with an energy transfer rate [290], or through direct coupling of the state occupations [291]. For transport under the presence of an electric field or temperature gradient, the non-equilibrium populations of electrons and phonons can lead to a mutual "drag" which affects the transport coefficients, and the first-principles framework for calculating these phenomena has been recently established [93].

At low temperatures, the phonon-phonon scattering rate is lower since phonon occupations are smaller; at high electric fields, the energy dissipated by electrons is also higher, so the equilibrium assumption for phonons may not be valid. In fact, prior Monte Carlo studies have analyzed the effect of non-equilibrium phonons on the noise behavior in GaAs at 77 K, and found a non-negligible effect [292, 293]. In the same spirit of this work, a fully ab initio calculation of noise and transport trends versus electric field with coupled phonon and electron systems may provide new insights when compared to both the prior models and the experimental results.

BIBLIOGRAPHY

[1] G.D. Mahan. *Condensed Matter in a Nutshell*. Princeton University Press, Princeton, 2011.

[2] Charles Kittel. *Introduction to Solid State Physics*. Wiley, 8 edition, 2004.

[3] R. Peierls. Zur kinetischen theorie der wärmeleitung in kristallen. *Annalen der Physik*, 395(8):1055–1101, 1929.

[4] Joseph Callaway. Model for lattice thermal conductivity at low temperatures. *Phys. Rev.*, 113:1046–1051, Feb 1959.

[5] P. G. Klemens. *Thermal Conductivity of Solids at Low Temperatures*, pages 198–281. Springer Berlin Heidelberg, Berlin, Heidelberg, 1956.

[6] G. A. Slack. Nonmetallic crystals with high thermal conductivity. *Journal of Physics and Chemistry of Solids*, 34(2):321–335, January 1973.

[7] Felix Bloch. Über die quantenmechanik der elektronen in kristallgittern. *Zeitschrift für Physik*, 52(7):555–600, Jul 1929.

[8] J. Bardeen and W. Shockley. Deformation potentials and mobilities in non-polar crystals. *Phys. Rev.*, 80:72–80, Oct 1950.

[9] Conyers Herring and Erich Vogt. Transport and deformation-potential theory for many-valley semiconductors with anisotropic scattering. *Phys. Rev.*, 101:944–961, Feb 1956.

[10] James C. Phillips and Leonard Kleinman. New method for calculating wave functions in crystals and molecules. *Phys. Rev.*, 116:287–294, Oct 1959.

[11] L.J. Sham and J.M. Ziman. The electron-phonon interaction. volume 15 of *Solid State Physics*, pages 221–298. Academic Press, 1963.

[12] Walter Kohn and Lu Jeu Sham. Self-consistent equations including exchange and correlation effects. *Physical review*, 140(4A):A1133, 1965.

[13] S.K. Joshi and A.K. Rajagopal. Lattice dynamics of metals. volume 22 of *Solid State Physics*, pages 159–312. Academic Press, 1969.

[14] Hans Hellmann et al. Einfuhrung in die quantenchemie. 1937.

[15] R. P. Feynman. Forces in molecules. *Phys. Rev.*, 56:340–343, Aug 1939.

[16] H. Wendel and Richard M. Martin. Theory of structural properties of covalent semiconductors. *Phys. Rev. B*, 19:5251–5264, May 1979.

[17] K. Kunc and Richard M. Martin. Ab initio force constants of gaas: A new approach to calculation of phonons and dielectric properties. *Phys. Rev. Lett.*, 48:406–409, Feb 1982.

[18] Stefano Baroni, Paolo Giannozzi, and Andrea Testa. Green's-function approach to linear response in solids. *Phys. Rev. Lett.*, 58:1861–1864, May 1987.

[19] L. Lindsay, D. A. Broido, and T. L. Reinecke. First-Principles Determination of Ultrahigh Thermal Conductivity of Boron Arsenide: A Competitor for Diamond? *Physical Review Letters*, 111(2):025901, July 2013.

[20] Joon Sang Kang, Man Li, Huan Wu, Huuduy Nguyen, and Yongjie Hu. Experimental observation of high thermal conductivity in boron arsenide. *Science*, 361(6402):575–578, 2018. https://science.sciencemag.org/content/361/6402/575.

[21] Sheng Li, Qiye Zheng, Yinchuan Lv, Xiaoyuan Liu, Xiqu Wang, Pinshane Y. Huang, David G. Cahill, and Bing Lv. High thermal conductivity in cubic boron arsenide crystals. *Science*, 361(6402):579–581, 2018. https://science.sciencemag.org/content/361/6402/579.

[22] Tianli Feng, Lucas Lindsay, and Xiulin Ruan. Four-phonon scattering significantly reduces intrinsic thermal conductivity of solids. *Phys. Rev. B*, 96:161201, Oct 2017.

[23] Carlo Cercignani. *The Boltzmann Equation and Its Applications*. Springer New York, New York, NY, 1988.

[24] G. Chen. *Nanoscale Energy Transport and Conversion: A Parallel Treatment of Electrons, Molecules, Phonons, and Photons*. MIT-Pappalardo series in mechanical engineering. Oxford University Press, 2005.

[25] C. L. Choy. Thermal conductivity of polymers. *Polymer*, 18(10):984–1004, October 1977.

[26] C.L Choy, W.H Luk, and F.C Chen. Thermal conductivity of highly oriented polyethylene. *Polymer*, 19(2):155 – 162, 1978.

[27] C. L. Choy, F. C. Chen, and W. H. Luk. Thermal conductivity of oriented crystalline polymers. *Journal of Polymer Science: Polymer Physics Edition*, 18(6):1187–1207.

[28] Sheng Shen, Asegun Henry, Jonathan Tong, Ruiting Zheng, and Gang Chen. Polyethylene nanofibres with very high thermal conductivities. *Nat. Nano.*, 5(4):251, 2010.

[29] G. Jeffrey Snyder and Eric S. Toberer. Complex thermoelectric materials. *Nature Materials*, 7(2):105–114, February 2008.

[30] M. Pietralla. High thermal conductivity of polymers: Possibility or dream? *Journal of Computer-Aided Materials Design*, 3(1):273–280, August 1996.

[31] M. J. P. Musgrave and Edward Crisp Bullard. On the propagation of elastic waves in aeolotropic media i. general principles. *Proceedings of the Royal Society of London. Series A. Mathematical and Physical Sciences*, 226(1166):339–355, 1954.

[32] B. Taylor, H. J. Maris, and C. Elbaum. Phonon focusing in solids. *Phys. Rev. Lett.*, 23:416–419, Aug 1969.

[33] B. Taylor, H. J. Maris, and C. Elbaum. Focusing of Phonons in Crystalline Solids due to Elastic Anisotropy. *Physical Review B*, 3(4):1462–1472, February 1971.

[34] M. Pietralla, R. M. Weeger, and D. B. Mergenthaler. The role of phonon focussing and structure scattering in oriented semicrystalline polymers. *Zeitschrift für Physik B Condensed Matter*, 77(2):219–228, June 1989.

[35] Z. Chen, Z. Wei, Y. Chen, and C. Dames. Anisotropic Debye model for the thermal boundary conductance. *Physical Review B*, 87(12):125426, March 2013.

[36] Jun Liu and Ronggui Yang. Tuning the thermal conductivity of polymers with mechanical strains. *Phys. Rev. B*, 81:174122, 2010.

[37] Tengfei Luo, Keivan Esfarjani, Junichiro Shiomi, Asegun Henry, and Gang Chen. Molecular dynamics simulation of thermal energy transport in polydimethylsiloxane. *J. Appl. Phys.*, 109(7):074321, 2011.

[38] Hao Ma and Zhiting Tian. Effects of polymer topology and morphology on thermal transport: A molecular dynamics study of bottlebrush polymers. *Applied Physics Letters*, 110(9):091903, 2017.

[39] Teng Zhang, Xufei Wu, and Tengfei Luo. Polymer nanofibers with outstanding thermal conductivity and thermal stability: Fundamental linkage between molecular characteristics and macroscopic thermal properties. *The Journal of Physical Chemistry C*, 118(36):21148–21159, 2014.

[40] Boris Ni, Taku Watanabe, and Simon R Phillpot. Thermal transport in polyethylene and at polyethylene-diamond interfaces investigated using molecular dynamics simulation. *J. Phys. Condens. Matter*, 21(8):084219, 2009.

[41] Asegun Henry and Gang Chen. High Thermal Conductivity of Single Polyethylene Chains Using Molecular Dynamics Simulations. *Physical Review Letters*, 101(23):235502, December 2008.

[42] D. A. Broido, M. Malorny, G. Birner, Natalio Mingo, and D. A. Stewart. Intrinsic lattice thermal conductivity of semiconductors from first principles. *Appl. Phys. Lett.*, 91(23):231922, 2007.

[43]

[44] Qian Zhang, Chenhan Liu, Xue Liu, Jinyu Liu, Zhiguang Cui, Yin Zhang, Lin Yang, Yang Zhao, Terry T. Xu, Yunfei Chen, Jiang Wei, Zhiqiang Mao, and Deyu Li. Thermal Transport in Quasi-1d van der Waals Crystal Ta2pd3se8 Nanowires: Size and Length Dependence. *ACS Nano*, 12(3):2634–2642, March 2018.

[45] Tribhuwan Pandey, Carlos A. Polanco, Valentino R. Cooper, David S. Parker, and Lucas Lindsay. Symmetry-driven phonon chirality and transport in one-dimensional and bulk Ba_3N-derived materials. *Phys. Rev. B*, 98:241405, Dec 2018.

[46] Xinjiang Wang, Massoud Kaviany, and Baoling Huang. Phonon coupling and transport in individual polyethylene chains: a comparison study with the bulk crystal. *Nanoscale*, 9(45):18022–18031, November 2017.

[47] Jin-Wu Jiang, Junhua Zhao, Kun Zhou, and Timon Rabczuk. Superior thermal conductivity and extremely high mechanical strength in polyethylene chains from ab initio calculation. *Journal of Applied Physics*, 111(12):124304, 2012.

[48] Keishu Utimula, Tom Ichibha, Ryo Maezono, and Kenta Hongo. Ab initio search of polymer crystals with high thermal conductivity. *Chemistry of Materials*, 31(13):4649–4656, 2019.

[49] Nina Shulumba, Olle Hellman, and Austin J. Minnich. Lattice Thermal Conductivity of Polyethylene Molecular Crystals from First-Principles Including Nuclear Quantum Effects. *Physical Review Letters*, 119(18):185901, October 2017.

[50] Olle Hellman and I. A. Abrikosov. Temperature-dependent effective third-order interatomic force constants from first principles. *Phys. Rev. B*, 88(14):144301, 2013.

[51] Nina Shulumba, Olle Hellman, and Austin J. Minnich. Intrinsic localized mode and low thermal conductivity of PbSe. *Phys. Rev. B*, 95(1):014302, 2017.

[52] O. Hellman, I. A. Abrikosov, and S. I. Simak. Lattice dynamics of anharmonic solids from first principles. *Phys. Rev. B*, 84(18):180301, 2011.

[53] Olle Hellman and David A. Broido. Phonon thermal transport in Bi2te3 from first principles. *Phys. Rev. B*, 90(13):134309, 2014.

[54] A. H. Romero, E. K. U. Gross, M. J. Verstraete, and Olle Hellman. Thermal conductivity in PbTe from first principles. *Phys. Rev. B*, 91(21):214310, 2015.

[55] Yanfei Xu, Xiaoxue Wang, Jiawei Zhou, Bai Song, Zhang Jiang, Elizabeth M. Y. Lee, Samuel Huberman, Karen K. Gleason, and Gang Chen. Molecular engineered conjugated polymer with high thermal conductivity. *Science Advances*, 4(3), 2018.

[56] Miguel MuñozRojo, Jaime Martín, Stéphane Grauby, Theodorian Borca-Tasciuc, Stefan Dilhaire, and Marisol Martin-Gonzalez. Decrease in thermal conductivity in polymeric P3ht nanowires by size-reduction induced by crystal orientation: new approaches towards thermal transport engineering of organic materials. *Nanoscale*, 6(14):7858–7865, 2014.

[57] Boris Russ, Anne Glaudell, Jeffrey J. Urban, Michael L. Chabinyc, and Rachel A. Segalman. Organic thermoelectric materials for energy harvesting and temperature control. *Nature Reviews Materials*, 1(10):16050, October 2016.

[58] Virendra Singh, Thomas L Bougher, Annie Weathers, Ye Cai, Kedong Bi, Michael T Pettes, Sally A McMenamin, Wei Lv, Daniel P Resler, Todd R Gattuso, David H Altman, Kenneth H Sandhage, Li Shi, Asegun Henry, and Baratunde A Cola. High thermal conductivity of chain-oriented amorphous polythiophene. *Nat. Nano.*, 9(5):384, 2014.

[59] *Transferred-Electron and Real-Space-Transfer Devices*, pages 510–547. John Wiley & Sons, Ltd, 2006.

[60] J.W. Ziman. *Electrons and Phonons: The Theory of Transport Phenomena in Solids*. Oxford University Press, Oxford, 1960.

[61] Carlo Jacoboni. *Nonlinear Transport*, pages 219–236. Springer Berlin Heidelberg, Berlin, Heidelberg, 2010.

[62] D.K. Ferry. *Semiconductor Transport*. CRC Press, London, 2000.

[63] E. J. Ryder and W. Shockley. Mobilities of electrons in high electric fields. *Phys. Rev.*, 81:139–140, Jan 1951.

[64] E. J. Ryder. Mobility of holes and electrons in high electric fields. *Phys. Rev.*, 90:766–769, Jun 1953.

[65] W. Shockley. Hot electrons in germanium and ohm's law. *Bell System Technical Journal*, 30(4):990–1034, 1951.

[66] J.B. Gunn. Microwave oscillations of current in iii–v semiconductors. *Solid State Communications*, 1(4):88–91, 1963.

[67] B K Ridley. Specific negative resistance in solids. *Proceedings of the Physical Society*, 82(6):954–966, dec 1963.

[68] Carlo Jacoboni and Lino Reggiani. The monte carlo method for the solution of charge transport in semiconductors with applications to covalent materials. *Rev. Mod. Phys.*, 55:645–705, Jul 1983.

[69] Feliciano Giustino. Electron-phonon interactions from first principles. *Rev. Mod. Phys.*, 89:015003, Feb 2017.

[70] M. Bernardi. First-principles dynamics of electrons and phonons. *European Physical Journal B*, 89(239), 2016.

[71] Samuel Poncé, Wenbin Li, Sven Reichardt, and Feliciano Giustino. First-principles calculations of charge carrier mobility and conductivity in bulk semiconductors and two-dimensional materials. *Reports on Progress in Physics*, 83(3):036501, feb 2020.

[72] O. D. Restrepo, K. Varga, and S. T. Pantelides. First-principles calculations of electron mobilities in silicon: Phonon and coulomb scattering. *Applied Physics Letters*, 94(21):212103, 2009.

[73] Wu Li. Electrical transport limited by electron-phonon coupling from boltzmann transport equation: An ab initio study of si, al, and mos_2. *Phys. Rev. B*, 92:075405, Aug 2015. https://link.aps.org/doi/10.1103/PhysRevB.92.075405.

[74] Mattia Fiorentini and Nicola Bonini. Thermoelectric coefficients of n-doped silicon from first principles via the solution of the boltzmann transport equation. *Phys. Rev. B*, 94:085204, Aug 2016. https://link.aps.org/doi/10.1103/PhysRevB.94.085204.

[75] Samuel Poncé, Elena R. Margine, and Feliciano Giustino. Towards predictive many-body calculations of phonon-limited carrier mobilities in semiconductors. *Phys. Rev. B*, 97:121201, Mar 2018.

[76] Samuel Poncé, Debdeep Jena, and Feliciano Giustino. Route to high hole mobility in gan via reversal of crystal-field splitting. *Phys. Rev. Lett.*, 123:096602, Aug 2019.

[77] Jin-Jian Zhou and Marco Bernardi. Ab initio electron mobility and polar phonon scattering in gaas. *Phys. Rev. B*, 94:201201, Nov 2016.

[78] Te-Huan Liu, Jiawei Zhou, Bolin Liao, David J. Singh, and Gang Chen. First-principles mode-by-mode analysis for electron-phonon scattering channels and mean free path spectra in gaas. *Phys. Rev. B*, 95:075206, Feb 2017.

[79] Carlo Motta, Fedwa El-Mellouhi, and Stefano Sanvito. Charge carrier mobility in hybrid halide perovskites. *Scientific Reports*, 5(1):12746, Aug 2015.

[80] Tianqi Zhao, Wen Shi, Jinyang Xi, Dong Wang, and Zhigang Shuai. Intrinsic and extrinsic charge transport in ch3nh3pbi3 perovskites predicted from first-principles. *Scientific Reports*, 6(1):19968, Jan 2016.

[81] K. M. Borysenko, J. T. Mullen, E. A. Barry, S. Paul, Y. G. Semenov, J. M. Zavada, M. Buongiorno Nardelli, and K. W. Kim. First-principles analysis of electron-phonon interactions in graphene. *Phys. Rev. B*, 81:121412, Mar 2010.

[82] Bolin Liao, Jiawei Zhou, Bo Qiu, Mildred S. Dresselhaus, and Gang Chen. Ab initio study of electron-phonon interaction in phosphorene. *Phys. Rev. B*, 91:235419, Jun 2015.

[83] Kristen Kaasbjerg, Kristian S. Thygesen, and Karsten W. Jacobsen. Phonon-limited mobility in n-type single-layer mos_2 from first principles. *Phys. Rev. B*, 85:115317, Mar 2012.

[84] Long Cheng, Chenmu Zhang, and Yuanyue Liu. Why two-dimensional semiconductors generally have low electron mobility. *Phys. Rev. Lett.*, 125:177701, Oct 2020.

[85] Samuel Poncé, Francesco Macheda, Elena Roxana Margine, Nicola Marzari, Nicola Bonini, and Feliciano Giustino. First-principles predictions of hall and drift mobilities in semiconductors. *Phys. Rev. Research*, 3:043022, Oct 2021.

[86] Te-Huan Liu, Bai Song, Laureen Meroueh, Zhiwei Ding, Qichen Song, Jiawei Zhou, Mingda Li, and Gang Chen. Simultaneously high electron and hole mobilities in cubic boron-v compounds: Bp, bas, and bsb. *Phys. Rev. B*, 98:081203, Aug 2018.

[87] Jin-Jian Zhou and Marco Bernardi. Predicting charge transport in the presence of polarons: The beyond-quasiparticle regime in $srtio_3$. *Phys. Rev. Research*, 1:033138, Dec 2019.

[88] Nien-En Lee, Hsiao-Yi Chen, Jin-Jian Zhou, and Marco Bernardi. Facile ab initio approach for self-localized polarons from canonical transformations. *Phys. Rev. Materials*, 5:063805, Jun 2021.

[89] Benjamin K. Chang, Jin-Jian Zhou, Nien-En Lee, and Marco Bernardi. Intermediate polaronic charge transport in organic crystals from a many-body first-principles approach, 2022.

[90] Zhenglu Li, Gabriel Antonius, Meng Wu, Felipe H. da Jornada, and Steven G. Louie. Electron-phonon coupling from ab initio linear-response theory within the *gw* method: Correlation-enhanced interactions and superconductivity in $ba_{1-x}k_xbio_3$. *Phys. Rev. Lett.*, 122:186402, May 2019.

[91] Guillaume Brunin, Henrique Pereira Coutada Miranda, Matteo Giantomassi, Miquel Royo, Massimiliano Stengel, Matthieu J. Verstraete, Xavier Gonze, Gian-Marco Rignanese, and Geoffroy Hautier. Electron-phonon beyond fröhlich: Dynamical quadrupoles in polar and covalent solids. *Phys. Rev. Lett.*, 125:136601, Sep 2020.

[92] Jinsoo Park, Jin-Jian Zhou, Vatsal A. Jhalani, Cyrus E. Dreyer, and Marco Bernardi. Long-range quadrupole electron-phonon interaction from first principles. *Phys. Rev. B*, 102:125203, Sep 2020.

[93] Nakib H. Protik and David A. Broido. Coupled transport of phonons and carriers in semiconductors: A case study of *n*-doped GaAs. *Phys. Rev. B*, 101:075202, Feb 2020.

[94] Dhruv C. Desai, Bahdan Zviazhynski, Jin-Jian Zhou, and Marco Bernardi. Magnetotransport in semiconductors and two-dimensional materials from first principles. *Phys. Rev. B*, 103:L161103, Apr 2021.

[95] Ivan Maliyov, Jinsoo Park, and Marco Bernardi. Ab initio electron dynamics in high electric fields: Accurate prediction of velocity-field curves. *Phys. Rev. B*, 104:L100303, Sep 2021.

[96] Krishnendu Ghosh and Uttam Singisetti. Ab initio velocity-field curves in monoclinic -ga2o3. *Journal of Applied Physics*, 122(3):035702, 2017.

[97] Jinlong Ma, Arun S. Nissimagoudar, and Wu Li. First-principles study of electron and hole mobilities of si and gaas. *Phys. Rev. B*, 97:045201, Jan 2018.

[98] Nien-En Lee, Jin-Jian Zhou, Hsiao-Yi Chen, and Marco Bernardi. Ab initio electron-two-phonon scattering in GaAs from next-to-leading order perturbation theory. *Nat. Comm.*, 11:1607, Mar 2020.

[99] H.L. Hartnagel, R. Katilius, and A. Matulionis. *Microwave Noise in Semiconductor Devices*. John Wiley & Sons, New York, 2001.

[100] V Bareikis and R Katilius. *Noise in Physical Systems and 1/f Fluctuations*. WORLD SCIENTIFIC, 1995. https://www.worldscientific.com/doi/abs/10.1142/2764.

[101] E. W. Bryerton, M. Morgan, and M. W. Pospieszalski. Ultra low noise cryogenic amplifiers for radio astronomy. In *2013 IEEE Radio and Wireless Symposium*, pages 358–360. IEEE, 2013. https://ieeexplore.ieee.org/document/6486740.

[102] Sh. Kogan. *Electronic Noise and Fluctuations in Solids*. Cambridge University Press, Cambridge, 1996.

[103] Herbert B. Callen and Richard F. Greene. On a theorem of irreversible thermodynamics. *Phys. Rev.*, 86:702–710, Jun 1952.

[104] H. Nyquist. Thermal agitation of electric charge in conductors. *Phys. Rev.*, 32:110–113, Jul 1928.

[105] P. Kleinert. Theory of hot-electron quantum diffusion in semiconductors. *Physics Reports*, 485(1):1–42, 2010.

[106] M.A. Leontovich. Fundamental equations of the kinetic theory of gases from the point of view of the theory of random processes. *Zh. Eksp. Teor. Fiz (JETP)*, 5(3-4), 1935.

[107] P. J. Price. Intervalley noise. *Journal of Applied Physics*, 31(6):949–953, 1960.

[108] S.V. Gantsevich, V.L. Gurevich, and R. Katilius. Fluctuations in semiconductors in a strong electric field and the scattering of light by "hot" electrons. *Soviet Physics JETP*, 22(4), 1970.

[109] W. Shockley, J.A. Copeland, and R.P. James. *Quantum Theory of Atoms*. Academic, New York, 1966.

[110] V. Bareikis, J. Liberis, I. Matulioniene, A. Matulionis, and P. Sakalas. Experiments on hot electron noise in semiconductor materials for high-speed devices. *IEEE Transactions on Electron Devices*, 41(11), 1994.

[111] J.-P. Nougier. Fluctuations and noise of hot carriers in semiconductor materials and devices. *IEEE Transactions on Electron Devices*, 41(11):2034–2049, 1994.

[112] Joseph L. Birman, Melvin Lax, and Rodney Loudon. Intervalley-scattering selection rules in iii-v semiconductors. *Phys. Rev.*, 145:620–622, May 1966.

[113] R Mickevicius and A Reklaitis. Electron intervalley scattering in gallium arsenide. 5(8):805–812, aug 1990.

[114] J. Požela and A. Reklaitis. Diffusion coefficient of hot electrons in GaAs. *Solid State Communications*, 27(11):1073–1077, 1978.

[115] J. Požela and A. Reklaitis. Electron transport properties in GaAs at high electric fields. *Solid-State Electronics*, 23(9):927–933, 1980.

[116] V. Gruzinskis and A. Reklaitis. Steady-state electron transport in short GaAs n-n-nstructures. *Semiconductor Science and Technology*, 3(8):754–757, aug 1988.

[117] A.R. Adams, P.J. Vinson, C. Pickering, G.D. Pitt, and W. Fawcett. 3-level conduction-band structure of GaAs from high-stress and high-field measurements. *Electronics Letters*, 13(2):46, 1977.

[118] R Mitskyavichyus and A Reklaitis. Rate of intervalley processes in n-type GaAs. *Soviet Physics. Semiconductors*, 20(9):1060–1061, 1986.

[119] Jagdeep Shah, Benoit Deveaud, T. C. Damen, W. T. Tsang, A. C. Gossard, and P. Lugli. Determination of intervalley scattering rates in GaAs by subpicosecond luminescence spectroscopy. *Phys. Rev. Lett.*, 59:2222–2225, Nov 1987.

[120] R. G. Ulbrich, J. A. Kash, and J. C. Tsang. Hot-Electron Recombination at Neutral Acceptors in GaAs: A cw Probe of Femtosecond Intervalley Scattering. *Phys. Rev. Lett.*, 62:949–952, Feb 1989.

[121] J. A. Kash. Hot-electron luminescence: A comparison of GaAs and InP. *Phys. Rev. B*, 47:1221–1227, Jan 1993.

[122] I Ya Karlik, DN Mirlin, and VF Sapega. Probability of intervalley transitions in gallium-arsenide crystals. *Fizika i Tekhnika Poluprovodnikov*, 21(6):1030–1032, 1987.

[123] D.N. Mirlin, V.F. Sapega, I.Ya. Karlik, and R. Katilius. Hot photoluminescence spectroscopy investigations of l-valley splitting and intervalley scattering in uniaxially stressed gallium arsenide. *Solid State Communications*, 61(12):799–802, 1987.

[124] J. Sjakste, V. Tyuterev, and N. Vast. Intervalley scattering in gaas: ab initio calculation of the effective parameters for monte carlo simulations. *Applied Physics A*, 86(3):301–307, Mar 2007.

[125] Stefan Zollner, Sudha Gopalan, and Manuel Cardona. Microscopic theory of intervalley scattering in GaAs: k dependence of deformation potentials and scattering rates. *Journal of Applied Physics*, 68(4):1682–1693, 1990.

[126] J Sjakste, K Tanimura, G Barbarino, L Perfetti, and N Vast. Hot electron relaxation dynamics in semiconductors: assessing the strength of the electron–phonon coupling from the theoretical and experimental viewpoints. *Journal of Physics: Condensed Matter*, 30(35):353001, aug 2018.

[127] Jelena Sjakste, Nathalie Vast, Giuliana Barbarino, Matteo Calandra, Francesco Mauri, Junichi Kanasaki, Hiroshi Tanimura, and Katsumi Tanimura. Energy relaxation mechanism of hot-electron ensembles in gaas: Theoretical and experimental study of its temperature dependence. *Phys. Rev. B*, 97:064302, Feb 2018.

[128] Hiroshi Tanimura, Jun'ichi Kanasaki, Katsumi Tanimura, Jelena Sjakste, Nathalie Vast, Matteo Calandra, and Francesco Mauri. Formation of hot-electron ensembles quasiequilibrated in momentum space by ultrafast momentum scattering of highly excited hot electrons photoinjected into the Γ valley of gaas. *Phys. Rev. B*, 93:161203, Apr 2016.

[129] Basil D. Washo and David Hansen. Heat conduction in linear amorphous high polymers: Orientation anisotropy. *Journal of Applied Physics*, 40(6):2423–2427, 1969.

[130] S Burgess and D Greig. The low-temperature thermal conductivity of polyethylene. *Journal of Physics C: Solid State Physics*, 8(11):1637–1648, jun 1975.

[131] H.G. Kilian and M. Pietralla. Anisotropy of thermal diffusivity of uniaxial stretched polyethylenes. *Polymer*, 19(6):664 – 672, 1978. Polymer Physics Group Conference.

[132] D. B. Mergenthaler, M. Pietralla, S. Roy, and H. G. Kilian. Thermal conductivity in ultraoriented polyethylene. *Macromolecules*, 25(13):3500–3502, June 1992.

[133] C. L. Choy, Y. W. Wong, G. W. Yang, and Tetsuo Kanamoto. Elastic modulus and thermal conductivity of ultradrawn polyethylene. *Journal of Polymer Science Part B: Polymer Physics*, 37(23):3359–3367, December 1999.

[134] L Piraux, M Kinany-Alaoui, J. P Issi, D Begin, and D Billaud. Thermal conductivity of an oriented polyacetylene film. *Solid State Communications*, 70(4):427–429, March 1989.

[135] Ramesh Shrestha, Pengfei Li, Bikramjit Chatterjee, Teng Zheng, Xufei Wu, Zeyu Liu, Tengfei Luo, Sukwon Choi, Kedar Hippalgaonkar, Maarten P. de Boer, and Sheng Shen. Crystalline polymer nanofibers with ultra-high strength and thermal conductivity. *Nature Communications*, 9(1):1664, April 2018.

[136] Sara Ronca, Tamito Igarashi, Giuseppe Forte, and Sanjay Rastogi. Metallic-like thermal conductivity in a lightweight insulator: Solid-state processed ultra high molecular weight polyethylene tapes and films. *Polymer*, 123:203 – 210, 2017.

[137] Yanfei Xu, Daniel Kraemer, Bai Song, Zhang Jiang, Jiawei Zhou, James Loomis, Jianjian Wang, Mingda Li, Hadi Ghasemi, Xiaopeng Huang, Xiaobo Li, and Gang Chen. Nanostructured polymer films with metal-like thermal conductivity. *Nature Communications*, 10(1):1771, April 2019.

[138] Andrew B. Robbins, Stavros X. Drakopoulos, Ignacio Martin-Fabiani, Sara Ronca, and Austin J. Minnich. Ballistic thermal phonons traversing nanocrystalline domains in oriented polyethylene. *Proceedings of the National Academy of Sciences*, 116(35):17163–17168, 2019.

[139] Taeyong Kim, Stavros X. Drakopoulos, Sara Ronca, and Austin J. Minnich. Origin of high thermal conductivity in disentangled ultra-high molecular weight polyethylene films: ballistic phonons within enlarged crystals, 2021.

[140] Xiaojia Wang, Victor Ho, Rachel A. Segalman, and David G. Cahill. Thermal conductivity of high-modulus polymer fibers. *Macromolecules*, 46(12):4937–4943, 2013.

[141] Tianli Feng and Xiulin Ruan. Quantum mechanical prediction of four-phonon scattering rates and reduced thermal conductivity of solids. *Physical Review B*, 93(4):045202, January 2016.

[142] Navaneetha K. Ravichandran and David Broido. Unified first-principles theory of thermal properties of insulators. *Physical Review B*, 98(8):085205, August 2018.

[143] Karel Kunc. *Recent Results in Semiconductor Dynamics by Ab Initio 'Direct' Approach*, pages 227–312. Springer US, Boston, MA, 1985.

[144] G Kresse, J Furthmüller, and J Hafner. Ab initio force constant approach to phonon dispersion relations of diamond and graphite. *Europhysics Letters (EPL)*, 32(9):729–734, dec 1995.

[145] Atsushi Togo and Isao Tanaka. First principles phonon calculations in materials science. *Scripta Materialia*, 108:1–5, 2015.

[146] Jin-Jian Zhou, Olle Hellman, and Marco Bernardi. Electron-phonon scattering in the presence of soft modes and electron mobility in srtio$_3$ perovskite from first principles. *Phys. Rev. Lett.*, 121:226603, Nov 2018.

[147] P. Souvatzis, O. Eriksson, M. I. Katsnelson, and S. P. Rudin. Entropy driven stabilization of energetically unstable crystal structures explained from first principles theory. *Phys. Rev. Lett.*, 100:095901, Mar 2008.

[148] Ion Errea, Matteo Calandra, and Francesco Mauri. First-principles theory of anharmonicity and the inverse isotope effect in superconducting palladium-hydride compounds. *Phys. Rev. Lett.*, 111:177002, Oct 2013.

[149] Fei Zhou, Weston Nielson, Yi Xia, and Vidvuds Ozoliņš. Lattice anharmonicity and thermal conductivity from compressive sensing of first-principles calculations. *Phys. Rev. Lett.*, 113:185501, Oct 2014.

[150] M. L. Klein and G. K. Horton. The rise of self-consistent phonon theory. *J. Low Temp. Phys*, 9(3):151–166, 1972.

[151] D. West and S. K. Estreicher. First-principles calculations of vibrational lifetimes and decay channels: Hydrogen-related modes in si. *Phys. Rev. Lett.*, 96:115504, 2006.

[152] Olle Hellman, Peter Steneteg, I. A. Abrikosov, and S. I. Simak. Temperature dependent effective potential method for accurate free energy calculations of solids. *Phys. Rev. B*, 87:104111, 2013.

[153] R. Shankar. *Principles of Quantum Mechanics*. Springer US, 2012.

[154] M. Omini and A. Sparavigna. Beyond the isotropic-model approximation in the theory of thermal conductivity. *Phys. Rev. B*, 53:9064–9073, Apr 1996.

[155] D. A. Broido, A. Ward, and N. Mingo. Lattice thermal conductivity of silicon from empirical interatomic potentials. *Phys. Rev. B*, 72:014308, Jul 2005.

[156] G. Kresse and J. Furthmüller. Efficient iterative schemes for *ab initio* total-energy calculations using a plane-wave basis set. *Phys. Rev. B*, 54:11169, 1996.

[157] G. Kresse and J. Furthmüller. Efficiency of ab-initio total energy calculations for metals and semiconductors using a plane-wave basis set. *Comput. Mater. Sci.*, 6(1):15, 1996.

[158] G. Kresse and D. Joubert. From ultrasoft pseudopotentials to the projector augmented-wave method. *Physical Review B*, 59(3):1758–1775, January 1999.

[159] G. Kresse and J. Hafner. Ab initio molecular dynamics for open-shell transition metals. *Physical Review B*, 48(17):13115–13118, November 1993.

[160] M. Dion, H. Rydberg, E. Schröder, D. C. Langreth, and B. I. Lundqvist. Van der waals density functional for general geometries. *Phys. Rev. Lett.*, 92:246401, 2004.

[161] J Klimeš, David R. Bowler, and Angelos Michaelides. Van der waals density functionals applied to solids. *Phys. Rev. B*, 83:195131, 2011.

[162] Guillermo Román-Pérez and José M. Soler. Efficient implementation of a van der waals density functional: Application to double-wall carbon nanotubes. *Phys. Rev. Lett.*, 103:096102, 2009.

[163] Jesper Kleis, Bengt I. Lundqvist, David C. Langreth, and Elsebeth Schröder. Towards a working density-functional theory for polymers: First-principles determination of the polyethylene crystal structure. *Physical Review B*, 76(10):100201, September 2007.

[164] Thinh H. Pham, Rampi Ramprasad, and Huy-Viet Nguyen. Density-functional description of polymer crystals: A comparative study of recent van der waals functionals. *The Journal of Chemical Physics*, 144(21):214905, 2016.

[165] Ankit Jain and Alan J. H. McGaughey. Effect of exchange–correlation on first-principles-driven lattice thermal conductivity predictions of crystalline silicon. *Computational Materials Science*, 110:115–120, December 2015.

[166] Shin-ichiro Tamura. Isotope scattering of dispersive phonons in Ge. *Physical Review B*, 27(2):858–866, January 1983.

[167] Z. Mo, K. B. Lee, Y. B. Moon, M. Kobayashi, A. J. Heeger, and F. Wudl. X-ray scattering from poly(thiophene): crystallinity and crystallographic structure. *Macromolecules*, 18(10):1972–1977, October 1985.

[168] Xu Lu, Donald T. Morelli, Yi Xia, Fei Zhou, Vidvuds Ozolins, Hang Chi, Xiaoyuan Zhou, and Ctirad Uher. High Performance Thermoelectricity in Earth-Abundant Compounds Based on Natural Mineral Tetrahedrites. *Advanced Energy Materials*, 3(3):342–348, March 2013.

[169] D. S. Kim, O. Hellman, J. Herriman, H. L. Smith, J. Y. Y. Lin, N. Shulumba, J. L. Niedziela, C. W. Li, D. L. Abernathy, and B. Fultz. Nuclear quantum effect with pure anharmonicity and the anomalous thermal expansion of silicon. *Proceedings of the National Academy of Sciences*, 115(9):1992–1997, 2018.

[170] Sea-Fue Wang, Yung-Fu Hsu, Jui-Chen Pu, James C. Sung, and L.G. Hwa. Determination of acoustic wave velocities and elastic properties for diamond and other hard materials. *Materials Chemistry and Physics*, 85(2):432–437, 2004.

[171] P. W. Bridgman. The thermal conductivity and compressibility of several rocks under high pressures. *American Journal of Science*, s5-7(38):81–102, 1924.

[172] R G Ross, P Andersson, B Sundqvist, and G Backstrom. Thermal conductivity of solids and liquids under pressure. *Reports on Progress in Physics*, 47(10):1347–1402, oct 1984.

[173] Xiaoli Tang and Jianjun Dong. Lattice thermal conductivity of mgo at conditions of earth's interior. *Proceedings of the National Academy of Sciences*, 107(10):4539–4543, 2010.

[174] D. A. Broido, L. Lindsay, and A. Ward. Thermal conductivity of diamond under extreme pressure: A first-principles study. *Phys. Rev. B*, 86:115203, Sep 2012.

[175] Saikat Mukhopadhyay and Derek A. Stewart. Polar effects on the thermal conductivity of cubic boron nitride under pressure. *Phys. Rev. Lett.*, 113:025901, Jul 2014.

[176] Tao Ouyang and Ming Hu. Competing mechanism driving diverse pressure dependence of thermal conductivity of xTe (x = Hg, Cd, andZn). *Phys. Rev. B*, 92:235204, Dec 2015.

[177] L. Lindsay, D. A. Broido, Jesús Carrete, Natalio Mingo, and T. L. Reinecke. Anomalous pressure dependence of thermal conductivities of large mass ratio compounds. *Phys. Rev. B*, 91:121202, Mar 2015.

[178] Navaneetha K. Ravichandran and David Broido. Non-monotonic pressure dependence of the thermal conductivity of boron arsenide. *Nature Communications*, 10(1):827, Feb 2019.

[179]

[180] L. Lindsay, Wu Li, Jesús Carrete, Natalio Mingo, D. A. Broido, and T. L. Reinecke. Phonon thermal transport in strained and unstrained graphene from first principles. *Phys. Rev. B*, 89:155426, Apr 2014.

[181] Youdi Kuang, Lucas Lindsay, Sanqiang Shi, Xinjiang Wang, and Baoling Huang. Thermal conductivity of graphene mediated by strain and size. *International Journal of Heat and Mass Transfer*, 101:772–778, 2016.

[182] Y. D. Kuang, L. Lindsay, S. Q. Shi, and G. P. Zheng. Tensile strains give rise to strong size effects for thermal conductivities of silicene, germanene and stanene. *Nanoscale*, 8:3760–3767, 2016.

[183] Susumu Hirakawa and Tetuo Takemura. Transitions and phases of polytetrafluoroethylene. *Japanese Journal of Applied Physics*, 8(6):635–641, jun 1969.

[184] Chitoshi Nakafuku and Tetuo Takemura. Crystal structure of high pressure phase of polytetrafluoroethylene. *Japanese Journal of Applied Physics*, 14(5):599–602, may 1975.

[185] Thermal conductivity of ptfe and ptfe composites. *Thermochimica Acta*, 392-393:231–236, 2002.

[186] Francis Birch. Finite elastic strain of cubic crystals. *Phys. Rev.*, 71:809–824, Jun 1947.

[187] Saikat Mukhopadhyay, Dipanshu Bansal, Olivier Delaire, Didier Perrodin, Edith Bourret-Courchesne, David J. Singh, and Lucas Lindsay. The curious case of cuprous chloride: Giant thermal resistance and anharmonic quasiparticle spectra driven by dispersion nesting. *Phys. Rev. B*, 96:100301, Sep 2017.

[188] L. Lindsay, C. Hua, X.L. Ruan, and S. Lee. Survey of ab initio phonon thermal transport. *Materials Today Physics*, 7:106–120, 2018.

[189] Mario Culebras, Clara M. Gómez, and Andrés Cantarero. Review on polymers for thermoelectric applications. *Materials*, 7(9):6701–6732, 2014.

[190] Herbert Fröhlich and Nevill Francis Mott. Theory of electrical breakdown in ionic crystals. *Proceedings of the Royal Society of London. Series A - Mathematical and Physical Sciences*, 160(901):230–241, 1937.

[191] J. G. Ruch and G. S. Kino. Measurement of the velocity-field characteristic of gallium arsenide. *Applied Physics Letters*, 10(2):40–42, 1967.

[192] N. Braslau. Velocity-field characteristic of gallium arsenide from measurement of the conductivity in a microwave field. *Physics Letters A*, 24(10):531–533, 1967.

[193] G.A. Acket and J. de Groot. Measurements of the current-field strength characteristic of n-type gallium arsenide using various high-power microwave techniques. *IEEE Transactions on Electron Devices*, 14(9):505–511, 1967.

[194] M.T. Vlaardingerbroek, W. Kuypers, and G.A. Acket. Energy relaxation time of hot electrons in GaAs. *Physics Letters A*, 28(2):155–156, 1968.

[195] F. Kuchar, A. Philipp, and K. Seeger. Anisotropy of the submillimeter conductivity of warm carriers in n-type gallium arsenide. *Solid State Communications*, 11(8):965–968, 1972.

[196] Masayuki Abe and Shigeo Kaneda. Millimeter-Wave Frequency Response of Hot Electrons in n-type GaAs. *Japanese Journal of Applied Physics*, 11(11):1675–1683, nov 1972.

[197] G. H. Glover. Study of electron energy relaxation times in GaAs and InP. *Journal of Applied Physics*, 44(3):1295–1301, 1973.

[198] E. M. Conwell. Rate of energy loss to polar modes. *Phys. Rev.*, 143:657–658, Mar 1966.

[199] P N Butcher and W Fawcett. The intervalley transfer mechanism of negative resistivity in bulk semiconductors. *Proceedings of the Physical Society*, 86(6):1205–1219, dec 1965.

[200] E.M. Conwell and M.O. Vassell. High-field distribution function in gaas. *IEEE Transactions on Electron Devices*, ED-13(1):22–27, 1966.

[201] E. M. Conwell and M. O. Vassell. High-field transport in- type GaAs. *Physical Review*, 166(3):797–821, feb 1968.

[202] H. D. Rees. Time response of the high-field electron distribution function in gaas. *IBM Journal of Research and Development*, 13(5):537–542, 1969.

[203] W. Fawcett, A.D. Boardman, and S. Swain. Monte carlo determination of electron transport properties in gallium arsenide. *Journal of Physics and Chemistry of Solids*, 31(9):1963–1990, 1970.

[204] J. G. Ruch and W. Fawcett. Temperature dependence of the transport properties of gallium arsenide determined by a monte carlo method. *Journal of Applied Physics*, 41(9):3843–3849, 1970.

[205] M. A. Littlejohn, J. R. Hauser, and T. H. Glisson. Velocity-field characteristics of gaas with c6-lc6-xc6 conduction-band ordering. *Journal of Applied Physics*, 48(11):4587–4590, 1977.

[206] Gregory H. Wannier. Motion of gaseous ions in a strong electric field. ii. *Phys. Rev.*, 87:795–798, Sep 1952.

[207] N.A. Hashitsume. Statistical theory of nonlinear dissipative systems. *Progress of Theoretical Physics*, 15(4), 1956. https://academic.oup.com/ptp/article/8/4/461/1857479.

[208] B.B. Kadomotsev. Fundamental equations of the kinetic theory of gases from the point of view of the theory of random processes. *Soviet Physics JETP*, 5(4), 1957.

[209] Melvin Lax. Fluctuations from the nonequilibrium steady state. *Rev. Mod. Phys.*, 32:25–64, Jan 1960. https://link.aps.org/doi/10.1103/RevModPhys.32.25.

[210] Sh.M. Kogan and A.Ya. Shul'man. Theory of Fluctuations in a Nonequilibrium Electron Gas. *Soviet Physics JETP*, 29(3), 1969.

[211] Melvin Lax. Quantum noise. iv. quantum theory of noise sources. *Phys. Rev.*, 145:110–129, May 1966. https://link.aps.org/doi/10.1103/PhysRev.145.110.

[212] K.M. van Vliet and J.R. Fasset. 'fluctuations due to electronic transitions and transport in solids'. In R.E. Burgess, editor, *'Fluctuation Phenomena in Solids'*, chapter 7. Academic, New York, 1965.

[213] Sh.M. Kogan and A.Ya. Shul'man. Extraneous random forces and equations for correlation functions in the theory of nonequilibrium fluctuations. *Soviet Physics Solid State*, 12(4):467, 1970.

[214] W. Fawcett and H.D. Rees. Calculation of the hot electron diffusion rate for gaas. *Physics Letters A*, 29(10):578 – 579, 1969.

[215] C. Jacoboni. Generalization of fick's law for non-local complex diffusion in semiconductors. *physica status solidi (b)*, 65(1):61–65, 1974.

[216] A. Alberigi Quaranta, V. Borsari, C. Jacoboni, and G. Zanarini. Electron diffusion in cdte. *Applied Physics Letters*, 22(3):103–105, 1973.

[217] V. Bareikis, V. Viktoravicius, A. Galdikas, and R. Miliusyte. Microwave Noise and Constant of the Coupling Between the Valleys Gamma and l in a Three-Valley Model of GaAs. *Soviet Physics-Semiconductors*, 14(7):847–849, 1980.

[218] D. Y. Xing, M. Liu, and C. S. Ting. Analytical approach to diffusion of hot carriers in n-type gaas with Γ-l-x band structure. *Phys. Rev. B*, 37:10283–10294, Jun 1988.

[219] Christopher J. Stanton and John W. Wilkins. Nonequilibrium current fluctuations in semiconductors: A boltzmann-equation–green-function approach. *Phys. Rev. B*, 35:9722–9734, Jun 1987.

[220] Christopher J. Stanton and John W. Wilkins. Hot-electron noise in two-valley semiconductors: An analytic model. *Phys. Rev. B*, 36:1686–1695, Jul 1987.

[221] L. Gherardi, A. Pellacani, and C. Jacoboni. Velocity autocorrelation and low temperature mobility of electrons in silicon. *Lettere al Nuovo Cimento*, 14:225–232, 1975.

[222] R. Fauquembergue, J. Zimmermann, A. Kaszynski, E. Constant, and Greco Microondes. Diffusion and the power spectral density and correlation function of velocity fluctuation for electrons in si and gaas by monte carlo methods. *Journal of Applied Physics*, 51(2):1065–1071, 1980.

[223] D. K. Ferry and J. R. Barker. Generalized diffusion, mobility, and the velocity autocorrelation function for high-field transport in semiconductors. *Journal of Applied Physics*, 52(2):818–824, 1981.

[224] Tilmann Kuhn, Lino Reggiani, Luca Varani, and Vladimir Mitin. Monte carlo method for the simulation of electronic noise in semiconductors. *Phys. Rev. B*, 42:5702–5713, Sep 1990.

[225] G. Hill, P. N. Robson, and W. Fawcett. Diffusion and the power spectral density of velocity fluctuations for electrons in inp by monte carlo methods. *Journal of Applied Physics*, 50(1):356–360, 1979.

[226] Shulong Wang, Hongxia Liu, Bo Gao, and Huimin Cai. Monte carlo calculation of electron diffusion coefficient in wurtzite indium nitride. *Applied Physics Letters*, 100(14):142105, 2012. https://doi.org/10.1063/1.3700720.

[227] E Starikov, P Shiktorov, V Gružinskis, L Reggiani, L Varani, J C Vaissière, and C Palermo. Monte carlo calculations of hot-electron transport and diffusion noise in GaN and InN. *Semiconductor Science and Technology*, 20(3):279–285, feb 2005. https://iopscience.iop.org/article/10.1088/0268-1242/20/3/004.

[228] V. Bareikis, K. Kibickas, J. Liberis, A. Matulionis, R. Miliušytė, J. Paršeliūnas, J. Požela, and P. Sakalas. Velocity overshoot and suppression of diffusivity and microwave noise in short n+-n-n+ structures of GaAs. In Bengt Källbäck and Heinz Beneking, editors, *High-Speed Electronics*, pages 28–31, Berlin, Heidelberg, 1986. Springer Berlin Heidelberg.

[229] V. Bareikis, J. Liberis, A. Matulionis, R. Miliušyt, J. Požela, and P. Sakalas. Length dependent hot electron noise in doped GaAs. *Solid-State Electronics*, 32(12):1647–1650, 1989. Special Issue Hot Carriers in Semiconductors.

[230] J. Mateos, T. Gonzalez, D. Pardo, V. Hoel, and A. Cappy. Monte carlo simulator for the design optimization of low-noise hemts. *IEEE Transactions on Electron Devices*, 47(10):1950–1956, 2000.

[231] J. Mateos, H. Rodilla, B.G. Vasallo, and T. Gonzalez. Monte carlo modelling of noise in advanced iii-v hemts. *Journal of Computational Electronics*, 14:72–86, 2015.

[232] R. Rengel and M. J. Martín. Diffusion coefficient, correlation function, and power spectral density of velocity fluctuations in monolayer graphene. *Journal of Applied Physics*, 114(14):143702, 2013. https://doi.org/10.1063/1.4824182.

[233] A. Rustagi and C. J. Stanton. Hot-electron noise properties of graphene-like systems. *Phys. Rev. B*, 90:245424, Dec 2014.

[234] M. Lundstrom. *Fundamentals of Carrier Transport*. Cambridge University Press, Cambridge, 2000.

[235] Feliciano Giustino, Jonathan R. Yates, Ivo Souza, Marvin L. Cohen, and Steven G. Louie. Electron-phonon interaction via electronic and lattice wannier functions: Superconductivity in boron-doped diamond reexamined. *Phys. Rev. Lett.*, 98:047005, Jan 2007.

[236] Feliciano Giustino, Marvin L. Cohen, and Steven G. Louie. Electron-phonon interaction using wannier functions. *Phys. Rev. B*, 76:165108, Oct 2007.

[237] Nicola Marzari, Arash A. Mostofi, Jonathan R. Yates, Ivo Souza, and David Vanderbilt. Maximally localized wannier functions: Theory and applications. *Rev. Mod. Phys.*, 84:1419–1475, Oct 2012.

[238] Nicola Marzari and David Vanderbilt. Maximally localized generalized wannier functions for composite energy bands. *Phys. Rev. B*, 56:12847–12865, Nov 1997.

[239] J. Sjakste, N. Vast, M. Calandra, and F. Mauri. Wannier interpolation of the electron-phonon matrix elements in polar semiconductors: Polar-optical coupling in gaas. *Phys. Rev. B*, 92:054307, Aug 2015. https://link.aps.org/doi/10.1103/PhysRevB.92.054307.

[240] Carla Verdi and Feliciano Giustino. Fröhlich electron-phonon vertex from first principles. *Phys. Rev. Lett.*, 115:176401, Oct 2015.

[241] J. Zhou, J. Park, I. Lu, I. Maliyov, X. Tong, and M. Bernardi. Perturbo: a software package for ab initio electron-phonon interactions, charge transport and ultrafast dynamics. 2020.

[242] Arash A. Mostofi, Jonathan R. Yates, Young-Su Lee, Ivo Souza, David Vanderbilt, and Nicola Marzari. wannier90: A tool for obtaining maximally-localised wannier functions. *Computer Physics Communications*, 178(9):685 – 699, 2008.

[243] Giovanni Pizzi, Valerio Vitale, Ryotaro Arita, Stefan Blügel, Frank Freimuth, Guillaume Géranton, Marco Gibertini, Dominik Gresch, Charles Johnson, Takashi Koretsune, Julen Ibañez-Azpiroz, Hyungjun Lee, Jae-Mo Lihm, Daniel Marchand, Antimo Marrazzo, Yuriy Mokrousov, Jamal I Mustafa, Yoshiro Nohara, Yusuke Nomura, Lorenzo Paulatto, Samuel Poncé, Thomas Ponweiser, Junfeng Qiao, Florian Thöle, Stepan S Tsirkin, Małgorzata Wierzbowska, Nicola Marzari, David Vanderbilt, Ivo Souza, Arash A Mostofi, and Jonathan R Yates. Wannier90 as a community code: new features and applications. *Journal of Physics: Condensed Matter*, 32(16):165902, jan 2020.

[244] Gallium arsenide (GaAs), debye temperature, density, heat capacity, melting point: Datasheet from landolt-börnstein - group iii condensed matter · volume 41a1β: "group iv elements, iv-iv and iii-v compounds. part b - electronic, transport, optical and other properties" in springermaterials (https://doi.org/10.1007/10832182_226). accessed 2022-01-20.

[245] S.V. Gantsevich, V.L. Gurevich, and R. Katilius. Theory of fluctuations in nonequilibrium electron gas. *Rivista Del Nuovo Cimento*, 2(5), 1979.

[246] András Ambrózy. *Electronic noise*. McGraw-Hill International Book Co., 1982.

[247] R.H. Fowler. *Statistical Mechanics*. Cambridge University Press, London, 1936.

[248] Paolo Giannozzi, Stefano Baroni, Nicola Bonini, Matteo Calandra, Roberto Car, Carlo Cavazzoni, Davide Ceresoli, Guido L Chiarotti, Matteo Cococcioni, Ismaila Dabo, Andrea Dal Corso, Stefano de Gironcoli, Stefano Fabris, Guido Fratesi, Ralph Gebauer, Uwe Gerstmann, Christos Gougoussis, Anton Kokalj, Michele Lazzeri, Layla Martin-Samos, Nicola Marzari, Francesco Mauri, Riccardo Mazzarello, Stefano Paolini, Alfredo Pasquarello, Lorenzo Paulatto, Carlo Sbraccia, Sandro Scandolo, Gabriele Sclauzero, Ari P Seitsonen, Alexander Smogunov, Paolo Umari, and Renata M Wentzcovitch. QUANTUM ESPRESSO: a modular and open-source software project for quantum simulations of materials. *Journal of Physics: Condensed Matter*, 21(39):395502, sep 2009.

[249] P Giannozzi, O Andreussi, T Brumme, O Bunau, M Buongiorno Nardelli, M Calandra, R Car, C Cavazzoni, D Ceresoli, M Cococcioni, N Colonna, I Carnimeo, A Dal Corso, S de Gironcoli, P Delugas, R A DiStasio, A Ferretti, A Floris, G Fratesi, G Fugallo, R Gebauer, U Gerstmann, F Giustino, T Gorni, J Jia, M Kawamura, H-Y Ko, A Kokalj, E Küçükbenli, M Lazzeri, M Marsili, N Marzari, F Mauri, N L Nguyen, H-V Nguyen, A Otero de-la Roza, L Paulatto, S Poncé, D Rocca, R Sabatini, B Santra, M Schlipf, A P Seitsonen, A Smogunov, I Timrov, T Thonhauser, P Umari, N Vast, X Wu, and S Baroni. Advanced capabilities for materials modelling with quantum ESPRESSO. *Journal of Physics: Condensed Matter*, 29(46):465901, oct 2017.

[250] Alexander Y. Choi, Peishi S. Cheng, Benjamin Hatanpää, and Austin J. Minnich. Electronic noise of warm electrons in semiconductors from first principles. *Phys. Rev. Materials*, 5:044603, Apr 2021.

[251] Peishi S. Cheng, Shi-Ning Sun, Alexander Y. Choi, and Austin J. Minnich. High-field transport and hot electron noise in gaas from first principles: role of two-phonon scattering, 2022.

[252] Pauli Virtanen, Ralf Gommers, Travis E. Oliphant, Matt Haberland, Tyler Reddy, David Cournapeau, Evgeni Burovski, Pearu Peterson, Warren Weckesser, Jonathan Bright, Stéfan J. van der Walt, Matthew Brett, Joshua Wilson, K. Jarrod Millman, Nikolay Mayorov, Andrew R. J. Nelson, Eric Jones, Robert Kern, Eric Larson, C. J. Carey, İlhan Polat, Yu Feng, Eric W. Moore, Jake VanderPlas, Denis Laxalde, Josef

Perktold, Robert Cimrman, Ian Henriksen, E. A. Quintero, Charles R. Harris, Anne M. Archibald, Antônio H. Ribeiro, Fabian Pedregosa, Paul van Mulbregt, Aditya Vijaykumar, Alessandro Pietro Bardelli, Alex Rothberg, Andreas Hilboll, Andreas Kloeckner, Anthony Scopatz, Antony Lee, Ariel Rokem, C. Nathan Woods, Chad Fulton, Charles Masson, Christian Häggström, Clark Fitzgerald, David A. Nicholson, David R. Hagen, Dmitrii V. Pasechnik, Emanuele Olivetti, Eric Martin, Eric Wieser, Fabrice Silva, Felix Lenders, Florian Wilhelm, G. Young, Gavin A. Price, Gert-Ludwig Ingold, Gregory E. Allen, Gregory R. Lee, Hervé Audren, Irvin Probst, Jörg P. Dietrich, Jacob Silterra, James T. Webber, Janko Slavič, Joel Nothman, Johannes Buchner, Johannes Kulick, Johannes L. Schönberger, José Vinícius de Miranda Cardoso, Joscha Reimer, Joseph Harrington, Juan Luis Cano Rodríguez, Juan Nunez-Iglesias, Justin Kuczynski, Kevin Tritz, Martin Thoma, Matthew Newville, Matthias Kümmerer, Maximilian Bolingbroke, Michael Tartre, Mikhail Pak, Nathaniel J. Smith, Nikolai Nowaczyk, Nikolay Shebanov, Oleksandr Pavlyk, Per A. Brodtkorb, Perry Lee, Robert T. McGibbon, Roman Feldbauer, Sam Lewis, Sam Tygier, Scott Sievert, Sebastiano Vigna, Stefan Peterson, Surhud More, Tadeusz Pudlik, Takuya Oshima, Thomas J. Pingel, Thomas P. Robitaille, Thomas Spura, Thouis R. Jones, Tim Cera, Tim Leslie, Tiziano Zito, Tom Krauss, Utkarsh Upadhyay, Yaroslav O. Halchenko, Yoshiki Vázquez-Baeza, and SciPy 1.0 Contributors. Scipy 1.0: fundamental algorithms for scientific computing in python. *Nature Methods*, 17(3):261–272, Mar 2020.

[253] Valérie Frayssé, Luc Giraud, Serge Gratton, and Julien Langou. Algorithm 842: A set of gmres routines for real and complex arithmetics on high performance computers. *ACM Trans. Math. Softw.*, 31(2):228–238, June 2005.

[254] Vatsal A. Jhalani, Jin-Jian Zhou, Jinsoo Park, Cyrus E. Dreyer, and Marco Bernardi. Piezoelectric electron-phonon interaction from ab initio dynamical quadrupoles: Impact on charge transport in wurtzite gan. *Phys. Rev. Lett.*, 125:136602, Sep 2020.

[255] Esther Conwell. *High Field Transport in Semiconductors*. Academic Press, 1967. https://www.google.com/books/edition/{High_Field_Transport_in_Semiconductors}/{9teaxQEACAAJ}?hl=en.

[256] J. G. Ruch and G. S. Kino. Transport Properties of GaAs. *Phys. Rev.*, 174:921–931, Oct 1968.

[257] J. S. Blakemore. Semiconducting and other major properties of gallium arsenide. *Journal of Applied Physics*, 53(10):R123–R181, 1982.

[258] S. Teitel and J. W. Wilkins. Small-signal ac conductivity and velocity overshoot in semiconductor materials. *Journal of Applied Physics*, 53(7):5006–5012, 1982. https://doi.org/10.1063/1.331376.

[259] B.J. Davydov. On the theory of electron motion in gases and semiconductors. *Zh. Eksp. Teor. Fiz.*, 8:1069, 1937.

[260] H R Skullerud. Longitudinal diffusion of electrons in electrostatic fields in gases. *Journal of Physics B: Atomic and Molecular Physics*, 2(6):696–705, June 1969.

[261] V.L. Gurevich and R. Katilius. Contribution to the theory of hot electrons in an anisotropic semiconductor. *Soviet Physics JETP*, 22:796, April 1966. http://www.jetp.ac.ru/cgi-bin/e/index/e/22/4/p796?a=list.

[262] W.A. Schlup. Definition of noise temperatures θ in three dimensions and the conjecture $\theta \geq t$ in nonequilibrium systems. *Physica*, 69(2):485 – 498, 1973. "http://www.sciencedirect.com/science/article/pii/0031891473900852".

[263] V. Aninkevičius, V. Bareikis, J. Liberis, A. Matulionis, and P. Sakalas. Comparative analysis of microwave noise in GaAs and AlGaAs/GaAs channels. *Solid-State Electronics*, 36(9):1339–1343, 1993.

[264] S. Karishy, C. Palermo, G. Sabatini, H. Marinchio, L. Varani, J. Mateos, and T. González. Monte carlo calculation of In0.53Ga0.47As and InAs noise parameters. In *2017 International Conference on Noise and Fluctuations (ICNF)*, pages 1–4. 'IEEE', 2017. https://ieeexplore.ieee.org/document/7985941.

[265] Laurent Chaput. Direct solution to the linearized phonon boltzmann equation. *Phys. Rev. Lett.*, 110:265506, Jun 2013.

[266] P.J. Price. 'fluctuations of hot electrons in semiconductors'. In R.E. Burgess, editor, *'Fluctuation Phenomena in Solids'*, chapter 8. Academic, New York, 1965.

[267] R.I. Rabinovich. On galvanomagnetic phenomena under hot-electron energy scattering on optical phonons. *Soviet Physics - Semiconductors*, 3(7):839, 1969.

[268] Kazumi Ashida, Masataka Inoue, Junji Shirafuji, and Yoshio Inuishi. Energy relaxation effect of hot electrons in GaAs. *Journal of the Physical Society of Japan*, 37(2):408–414, 1974.

[269] D. E. Aspnes, C. G. Olson, and D. W. Lynch. Ordering and absolute energies of the ${l_6}^c$ and ${x_6}^c$ conduction band minima in GaAs. *Phys. Rev. Lett.*, 37:766–769, Sep 1976.

[270] Mark Lundstrom. *High-field transport in bulk semiconductors*, page 282–314. Cambridge University Press, 2 edition, 2000.

[271] D. Gasquet, M. de Murcia, J.P. Nougier, and C. Gontrand. Transport parameters of hot electrons in gaas at 300 k. *Physica B+C*, 134(1):264–268, 1985.

[272] T.H. Glisson, R.A. Sadler, J.R. Hauser, and M.A. Littlejohn. Circuit effects in time-of-flight diffusivity measurements. *Solid-State Electronics*, 23(6):627–630, 1980.

[273] Stefan Zollner, Sudha Gopalan, and Manuel Cardona. Effective intervalley deformation potentials in the description of time-resolved and hot-electron luminescence. *Solid State Communications*, 76(7):877–879, 1990.

[274] V.D. Dymnikov, D.N. Mirlin, L.P. Nikitin, V.I. Perel', I.I. Reshina, and V.F. Sapega. Depolarization of hot photoluminescence of gallium arsenide crystals in a magnetic field. determination of the energy relaxation times of hot electrons. *Journal of Experimental and Theoretical Physics*, 53(5):912, 1981.

[275] G. Fasol, W. Hackenberg, H. P. Hughes, K. Ploog, E. Bauser, and H. Kano. Continuous-wave spectroscopy of femtosecond carrier scattering in GaAs. *Phys. Rev. B*, 41:1461–1478, Jan 1990.

[276] H. Rodilla, J. Schleeh, P. Nilsson, N. Wadefalk, J. Mateos, and J. Grahn. Cryogenic performance of low-noise inp hemts: A monte carlo study. *IEEE Transactions on Electron Devices*, 60(5):1625–1631, 2013. https://ieeexplore.ieee.org/document/6497570.

[277] I. Iñiguez–de-la Torre, J. Mateos, D. Pardo, and T. González. Monte carlo analysis of noise spectra in self-switching nanodiodes. *Journal of Applied Physics*, 103(2):024502, 2008. https://doi.org/10.1063/1.2832505.

[278] H. Rodilla, T. González, D. Pardo, and J. Mateos. High-mobility heterostructures based on inas and insb: A monte carlo study. *Journal of Applied Physics*, 105(11):113705, 2009. https://doi.org/10.1063/1.3132863.

[279] L. Lindsay, D. A. Broido, and Natalio Mingo. Flexural phonons and thermal transport in graphene. *Phys. Rev. B*, 82:115427, Sep 2010.

[280] I-Te Lu, Jin-Jian Zhou, and Marco Bernardi. Efficient ab initio calculations of electron-defect scattering and defect-limited carrier mobility. *Phys. Rev. Materials*, 3:033804, Mar 2019.

[281] I-Te Lu, Jin-Jian Zhou, Jinsoo Park, and Marco Bernardi. First-principles ionized-impurity scattering and charge transport in doped materials. *Phys. Rev. Materials*, 6:L010801, Jan 2022.

[282] H. K. Jung, K. Taniguchi, and C. Hamaguchi. Impact ionization model for full band monte carlo simulation in gaas. *Journal of Applied Physics*, 79(5):2473–2480, 1996.

[283] Marco Bernardi, Derek Vigil-Fowler, Chin Shen Ong, Jeffrey B. Neaton, and Steven G. Louie. Ab initio study of hot electrons in GaAs. *Proceedings of the National Academy of Sciences*, 2015.

[284] Takao Kotani and Mark van Schilfgaarde. Impact ionization rates for si, gaas, inas, zns, and gan in the *gw* approximation. *Phys. Rev. B*, 81:125201, Mar 2010.

[285] Anna Hauber and Stephen Fahy. Scattering of carriers by coupled plasmon-phonon modes in bulk polar semiconductors and polar semiconductor heterostructures. *Phys. Rev. B*, 95:045210, Jan 2017.

[286] G.D. Mahan. *Many-Particle Physics*. Physics of Solids and Liquids. Springer US, 2000.

[287] Jagdeep Shah. Hot electrons and phonons under high intensity photoexcitation of semiconductors. *Solid-State Electronics*, 21(1):43–50, 1978.

[288] Ajit K. Vallabhaneni, Dhruv Singh, Hua Bao, Jayathi Murthy, and Xiulin Ruan. Reliability of raman measurements of thermal conductivity of single-layer graphene due to selective electron-phonon coupling: A first-principles study. *Phys. Rev. B*, 93:125432, Mar 2016.

[289] Lutz Waldecker, Roman Bertoni, Ralph Ernstorfer, and Jan Vorberger. Electron-phonon coupling and energy flow in a simple metal beyond the two-temperature approximation. *Phys. Rev. X*, 6:021003, Apr 2016.

[290] Sridhar Sadasivam, Maria K. Y. Chan, and Pierre Darancet. Theory of thermal relaxation of electrons in semiconductors. *Phys. Rev. Lett.*, 119:136602, Sep 2017.

[291] Xiao Tong and Marco Bernardi. Toward precise simulations of the coupled ultrafast dynamics of electrons and atomic vibrations in materials. *Phys. Rev. Research*, 3:023072, Apr 2021.

[292] Paolo Bordone, Luca Varani, Lino Reggiani, Lucio Rota, and Tilmann Kuhn. Influence of hot phonons on electronic noise in gaas. *Applied Physics Letters*, 63(8):1107–1109, 1993.

[293] P Bordone, L Reggiani, L Varan, and T Kuhn. Hot-phonon effect on noise and diffusion in GaAs. *Semiconductor Science and Technology*, 9(5S):623–626, may 1994.